

https://dspace.org/

Effect of ruthenium additions on the corrosion and mechanical properties of the weld metal of 316L austenitic and LDX 2101 duplex stainless steels

Zuma-Rubambura, Bridget Nomshado

2018

https://hdl.handle.net/10539/27006

Zuma-Rubambura, Bridget Nomshado (2018) Effect of ruthenium additions on the corrosion and mechanical properties of the weld metal of 316L and LDX 2101 duplex stainless steel, University of the Witwatersrand, Johannesburg, https://hdl.handle.net/10539/27006

Downloaded from a DSpace repository. https://dspace.org/



Effect of ruthenium additions on the corrosion and mechanical properties of the weld metal of 316L austenitic and LDX 2101 duplex stainless steels

Prepared by

Bridget Nomshado Zuma-Rubambura

Submitted to

School of Chemical and Metallurgical Engineering, Faculty of Engineering and the Built Environment, University of the Witwatersrand, Johannesburg, South Africa

September, 2018

Declaration

I declare that this dissertation is my own, unaided work. It is being submitted for the Degree of Masters of Science (MSc) in Engineering, in the Faculty of Engineering at the University of the Witwatersrand in Johannesburg, South Africa. It has not been submitted before for any degree or examination in any other university.

Signature:..... Date:18/9/2018.....

Abstract

Austenitic stainless steels (ASSs) and duplex stainless steels (DSSs) are widely used in high performance pressure vessels, nuclear, chemical, process and medical industry due to their very good corrosion resistance and superior mechanical properties (Chernova, et al., 1978). The 316L stainless steel is a Mo containing austenitic steel. Welding is a common technique used to join 316L ASS which results in the solidified weld metal behaving as a miniature “casting”. The welding procedure influences the mechanical properties and the microstructural morphology of the 316L ASS. The L-grade ASSs are generally recognised as resistant to sensitization in short-term exposures or heat treatments such as welding. However, 316L still remains susceptible to other forms of corrosion such as pitting corrosion to a lesser extent compared to conventional Ni -Cr stainless steels such as 304 ASS. LDX 2101 duplex stainless steel was patented by Outokumpu into 2013. Due to its duplex microstructure LDX 2101 offers very good resistance to intergranular corrosion. Duplex stainless steels are less susceptible to this kind of corrosion than austenitic steels. This study explored the impact Ru addition to the weld metal of 316L and LDX 2101 would have on the mechanical and corrosion resistance properties. Corrosion has cost the stainless steel industry extensively in maintenance and mechanical failures particularly at the welded joints of stainless steels. Chernova and Tomashov (1978) showed that a small addition of Platinum Group Metals (PGM) to the weld metal of ASSs caused the cathodic potential to spontaneously move to the passive region through a phenomenon known as “cathodic modification” thus protecting the ASS from corrosion (Chernova, et al., 1978), (Wolff, 1999) and (Potgieter, et al., 1995).This work compromised tests to validate the potential benefit that Ru additions would have on the corrosion resistance of the weld metal based on microstructural and mechanical properties. Additionally the increase in availability and affordability of Ru in South Africa makes it more feasible as an alloying element in the weld metal of 316L ASS and LDX 2101. The microstructural evolution of 316L ASS and LDX 2101 when it undergoes gas tungsten arc welding (GTAW) and the impact on mechanical properties with increasing Ru addition to the weld metal were investigated. The microstructures of all 316L GTAW button samples exhibited γ-austenite phases with δ-ferrite at the dendritic boundaries. Bulky δ-ferrite phases extending to thin dendrite arms were observed at 0.1 wt% Ru while a skeletal δ-ferrite microstructure was observed with 2 wt% Ru addition. The ferrite-austenite (FA) solidification mode suggested that an incomplete solid-state transformation had occurred due to the melting of the 316L in water cooled conical shaped copper mould (Baldissin, et al., 2007). The hardness results revealed that 316L ASS had an increase in hardness as Ru additions were increased due to grain refining nature of Ru. The mechanical properties of LDX 2101 were significantly improved as more Ru was added to the

weld metal. The microstructure exhibited a ferrite matrix and austenite region at 1 wt% Ru addition the grain refining capability of Ru was noted. At 2 wt% Ru addition austenite grains were fully refined into thin grains. The hardness verified this improvement as Ru was added the hardness significantly increased from 230 HV to 235 HV. The potentiodynamic polaristion test indicated that as Ru addition increased there was an increase in corrosion resistance for both 316L and LDX 2101. The corrosion resistance was noted to be peak at 1 wt% Ru addition; thereafter 2 wt% exhibited a decline in corrosion resistance. This was due to the spontaneous passivation of the samples cause by 1 wt% Ru addition and cathodic modification. Overall, it was concluded that the addition of Ru exhibits no detrimental effect of the solid state transformation but rather strengthens the alloy as Ru increases. It can be deduced that the Ru additions in 316L and LDX 2101 weld metal not only improves the weld metal mechanical properties but can additionally improve the corrosion resistance of the weld metal, which confirmed the studies by Potgieter et al. (Potgieter, et al., 2014), and Sherif et al. (Sherif, et al., 2009). The comparative study between LDX 2101 and 316L showed that LDX 2101 exhibited superior mechanical properties compared to 316L and higher hardness values; however this required a secondary post weld heat treatment step to be achieved. The comparative analysis of the potentiodynamic polarisation curves of 1 wt% Ru addition indicated that 316L had lower corrosion rate than LDX 2101.

Acknowledgements

First, I would like to thank the Lord God Almighty for the grace He afforded me to complete these studies. You have been my source of encouragement and hope.

Secondly my appreciation goes to my Supervisor, Dr. Josias van der Merwe. Without his guidance, advice and patience this day would not have arrived.

Thirdly, I would like to thank Edson Muhuma (MINTEK) for sharing his technical knowledge on melting. I would also like to thank my husband Mr Tresor Rubambura, for his love, understanding and support, especially when I had to work long hours.

Last but not least, my appreciation goes to the Center of excellence (COE) for sponsoring my studies, The School of Chemical and Metallurgical Engineering at the University of the Witwatersrand for allowing me to conduct my studies there and providing all necessary equipment and materials and, MINTEK for allowing me to use their equipment.

Table of Contents

Declaration i

Abstract ii

Acknowledgements iv

List of Figures ix

List of Tables xiv

Chapter 1 ..... - 1 -

1.1 Introduction ..... - 1 -

1.2 Problem statement: ..... - 2 -

1.3 Research objectives: ..... - 3 -

Chapter 2 ..... - 4 -

2 Literature review ..... - 4 -

2.1 General background on austenitic stainless steels ..... - 4 -

2.2 AISI 316L austenitic stainless steel ..... - 5 -

2.2.1 Chemical Composition of the AISI 316L ..... - 5 -

2.2.2 Mechanical Properties of the 316L ASS ..... - 5 -

2.3 General background on duplex stainless steels ..... - 6 -

2.4 LDX 2101 duplex stainless steel ..... - 7 -

2.4.1 Chemical composition of LDX 2101 ..... - 7 -

2.4.2 Alloying elements of LDX 2101 ..... - 8 -

2.4.3 Mechanical properties of LDX 2101 ..... - 11 -

2.5 Welding techniques and weldability ..... - 12 -

2.6 Heat treatment of duplex stainless steels ..... - 13 -

2.7 Weld solidification: Mode of solidification characterisation ..... - 15 -

2.8 Weld solidification defects: Hot cracking ..... - 20 -

2.9 Different types of corrosion of stainless steels ..... - 23 -

2.9.1 General corrosion ..... - 23 -

2.9.2 Localised corrosion ..... - 23 -

2.9.3 Intergranular corrosion ..... - 25 -

2.9.4 Galvanic corrosion ..... - 27 -
2.10 Corrosion of stainless steel alloyed with Ru ..... - 28 -
2.10.1 Effect of Ru addition to corrosion of stainless steel ..... - 28 -
2.11 Mechanism of cathodic modification ..... - 30 -
2.12 Effect of NaCl solution on corrosion of stainless steels ..... - 32 -
2.13 Corrosion rate determination ..... - 34 -
2.14 Cost of 316L ASS compared to LDX 2101 ..... - 38 -
2.15 Background on Ruthenium ..... - 41 -
2.16 Effect of Ru addition to stainless steel ..... - 43 -
Chapter 3 ..... - 44 -
3 Methodology ..... - 44 -
3.1 Introduction ..... - 44 -
3.2 Stage 1: Weld fabrication ..... - 45 -
3.2.1 Gas Tungsten Arc button welds ..... - 45 -
3.3 Stage 2: Material preparation ..... - 46 -
3.3.1 Test samples preparation: Metallography ..... - 46 -
3.3.2 Preparation for metallography ..... - 46 -
3.4 Stage 3: Solidification and Heat treatments ..... - 47 -
3.4.1 Heat treatment of samples ..... - 47 -
3.4.2 Mode of solidification characterisation ..... - 48 -
3.5 Stage 4: Corrosion tests ..... - 50 -
3.5.1 Sample preparation –Corrosion test ..... - 50 -
3.5.2 Potentiodynamic polarisation test ..... - 50 -
3.5.3 Actual test setup technique ..... - 51 -
3.5.4 Open Circuit Potential (OCP) ..... - 51 -
3.5.5 Potentiodynamic polarization ..... - 51 -
3.5.6 Parameters ..... - 51 -
3.5.7 Corrosion rate determination ..... - 52 -
3.6 Stage 5: Post corrosion tests metallography ..... - 53 -
3.6.1 Optical microscope: Pitting corrosion evaluation ..... - 53 -

3.7 Stage 6: Mechanical properties ..... - 54 -
3.7.1 Hardness test: Post GTA welding ..... - 54 -
Chapter 4 ..... - 55 -
4 Results and Discussion ..... - 55 -
4.1 Microstructural evaluation: GTAW button 316L samples ..... - 55 -
4.1.1 Optical Microscope - 316L ASS ..... - 55 -
4.1.2 Spectrometry results for 316L ASS. ..... - 57 -
4.1.3 Scanning Electron Microscope (SEM) and Energy-dispersive X-ray spectroscopy (EDX) analysis ..... - 57 -
316L SEM and EDX results for 316L ASS ..... - 57 -
4.1.4 Mode of Solidification for 316L ..... - 61 -
4.1.5 316L Hardness results ..... - 63 -
4.2 Potentiodynamic results ..... - 64 -
4.2.1 316L Potentiodynamic curves ..... - 64 -
4.2.2 Corrosion rate ..... - 68 -
4.2.3 316L Corrosion rate ..... - 68 -
4.2.4 Pitting Corrosion for 316L ..... - 69 -
4.3 Microstructural evaluation: GTAW button LDX 2101 samples ..... - 72 -
4.3.1 Optical microscope: LDX 2101 duplex stainless steel ..... - 72 -
4.3.2 Spectrometry results for LDX 2101 ..... - 77 -
4.3.3 2101 SEM and EDX results ..... - 77 -
4.4 Hardness results ..... - 81 -
4.4.1 LDX 2101 ..... - 81 -
4.4.2 LDX 2101 Potentiodynamic curves ..... - 82 -
4.5 Corrosion rate ..... - 87 -
4.5.1 LDX 2101 Corrosion rate ..... - 87 -
4.6 Pitting Corrosion results ..... - 89 -
4.7 Comparison of 316L vs LDX 2101 corrosion properties ..... - 91 -
5 Commercial viability ..... - 93 -

6 Conclusions ..... - 94 -
7 Recommendations ..... - 95 -
8 References ..... - 96 -
9 Intellectual property ..... - 104 -
10 Ethics ..... - 104 -
11 Appendix ..... - 105 -
11.1 Appendix A ..... - 105 -
11.2 Appendix B ..... - 105 -
11.3 Appendix C ..... - 106 -
11.4 Appendix D ..... - 108 -
11.5 Appendix E ..... - 110 -
11.6 Appendix F ..... - 111 -
11.7 Appendix G ..... - 112 -
11.8 Appendix H ..... - 113 -
11.9 Appendix I ..... - 114 -
11.10 Appendix J ..... - 115 -
11.10.1 Publication from this work ..... - 115 -

List of Figures

Figure 1: The crystal structures of the three groups of stainless steel a) austenite, b) ferrite and c) martensite (Aung, 2016). ..... - 4 -
Figure 2: The equilibrium phase transition diagram (Pellizzari, et al., 2005) ..... - 14 -
Figure 3: TTT (Time Temperature Transition) curves of DSS grades (BSSA, 2016). ..... - 15 -
Figure 4: The liquidus and solidus projections of the Fe–Cr–Ni system along with the related binaries (Folkard, 1988). ..... - 16 -
Figure 5: Pseudobinary section of the Fe–Cr–Ni ternary diagram at 70% Fe, showing solidification modes (Lippold & Kotecki, 2005). ..... - 17 -
Figure 6: The Schaeffler constitution diagram of 1949 (Schaeffler, 1949). ..... - 18 -
Figure 7: DeLong constitution diagram of 1973, introducing the concept of Ferrite Number (Long & DeLong, 1973). ..... - 19 -
Figure 8: The WRC-92 constitution diagram for weld metal ferrite, including solidification mode boundaries (Siewert & Kotechi, 1992). ..... - 20 -
Figure 9: Modified concept of the effect of constitution on cracking susceptibility in binary systems (Borland, 1960). ..... - 21 -
Figure 10: Intergranular corrosion (weld decay) of stainless steel weldments (ASM International, 2006). ..... - 26 -
Figure 11: Typical polarization curve of Fe-Cr alloy showing effect of cathodic modification (Wolff, 1999). ..... - 29 -
Figure 12: (a) Graphical representation of the effect of addition of cathodic impurity and (b) graphical representation of ways in which cathodic reactions can be retarded by increasing over potential (Potgieter, et al., 1990). ..... - 31 -
Figure 13: Schematic representation of effect of cathodic modification (Potgieter, et al., 1990). ..... - 32 -
Figure 14: Evans Diagram (Frankel, 2016). ..... - 35 -
Figure 15: Schematic distribution of the free energy (Amri, 2009). ..... - 38 -
Figure 16: Nickel stocks vs price from 1990 to 2008 (Papp, et al., 2007). ..... - 39 -
Figure 17: Price of nickel at the London Metal Exchange from Dec ‘2016 to Dec ’2017 (in U.S. dollars per metric ton) (Statisca, 2017). ..... - 40 -
Figure 18: Ruthenium Price over the last 13 years (InfoMine Inc, 2017) ..... - 42 -
Figure 19: (a) The copper hearth for compact vacuum arc melting system, (b) schematic of spherical button weld and (c) cross sectional view of mounted sample. ..... - 45 -

Figure 20: TTT Diagram of Outokumpu duplex stainless steel LDX 2101® and the heat treatment utilised (British Stainless Steel Association, 2016). ..... - 48 -
Figure 21: Linear Polarisation Resistance curve (K.A.Natarajan, 2012). ..... - 53 -
Figure 22: Optical micrograph of 316L ASS as-received standard material etched with one part HNO_3, one part HCl and one part H_2O. ..... - 55 -
Figure 24: The SEM back scattered image for 0.1 wt% Ru alloyed 316L button welded sample . . .. - 57 -
Figure 25: The SEM back scattered image for 0.5 wt% Ru alloyed 316L button welded sample. . ..... - 58 -
Figure 26: The SEM back scattered image for 1 wt% Ru alloyed 316L button welded sample. .... - 58 -
Figure 27: The SEM back scattered image for 2 wt% Ru alloyed 316L button welded sample. .... - 59 -
Figure 28: EDX analysis of matrix region of the 2 wt% Ru sample. ..... - 59 -
Figure 29: Schaeffler diagram for stainless steel weld metal (British Stainless Steel Association, 2016). ..... - 61 -
Figure 29: Vickers hardness test results for different Ru additions for the GTAW 316L button samples at: 0.1 wt%, 0.5 wt %, 1 wt % and 2 wt % Ru additions. ..... - 63 -
Figure 30: Potentiodynamic polarisation curves for 0.1 wt%, 0.5 wt%, 1 wt% and 2 wt% Ru addition to 316L GTA welded buttons in 1M NaCl. ..... - 64 -
Figure 31: The potentiodynamic polarisation curves of E vs log (i) for standard 0wt% Ru addition GTAW 316L button weld and 0.5 wt% Ru addition. ..... - 65 -
Figure 32: The potentiodynamic polarisation curves of E vs log (i) for standard 0 wt% Ru addition GTAW 316L button weld and 1 wt% Ru addition. ..... - 66 -
Figure 33: The potentiodynamic polarisation curves of E vs log (i) for standard 0 wt% Ru addition GTAW 316L button weld to 2 wt% Ru addition. ..... - 67 -
Figure 34: Surface of the 0.1 wt% Ru 316L corroded sample after potentiodynamic polarisation in 1 M NaCl. ..... - 70 -
Figure 35: Surface of the 0.5 wt% Ru 316L corroded sample after potentiodynamic polarisation in 1 M NaCl. ..... - 70 -
Figure 36: Surface of the 1 wt% Ru 316L corroded sample after potentiodynamic polarisation in 1 M NaCl. ..... - 71 -
Figure 37: Surface of the 2 wt% Ru 316L corroded sample after potentiodynamic polarisation in 1 M NaCl. ..... - 71 -

Figure 38: Optical micrograph of LDX 2101 as-received standard material etched with one part HNO_3, one part HCl and one part H_2O. ..... - 72 -
Figure 39: 0.1 wt% Ru in LDX 2101 DSS before heat treatment etched with one part HNO_3, one part HCl and one part H_2O. ..... - 73 -
Figure 40: 0.1 wt% Ru in LDX 2101 DSS after heat treatment etched with one part HNO_3, one part HCl and one part H_2O. ..... - 74 -
Figure 41: Micrograph of 0.1 wt% Ru addition into LDX 2101 GTAW buttons etched with one part HNO_3, one part HCl and one part H_2O. ..... - 75 -
Figure 42: Micrograph of 0.5 wt% Ru addition into LDX 2101 GTAW buttons etched with one part HNO_3, one part HCl and one part H_2O. ..... - 75 -
Figure 43 : Micrograph of 1 wt% Ru addition into LDX 2101 GTAW buttons etched with one part HNO_3, one part HCl and one part H_2O. ..... - 76 -
Figure 44: Micrograph of 2 wt% Ru addition into LDX 2101 GTAW buttons etched with one part HNO_3, one part HCl and one part H_2O. ..... - 76 -
Figure 45: The SEM back scattered image for 0.1 wt% Ru alloyed LDX 2101 button welded sample..... - 77 -
Figure 46: The SEM back scattered image for 0.5 wt% Ru alloyed LDX 2101 button welded sample..... - 78 -
Figure 47: The SEM back scattered image for 1 wt% Ru alloyed LDX 2101 button welded sample. ..... - 78 -
Figure 48: The SEM back scattered image for 2 wt% Ru alloyed LDX 2101 button welded sample. ..... - 79 -
Figure 49: Schaeffler diagram for stainless steel weld metal (British Stainless Steel Association, 2016). ..... - 81 -
Figure 50: Vickers hardness test results for different Ru additions for the LDX 2101 button samples at: 0.1 wt%, 0.5 wt%, 1 wt% and 2 wt% Ru additions. ..... - 82 -
Figure 51: Potentiodynamic polarisation curves for 0.1 wt%, 0.5 wt%, 1 wt% and 2 wt% Ru addition to LDX 2101 DSS GTA welded buttons in 1M NaCl. ..... - 83 -
Figure 52: The potentiodynamic polarisation curve (E vs log (i)) for the standard 0 wt% Ru addition GTAW LDX 2101 button weld compared with the 0.5 wt% Ru sample. ..... - 84 -
Figure 53: The potentiodynamic polarisation curves (E vs log (i)) for the standard 0 wt% Ru addition GTAW LDX 2101 button weld compared with the 1 wt% Ru sample. ..... - 85 -
Figure 54: The potentiodynamic polarisation curves (E vs log (i)) for the standard 0 wt% Ru addition GTAW LDX 2101 button weld compared with the 2 wt% Ru sample. ..... - 86 -

Figure 55: Surface of the 0.1 wt% Ru LDX 2101 corroded sample after potentiodynamic polarisation in 1 M NaCl. ..... - 89 -
Figure 56: Surface of the 0.5 wt% Ru LDX 2101 corroded sample after potentiodynamic polarisation in 1 M NaCl. ..... - 90 -
Figure 57: Surface of the 1 wt% Ru LDX 2101 corroded sample after potentiodynamic polarisation in 1 M NaCl. ..... - 90 -
Figure 58: Surface of the 2 wt% Ru LDX 2101 corroded sample after potentiodynamic polarisation in 1 M NaCl. ..... - 91 -
Figure 59: Comparative potentiodynamic polarisation curve for 1 wt% Ru addition to 316L ASS verse LDX 2101 DSS. ..... - 92 -
Figure 60: Corrosion rate comparison in mm/yr for 316L ASS and LDX 2101 ..... - 92 -
Figure 61: Mechanical properties vs Corrosion Resistance of LDX 2101 DSS compared to standard stainless steels (Outokumpu, 2014). ..... - 105 -
Figure 62: Back scattered image for EDX containing Ti. ..... - 105 -
Figure 63: EDX analysis spectrum for 2 wt% Ru addition to 316L ASS. ..... - 106 -
Figure 64 : EDX spectrum for 0.1 wt% Ru addition to LDX 2101. ..... - 106 -
Figure 65 : EDX spectrum for 0.5 wt% Ru addition to LDX 2101. ..... - 107 -
Figure 66: EDX spectrum for 1 wt% Ru addition to LDX 2101. ..... - 107 -
Figure 67: EDX spectrum for 2 wt% Ru addition to LDX 2101. ..... - 108 -
Figure 68: Potentiodynamic curves of 0.1 wt% Ru addition to 316L in 1M NaCl. ..... - 108 -
Figure 69: Potentiodynamic curves of 0.5 wt% Ru addition to 316L in 1M NaCl. ..... - 108 -
Figure 70: Potentiodynamic curves of 1 wt% Ru addition to 316L in 1M NaCl. ..... - 109 -
Figure 71: Potentiodynamic curves of 2 wt% Ru addition to 316L in 1M NaCl. ..... - 109 -
Figure 72: Potentiodynamic curves of 0.1 wt% Ru addition to LDX 2101 in 1M NaCl. ..... - 110 -
Figure 73: Potentiodynamic curves of 0.5 wt% Ru addition to LDX 2101 in 1M NaCl ..... - 110 -
Figure 74: Potentiodynamic curves of 1 wt% Ru addition to LDX 2101 in 1M NaCl. ..... - 110 -
Figure 75: Potentiodynamic curves of 2 wt% Ru addition to LDX 2101 in 1M NaCl. ..... - 110 -
Figure 76: Tafel extrapolation of 0.1 wt% Ru addition to 316L in 1M NaCl. ..... - 111 -
Figure 77: Tafel extrapolation of 0.5 wt% Ru addition to 316L in 1M NaCl. ..... - 111 -
Figure 78: Tafel extrapolation of 1 wt% Ru addition to 316L in 1M NaCl. ..... - 111 -
Figure 79: Tafel extrapolation of 2 wt% Ru addition to 316L in 1M NaCl. ..... - 111 -
Figure 80: Tafel extrapolation of 0.1 wt% Ru addition to LDX 2101 in 1M NaCl. ..... - 112 -
Figure 81: Tafel extrapolation of 0.5 wt% Ru addition to LDX 2101 in 1M NaCl. ..... - 112 -
Figure 82: Tafel extrapolation of 1 wt% Ru addition to LDX 2101 in 1M NaCl. ..... - 113 -

Figure 83: Tafel extrapolation of 2 wt% Ru addition to LDX 2101 in 1M NaCl. .....- 113 -
Figure 84: Linear polarisation resistance of 0.1 wt% Ru addition to 316L in 1M NaCl .....- 113 -
Figure 85: Linear polarisation resistance of 0.5 wt% Ru addition to 316L in 1M NaCl .....- 113 -
Figure 86: Linear polarisation resistance of 1 wt% Ru addition to 316L in 1M NaCl .....- 113 -
Figure 87: Linear polarisation resistance of 2 wt% Ru addition to 316L in 1M NaCl .....- 113 -
Figure 88: Linear polarisation resistance of 0.1 wt% Ru addition to LDX 2101 in 1M NaCl. - 114 -
Figure 89: Linear polarisation resistance of 0.5 wt% Ru addition to LDX 2101 in 1M NaCl. - 114 -
Figure 90: Linear polarisation resistance of 1 wt% Ru addition to LDX 2101 in 1M NaCl. ...- 114 -
Figure 91: Linear polarisation resistance of 2 wt% Ru addition to LDX 2101 in 1M NaCl. ...- 114 -

List of Tables

Table I: Chemical composition of 316L ASS (Peckner & Bernstein, 1977) and (Davis, 1994). - 5 -
Table II: Mechanical properties of 316L ASS (Davis, 1994). ..... - 6 -
Table III: Chemical composition of LDX 2101 (Young.C.A., 2008). ..... - 8 -
Table IV: Mechanical properties of LDX 2101(Young.C.A., 2008). ..... - 12 -
Table V: Physical and Mechanical Properties of Ruthenium (AZoM, 2013). ..... - 42 -
Table VI: The spectrometry results of 316L ASS as received. ..... - 57 -
Table VII: Chemical Compositions of GTAW 316L button samples alloyed with 2 wt% Ru analysed by EDX. ..... - 60 -
Table VIII: The Creq to Nieq ratios of as received samples for 316L and Ru containing alloys .... - 62 -
Table IX: Potentiodynamic polarization data for 316L. ..... - 68 -
Table X: Potentiodynamic polarization corrosion rate data for 316L using linear polarisation .... - 69 -
Table XI: Volume fraction of LDX 2101 DSS using quantitative metallurgy. ..... - 73 -
Table XII: Volume fraction of LDX 2101 DSS using quantitative metallurgy. ..... - 74 -
Table XIII: The spectrometry results elemental composition for LDX 2101. ..... - 77 -
Table XIV: Chemical Compositions (wt %) of LDX 2101 button samples alloyed increasing Ru analysed by EDX analysis. ..... - 79 -
Table XV: The Cr_{eq} to Ni_{eq} ratios of as received samples for LDX 2101 and Ru containing alloys. ..... - 80 -
Table XVI: Potentiodynamic polarization data for LDX 2101. ..... - 87 -
Table XVII: Potentiodynamic polarization corrosion rate data for LDX 2101 using linear polarisation. ..... - 88 -

List of Equations

Equation 1……..- 15 -
Equation 2……..- 15 -
Equation 3……..- 15 -
Equation 4……..- 15 -
Equation 5……..- 18 -
Equation 6……..- 18 -
Equation 7……..- 25 -
Equation 8……..- 25 -
Equation 9……..- 28 -
Equation 10……..- 34 -
Equation 11……..- 34 -
Equation 12……..- 34 -
Equation 13……..- 34 -
Equation 14……..- 34 -
Equation 15……..- 34 -
Equation 16……..- 34 -
Equation 17……..- 36 -
Equation 18……..- 37 -
Equation 19……..- 37 -
Equation 20……..- 37 -
Equation 21……..- 37 -
Equation 22……..- 50 -
Equation 23……..- 50 -
Equation 24……..- 53 -
Equation 25……..- 62 -
Equation 26……..- 62 -

Chapter 1

1.1 Introduction

Over the years corrosion has cost the stainless steel industry extensive amounts of money in maintenance and mechanical failures particularly at welded points. These economic losses have been experienced in the infrastructure, transportation, production and manufacturing industries. There are different forms of corrosion that occur in stainless steel welds such as: pitting, stress corrosion cracking (SCC), intergranular, also known as weld decay, and galvanic corrosion (Wahid, et al., 1993). The passivity of stainless steels depends on the chromium content to provide a protective oxide film at the corrosion surface. Due to the harmful effects that chromium (Cr) VI emissions have on human health during welding, there is a growing need in the welding industry to develop a Cr free consumable and Cr free weld filler. This has led to the need for newly designed Cr-free consumables and modified welds that would have to be more cost effective and corrosion resistant than the standard products currently available in industry. Research from 1978 by a group of Russian investigators, Chernova and Tomashov showed that a small addition of platinum group metals (PGM's) to the weld metal of stainless steel caused the cathodic potential to spontaneously move to the passive region through a phenomenon known as "cathodic modification" thus protecting the stainless steel from corrosion (Chernova, et al., 1978). Previous research has revealed that the corrosion resistance, particularly pitting corrosion, significantly increased by alloying with low concentrations of PGMs (Sherif, et al., 2009). Lippold and Frankel (2009) at Ohio University looked at creating a Cr free consumable with Ni-Cu baseline and the addition of a variety of PGM's solely for 304L stainless steel. Liang, et al. (2010) also showed that the addition of small amounts of ruthenium (Ru) improved the corrosion resistance of 304L austenitic stainless steel (ASS).

In South Africa the PGM's that are mined contain on average 11% Ru while the PGMs mined in the former Union of Soviet Socialist Republic (USSR) contain only 2% Ru based on research dating from 1992 by (Matthews, 2007). Ruthenium is the least expensive PGM retailing at an average low of 40 USD/oz. for the past five years from 2016 (InfoMine Inc, 2017). The discovery of a new application in hard disk drives for Ru in early 2000 resulted in South Africa, the world's biggest source of Ru, benefiting from a surge in foreign exchange earnings. The increase in availability and affordability of Ru in South Africa makes it highly feasible for it to be used in the weld metal of 316L ASS and LDX 2101. However, not much research has been done on the weld metal of 316L austenitic and 2101 duplex stainless steel. In recent years, laser surface alloying

treatments for 316L ASS by addition of Ru and Ni have been investigated and show that the Ru modified alloys possesses properties which render these Ru for modified alloys as suitable replacing the Ni-based alloys (Lekala, et al., 2012). The 316L is a low carbon stainless steel version of the standard 316 stainless steel, and is able to overcome the risk of intergranular corrosion in the form of weld decay. LDX 2101 on the other hand is a lean duplex stainless steel with corrosion resistance superior to 304L and comparable to 316L. LDX 2101 possesses both superior strength and greater chloride stress corrosion cracking resistance than conventional 300 series stainless steels.

The purpose of this study is to investigate the improvement of corrosion resistance and mechanical properties through the addition of Ru to the weld metal of 316L ASS and LDX 2101. Different welds will be prepared using Gas Tungsten Arc Weld (GTAW) button on weld. The SCC, galvanic corrosion, and pitting will be investigated for the 316L stainless steel and LDX 2101 when exposed to a variety of corrosive environments. During corrosion tests the stainless steel was exposed to chloride containing environments namely; sodium chloride (NaCl) (Potgieter, et al., 2014). The mechanical properties of the weld were also evaluated to determine the influence of adding Ru in the weld metal. This was done by evaluating hardness properties. The expectation is that, the addition of Ru to the weld metal should then meet the minimum requirements of the base metal strength level and exhibit adequate or greater mechanical and corrosion properties.

1.2 Problem statement:

In this study the effect of the addition of Ru to the Heat Affected Zones (HAZ) will be evaluated according the following problem statements:

- Welding still remains as a preferred joining mechanism for high strength steels such as austenitic and duplex stainless steel.
- Corrosion at weld joints has caused significant economic losses in industry, increasing the need for maintenance and equipment failures.
- Mechanical failures at weld joints still pose large safety risk due to the poor understanding of microstructural changes occurring during welding of stainless steels
- Cost has been a major hindering factor to the alloying of stainless steels with PGMs to improve corrosion resistance.

- The feasibility of additions of small quantities of PGMs to stainless steels to improve their general corrosion in reducing acidic environments has not produced conclusive results (Higginson, 1989).
- The comparative study on the mechanical and corrosion properties of 316L weld metal as compared to LDX 2101 weld metal needs to be understood.

- Prospect of a commercially viable stainless steel alloyed with Ru due to its lower cost than other PGM'S is hoped to make this material commercially viable in South Africa.

1.3 Research objectives:

In this study the aim would be to determine if the addition of Ru to the weld metal of 316L austenitic and LDX 2101 duplex stainless steel, will improve the corrosion resistance and mechanical properties of the weld metal. This aim will be achieved by the following objectives:

- Evaluating what the addition of Ru via GTA welding has on the microstructures of 316L and LDX 2101 stainless steel.
- To determine the influence of Ru additions to the weld metal on the corrosion rate, corrosion potential and open circuit potential.
- Compare the pitting corrosion resistance of 316L and LDX 2101 stainless steel after Ru addition to weld metal
- Determine the mechanical properties of the weld metal of button melted welds for 316L vs LDX 2101, once increasing amounts of Ru have been added.

Chapter 2

2 Literature review

Stainless steels are divided into three groups according to their crystal structures: austenitic (face-centered cubic, fcc), ferritic (body-centered cubic, bcc) and martensitic (body-centered tetragonal or cubic, bct) (www.nsalloys.com, 2011). Stainless steels containing both austenite and ferrite usually in roughly equal amounts are known as “duplex stainless steels”. This study considers the effect of Ru addition to the weld metal of 316L austenitic stainless steel on the corrosion and mechanical properties compared to LDX 2101.

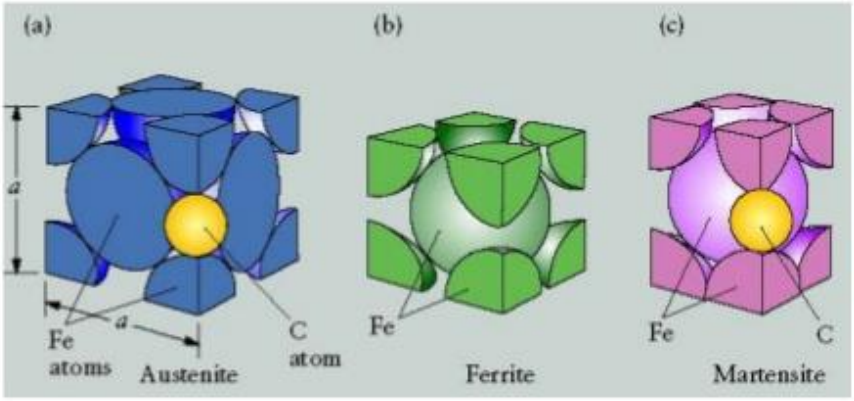


Figure 1: The crystal structures of the three groups of stainless steel a) austenite, b) ferrite and c) martensite (Aung, 2016).

2.1 General background on austenitic stainless steels

Austenitic stainless steels (ASSs) are not hardenable by heat treatment; they contain significant levels of Cr and Ni with low levels of carbon. ASSs are known for their high ductility and toughness with low tensile strengths. The Face Centered Cubic (FCC) atomic structure of ASS ensures greater ductility as the FCC structure contains more favourable planes for the movement of dislocations. ASS exhibit superior corrosion resistance, but in highly reactive and aggressive surroundings they can undergo acute corrosion (Davis, 1994). The ASSs are fundamentally nonmagnetic in the annealed state and can be hardened only by cold working. ASSs generally have low yield strengths but after cold working their yield strengths can significantly improve. Typically a small amount of cold work has the potential to increase the yield by an amount of 200 or 300 MPa and in severely cold worked material like spring temper wire or strip the yield strength

is usually about 80-95% of the tensile strength. This sharp increase in some cases is due to the formation of stress induced martensite (Milada, et al., 2007).

2.2 AISI 316L austenitic stainless steel

In this section the chemical composition and the mechanical properties of 316L ASS will be discussed.

2.2.1 Chemical Composition of the AISI 316L

The 316L ASS is a standard molybdenum-containing grade; amongst the family of austenitic stainless steels the 316L ASS is considered to be second in importance to the 304L ASSs. The low carbon content in 316L ASS lowers the probability of forming carbide precipitates in the welding process. This means that the stainless steel is resistant to sensitization. The presence of molybdenum (Mo) in 316L ASS gives better overall corrosion resisting properties than 304L ASS (Desu, et al., 2014). Therefore, 316L ASS is more resistant to corrosion in chloride rich environments and in particular 316L ASS has a higher resistance to pitting and crevice corrosion. Table I shows the chemical composition of 316L ASS.

Table I: Chemical composition of 316L ASS (Peckner & Bernstein, 1977) and (Davis, 1994).

AISI type	Maximum Nominal compositions (%)								
	Cr	Ni	C	Si	Mn	P	S	N	Mo
316L	16.0-18.0	10-14	0.03	1	2	0.045	0.03	0.10	2-3

2.2.2 Mechanical Properties of the 316L ASS

Austenitic stainless steels that have been annealed show a low yield strength in comparison to the tensile strength. Small degrees of cold work can significantly increase the yield strength. However, the yield strength also increases with a higher degree of tensile strength. In some instances the sharp increase in yield strength is due to the formation of stress induced martensite (Milada, et al., 2007). The formation of stress induced martensite depends on the stability of

austenite. With a decrease in stability of austenite a greater tendency exists for the formation of stress induced martensite (Milada, et al., 2007). Compared to 304L, 316L stainless steel offers higher creep resistance, stress to rupture and tensile strength at elevated temperatures (Klar & Samal, 2007). The mechanical properties of the 316L stainless steel are included in the Table II.

Table II: Mechanical properties of 316L ASS (Davis, 1994).

Grade	Tensile Strength (MPa) min	Yield Strength 0.2% Proof (MPa) min	Elongation (% in 50mm) min	Hardness	
				Rockwell B (HR B) max	Brinell (HB) max
316L*	517	206	40	95	217

***** Minimum mechanical properties for plate in thicknesses greater than 0.25 inch per ASTM A 240.

The 304L ASSs are commonly used particularly in the home, oil, gas and commercial industries. However, 316L ASS is used in the pharmaceutical industry, food, petroleum and chemical handling, because of its improved corrosion resistance (Peckner & Bernstein, 1977).

2.3 General background on duplex stainless steels

Duplex stainless steels are about twice as strong as standard austenitic or ferritic stainless steels. Their strength has made them a preferred alternative to conventional austenitic and ferritic stainless steel. In addition, they have significantly better toughness and ductility than ferritic grades. However, they do not reach the high toughness and ductility of austenitic grades. The corrosion resistance of duplex stainless steels depends mostly on the composition of the stainless steel. For chloride pitting and crevice corrosion resistance, their chromium, Mo and Ni content are important. A range of duplex stainless steel grades exist with a variety of corrosion resistances, similar to the range for austenitic stainless steels. For example, Type 304 ASS has alternative material such as 316 ASS which can be used as an alternative. Similarly, LDX 2101 can be utilized as an alternative to 6% Mo containing steel such as SAF 2507.

There are different types of duplex stainless steel such as:

- Lean duplex SS that are lower in nickel with no Mo (e.g. 2101, 2102, 2202, 2304),
- Standard duplex refers to duplex SS that are higher in Ni and Mo (e.g. 2205, 2003, 2404),
- Super duplex SS which usually contain 25% Cr and higher Ni and Mo "plus" (e.g. 2507, 255 and Z100), and
- Hyper duplex which refers to grades that have more Cr, Ni, Mo and N such as 2707 (Grocki.J, 2012).

2.4 LDX 2101 duplex stainless steel

In this section the chemical composition and the mechanical properties of LDX 2101 will be discussed.

2.4.1 Chemical composition of LDX 2101

LDX 2101 is a low-Ni; nitrogen enhanced lean duplex stainless steel developed for general-purpose use with corrosion resistance superior to 304L and comparable to 316L. This lean duplex LDX 2101 was created by Outokumpu in order to offer the market a stainless steel for light weight constructions, suitable for use in environments where other duplex stainless steels had been more prone to corrosion (Alfonsson, 2010). The purpose was to replace other duplex stainless steels like 2205 (UNS S31803/32205) which was developed and introduced by the German steel producer Krupp in the mid-1970's (Jan & Snis, 2006). This stainless steel grade was the first "second generation" duplex steel to be developed commercially and is the most commonly used to date. The new lean duplex stainless steels, unlike 2205, contain fewer alloying elements and are intended for applications in which their properties would be similar to 304 or 316 ASS grades (Alvarez-Armas, 2008). The resultant LDX 2101 that was developed was a resilient, adaptable and distinct high performance stainless steel. In terms of downstream utilisation throughout its life cycle the LDX 2101 is highly cost efficient when compared to other many competing materials such as 2205. This lean duplex stainless steel contains sufficient ferritic material to provide outstanding engineering properties as it is easy to machine. Additionally the austenitic content of LDX 2101 ensures that it is corrosion resistant and the phase balance between these two characteristics gives it the improved strength.

Table III shows the typical chemical composition of LDX 2101 lean duplex steel.

Table III: Chemical composition of LDX 2101 (Young.C.A., 2008).

Grade	Type	Maximum Nominal Composition						
		Cr	Ni	Mo	N	Mn	W	Cu
2101 LDX	Lean	21.5	1.5	0.3	0.22	5	-	-

As previously stated the LDX 2101 has fewer alloying elements and due to its relatively low alloying content, LDX 2101 is less prone to precipitation of intermetallic phases than other duplex steels such as 2205. Duplex stainless steels have lower nickel and molybdenum contents than their austenitic counterparts of similar corrosion resistance. Due to the lower alloying content, the duplex stainless steels are lower in cost, especially with the high price of Ni.

2.4.2 Alloying elements of LDX 2101

Alloying elements are added to stainless steels to improve properties. In this study the properties of concern were corrosion resistance and mechanical properties. Chromium which is the most important alloying element for stainless steel needs to be a minimum content of 10.5 wt% to create and maintain the passive film, which enables the material to be corrosion resistance. Other elements such as Ni, N and Mo are also added for corrosion resistance. Whereas C, Mo, N, titanium (Ti), aluminium (Al) and copper (Cu) are added for strength. Lastly sulphur (S) and selenium (Se) are added for machinability; and Ni is added for formability and toughness. Nickel assists in obtaining an austenitic microstructure which is far less prone to the loss of toughness from a large grain size.

2.4.2.1 Chromium

Chromium (Cr) plays an import role in most conventional stainless steels, it provides the stainless steel with its corrosion resistance capabilities. Chromium is responsible for the formation of a spontaneous protective passivation layer when a stainless steel is introduced to an aggressive environment. Normally the Cr content needs to be a minimum of 10.5 wt% to maintain and develop a passive film for corrosion resistance. Duplex grades normally contain comparatively high levels of Cr, typically 20–29 wt% Cr, which stabilises the ferrite phase.

2.4.2.2 Molybdenum (Mo)

Molybdenum (Mo) slightly increases mechanical strength of stainless steels and strongly promotes a ferritic microstructure. As a large atom, Mo increases the elevated temperature strength of stainless steels through solid solution hardening. Molybdenum also increases the risk of formation of secondary phases in duplex and austenitic stainless steels. In terms of corrosion resistance, Mo significantly increases the localized and general corrosion resistance. This is done by improving resistance of the passive film to resist breakdown, Mo can also enhance repassivation characteristics by reducing the active dissolution rate of the bare metal inside the pits (Hazza & El-Dahshan, 1995). However, due to the complexity of the chemistry of Mo, it makes it difficult to determine the nature of its influence of corrosion resistance.

2.4.2.3 Nickel

Nickel (Ni) is a deliberate alloying element in almost all commercial duplex stainless steels. With regards to mechanical properties Ni generally increases ductility and toughness. The main reason for adding nickel is to promote an austenitic microstructure. Even during post welding cooling Ni promotes austenite formation. The price of Ni increased substantially over the last year (2017) according to the London Metal Exchange (LME). Therefore, in DSS with high Ni contents, the austenitic types lead to price volatility which is non desirable to many end users. There has been a great deal of research into replacing Ni with other austenizing elements, such as carbon, nitrogen, manganese and copper (Lula, 1986).

2.4.2.4 Nitrogen

Nitrogen (N) has low solubility in ferrite and therefore is concentrated in the austenite. When Ni partial pressure in the atmosphere increases, the Ni content increases and the ferrite content decreases. High Ni contents result in rapid re-formation of austenite during weld thermal cycles. Nitrogen improves localized corrosion resistance particularly in chloride containing solutions. It further enhances fatigue properties, and improves creep properties particularly when considering heat treatment (Hertzman & Charles, 2011). In terms of mechanical properties an increase in

nitrogen enhances the Ultimate Tensile Strength (UTS) and reduces the ductility of the material slightly.

2.4.2.5 Manganese

Manganese (Mn) additions to stainless steels also increase the solubility of nitrogen in the molten state. Manganese addition to stainless steels has the benefit of being an austenite-former. In duplex stainless steel (DSS) manganese is added to form and stabilise the austenite phase as it extends the austenite loop and stabilizes at room temperature. It can be concluded that manganese is a useful substitute for NI in duplex alloys; it also has the advantage of being less expensive than nickel. Further work is required before the present alloys, or variations of them, could be commercially viable mainly because manganese is a weaker austenite former than Ni and has to be added in larger amounts to produce a fully austenitic microstructure. For improvement of corrosion resistance, reducing Mn content in stainless steels has proven to be a successful strategy for increasing the pitting corrosion resistance of stainless steels. Manganese is known through the formation manganese sulphide inclusions, to be detrimental to stainless steels pitting corrosion resistance (Gross & Robinson, 1981).

2.4.2.6 Copper

Copper (Cu) is an example of an element that has some austenite forming ability, it is usually added to steels as a residual element. It is added to a few alloys to produce precipitation hardening properties for improved machinability. In duplex stainless steel alloying with Cu has the harmful effect on the localized corrosion resistance in the noble potential range. Copper additions are found to reduce the corrosion rate of alloys in solutions of reducing acids, especially sulphuric acid (Solomon & Devine, 1983). The mechanism of corrosion appears to involve the precipitation of metallic copper on the surface of the alloy, and the consequent movement of the corrosion potential into the passive range (Nana & Cortie, 1993). The addition of copper to austenitic and duplex stainless steels improves the pitting behaviour in sodium chloride (NaCl) solutions.

2.4.2.7 Tungsten

Tungsten (W) is present as an impurity in most stainless steels, although it is added to some special grades to improve pitting corrosion resistance. The effect of W on localized corrosion resistance has not been studied to the same extent as other alloying elements such as Cr, Mo, and N. There is still a strong driving force for adding these elements that contribute to improved corrosion resistance. Tungsten can either be ineffective or detrimental when added to provide greater strength, toughness, corrosion and heat resistance of steel (Haugan, et al., 2017).

2.4.2.8 Carbon

Carbon (C) is a strong austenite former that also significantly increases mechanical strength. In duplex stainless steels, carbon is kept to very low levels (C < 0.03%). In LDX 2101 carbon is kept at a minimum. When alloys are rapidly cooled and contain high levels of carbon, after heat treatments as a result of welding, it leads to unwanted precipitation of chromium containing carbides causing sensitization (Brytan & Niagaj, 2016).

2.4.3 Mechanical properties of LDX 2101

For the DSS to have high mechanical strength, good toughness, and corrosion resistance and weldability a fine balance is required between the different alloying elements is needed (Pilhagen & Sandström, 2014). LDX 2101 possesses both superior strength and greater chloride stress-corrosion cracking resistance than conventional 300 series stainless steels. The high chromium and nitrogen content of LDX 2101, combined with an addition of molybdenum, provide very good resistance to localized and uniform corrosion. This lean duplex stain less steel contains enough ferritic material to provide outstanding engineering properties as it is easy to machine and simple to weld. This is due to the fact that LDX 2101 exhibits good abrasion and erosion resistance and can be fabricated using standard machine practices developed for duplex stainless steels. Additionally the austenitic content of LDX 2101 ensures that it is corrosion resistant and the phase balance between these two characteristics gives it an unyielding strength. Table IV shows the mechanical properties of LDX 2101 duplex stainless steel grade used in this study.

Table IV: Mechanical properties of LDX 2101(Young.C.A., 2008).

Grade	Tensile Strength (MPa) min.	Yield Strength 0.2% Proof (MPa) min.	Elongation (% in 50mm) min.	Hardness	
				Rockwell B (HRB) max.	Brinell (HB) max.
LDX 2101*	650	450	30	-	290

*Minimum (min) mechanical properties for plate in thicknesses greater than 0.25 inch per ASTM A 240.

LDX 2101 exhibits high tensile strength, this high tensile strength also implies high fatigue strength. Despite very high strength at room temperature the duplex steel is susceptible to embrittlement and decrease of mechanical properties, through prolonged exposure to high temperatures. Therefore, it is not advisable to use this stainless steel in high temperature applications. Nevertheless, this superior mechanical strength of LDX 2101 enable the end user to utilize the material in thinner gauge form which inevitable results in cost savings for the user as compared to using conventional 3xxx series alloys.

2.5 Welding techniques and weldability

All fusion welding methods can be used for welding duplex stainless steels on condition that suitable welding procedures and consumables are used. The typical welding techniques adopted in industry for 316L ASS however are:

2.5.1.1 Gas Tungsten Arc Welding (GTAW):

GTAW is a process that uses an external gas supply and non-consumable tungsten electrode to produce an arc that melts the filler wire and fuses the metal to be welded also known as TIG welds (Salmon, 2014).

2.5.1.2 Shielded Metal Arc Welding (SMAW):

SMAW is also known as Manual Metal Arc Welding (MMA or MMAW), flux shielded arc welding or informally as stick welding. It is a manual arc welding process that uses a consumable electrode covered with a flux to lay the weld (Salmon, 2014).

2.5.1.3 Gas metal arc welding (GMAW) processes:

GMAW is also referred to by its subtypes Metal Inert Gas (MIG) welding or Metal Active Gas (MAG) welding, is a welding process in which an electric arc forms between a consumable wire electrode and the work piece metal(s), which heats the work piece metal(s), causing them to melt, and join (Vashisth, 2015).

The occurrence of corrosion at weld joints created using the methods mentioned previously has caused significant economic losses in industries. The economic losses have been influenced by the increased need for maintenance and equipment failures (Van der Merwe & Tharandt, 2015). To prevent these economic losses, Lippold and Frankel (2009) investigated alternative welding electrode consumables, standardization of welding techniques to avoid the influence of human error. They subsequently found that a Cr free consumable could be developed namely the Ni–Cu–Pd welding consumables (Lippold & Frankel, 2009). These consumables have been recently developed solely for 300-series austenitic stainless steels such as 304L ASS. A later study by the Ohio State University in 2010 (Liang, et al., 2010) investigated the effect of Ru additions on corrosion resistance of 304 ASS when added into a modified filler metal instead of Pd. Ruthenium fulfilled all the requirements for a modified filler metal; to primarily decrease the cost implication and increase the corrosion resistance. Actual Ni–Cu–Ru arc welds made on 304L ASS were successfully produced and the corrosion performance was comparable to or better than that of Ni–Cu–Pd welds (Liang, et al., 2010). It is for this reason that Ru addition in ASS weld metal has found relevance in literature studies.

2.6 Heat treatment of duplex stainless steels

Duplex stainless steels cannot be hardened by heat treatment. However, a balanced microstructure of dual phases is essential for DSS that have undergone welding. As higher annealing temperatures are used, the ferrite content will increase. Formation of intermetallic

phases, such as sigma, can occur in the temperature range 593-954°C. There is the increased risk of 475°C embrittlement. In 1941, Reidrich and Loib were the first to document the occurrence of embrittlement (Reidrich & Loib, 1941). In 2009 a paper was released by the National Metallurgical Laboratory, which further validated that when the DSS are aged at 475°C the mechanical properties will be significantly be degraded because of 475°C embrittlement (Sahua, et al., 2009). This embrittlement is caused by the decomposition of the alloy to chromium-rich phase and iron-rich phase and thus termed the "475°C embrittlement". Therefore, LDX 2101 duplex stainless steel is preferentially solution annealed at temperature ranges from 1020-1080°C, and rapid cooling is recommended after annealing.

Figure 2 shows the schematic phase transformation diagram of the duplex stainless steel.

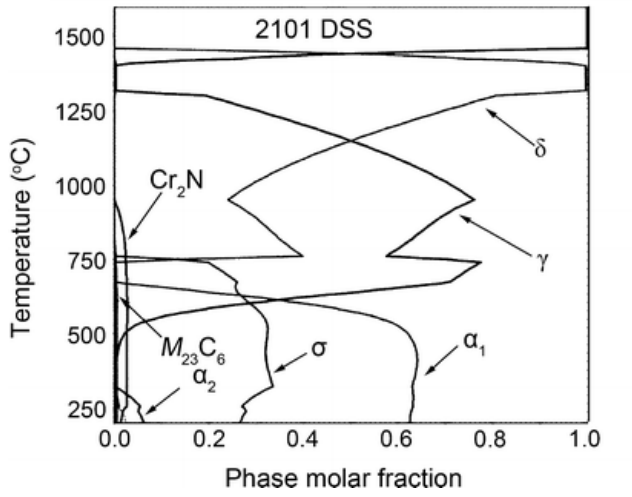


Figure 2: The equilibrium phase transition diagram (Pellizzari, et al., 2005).

LDX 2101 post welding typically requires heat treatment to get a 50:50 balanced phase distribution. Typically quench annealing is an acceptable heat treatment at temperatures at 1020-1080°C where the austenite and ferrite phases are present. The TTT (Time Temperature Transition) curves showing the narrow temperature range at which stress relieving can be performed for some duplex stainless steel grades are shown in Figure 3.

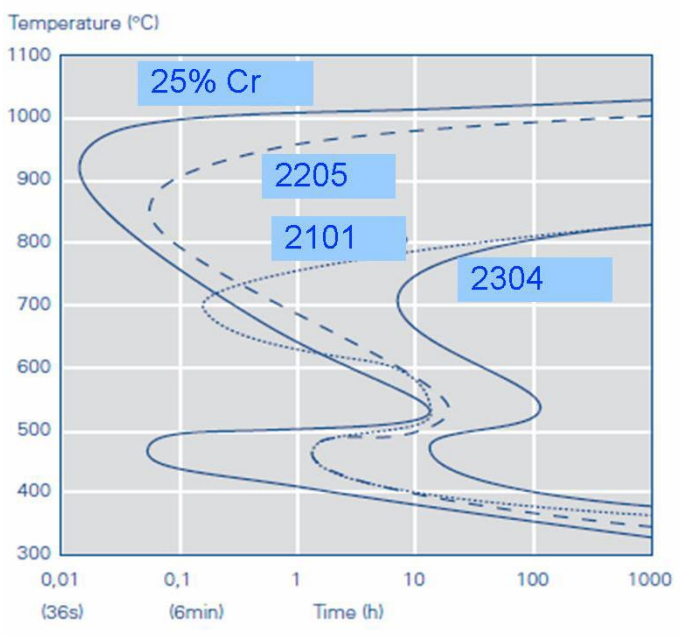


Figure 3: TTT (Time Temperature Transition) curves of DSS grades (BSSA, 2016).

The applied temperature range can be selected based on a TTT diagram in Figure 3. Time-Temperature Transformation (TTT) diagrams obtained from isothermal heat treatment followed by quenching can additionally be used to investigate the susceptibility of DSSs to the σ-phase formation. The heat treatment was based on the recommended solution annealing temperature of 1050°C by the LDX 2101 duplex stainless steel manufacturer Outokumpu in order to achieve a balanced chemical composition and a microstructure containing a fair ferrite austenite solution (Outokumpu, 2014).

2.7 Weld solidification: Mode of solidification characterisation

There are four different solidification modes possible for stainless steel welds: fully austenitic, primary austenitic, primary ferritic and fully ferritic, as shown in the following equations:

$$\mathbf{L \rightarrow L + \gamma \rightarrow \gamma \ (A\ mode)} \qquad \textbf{Equation 1}$$

$$\mathbf{L \rightarrow L + \gamma \rightarrow L + \gamma + \delta \rightarrow \gamma + \delta \rightarrow \gamma \ (AF\ mode)} \qquad \textbf{Equation 2}$$

$$\mathbf{L \rightarrow L + \delta \rightarrow L + \delta + \gamma \rightarrow \delta + \gamma \rightarrow \gamma \ (FA\ mode)} \qquad \textbf{Equation 3}$$

$$\mathbf{L \rightarrow L + \delta \rightarrow \delta \rightarrow \delta + \gamma \ (F\ mode)} \qquad \textbf{Equation 4}$$

where L is the liquid, γ is austenite and δ is delta-ferrite.

Each solidification mode results in distinctive austenite and ferrite morphologies. The mode of solidification of stainless steels is crucial for materials that have undergone any heat inducing fabrication technique, for example welding. This mode of solidification determination is crucial as it controls the weld metal microstructure, grain size, inclusion distribution, porosity, hot-cracking behaviour, and ultimately weld-metal properties (Devletian & Wood, 1983) (David & Vitek, 1993).

A study of the Fe-Cr-Ni phase diagram is required in order to give an understanding of the solidification behaviour of stainless steel welds. Figure 4 depicts the liquidus and solidus projections of the Fe-Cr-Ni system along with the constituent binaries (Folkard, 1988).

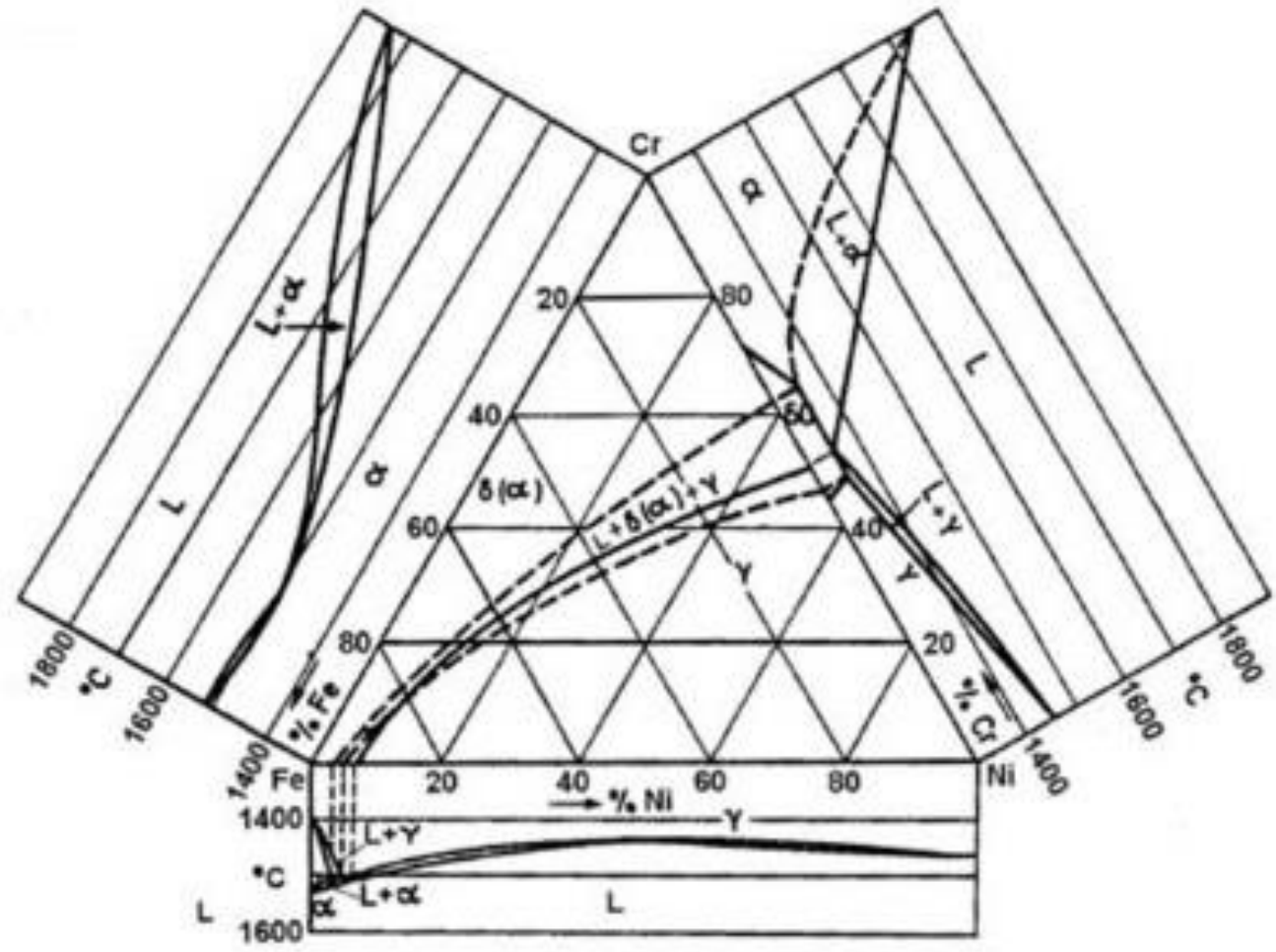


Figure 4: The liquidus and solidus projections of the Fe–Cr–Ni system along with the related binaries (Folkard, 1988).

The approximate composition ranges in which these solidification modes will occur for stainless steels are indicated in Figure 5.

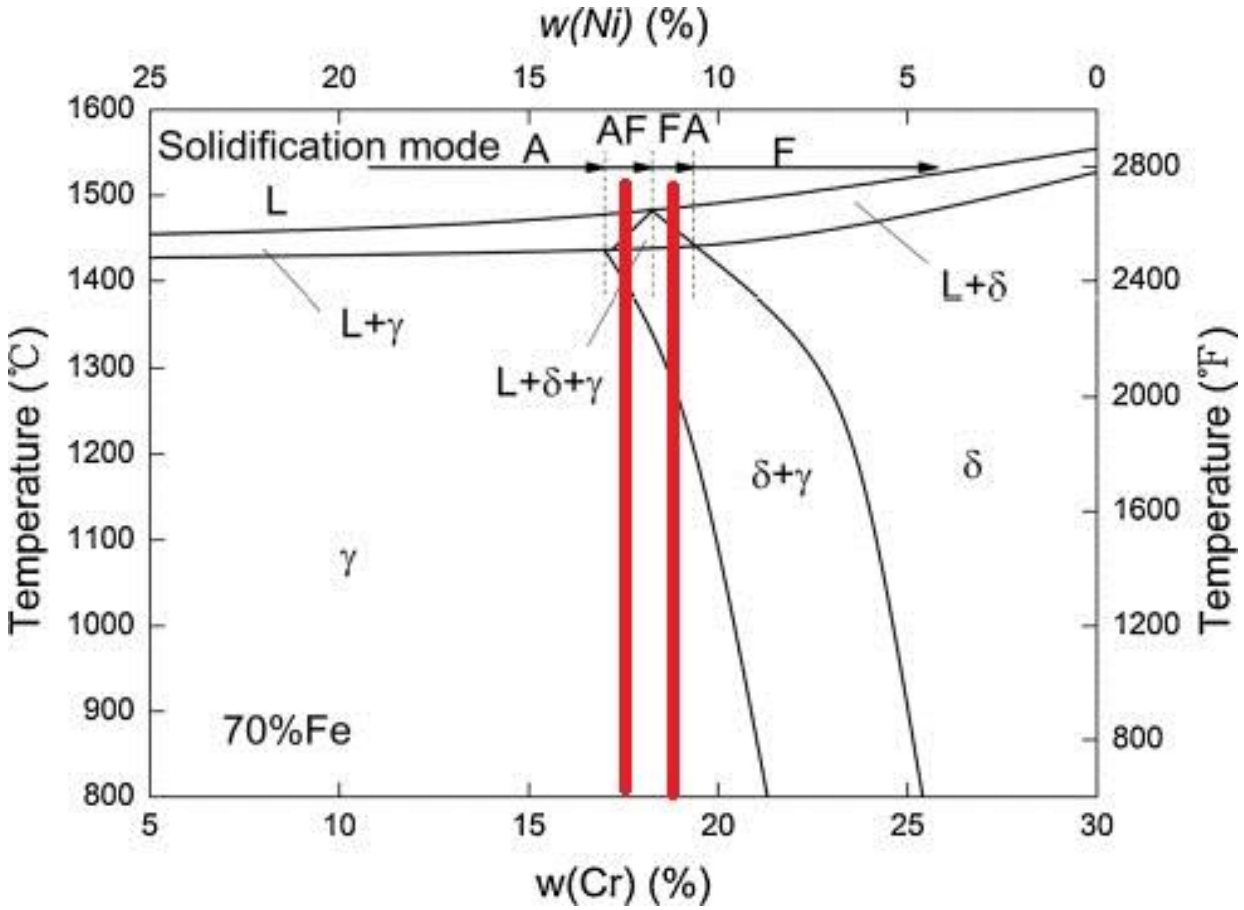


Figure 5: Pseudobinary section of the Fe–Cr–Ni ternary diagram at 70% Fe, showing solidification modes (Lippold & Kotecki, 2005).

Based on these diagrams it has been concluded that most austenitic stainless steel welds and cast metals are designed to form primary ferrite and secondary austenite to minimize the occurrence of hot cracks. This solidification mode is known as the ferritic-austenitic solidification mode (FA mode) (Inoue & Koskei, 2007). Welded alloys that solidify in the FA and F modes pass through the δ to γ two phase regions and may re-enter the single-phase austenite region. This is due to the asymmetry of the two-phase field towards the primary ferritic side of the diagram, as seen in Figure 5 (Olson, 1985). Therefore, alloys that undergo either AF/FA mode of solidification, for example 316L, can undergo solid state transformation to a fully austenitic structure or a fully ferritic single phase dependent on their composition.

Duplex stainless steels on the other hand, in particular LDX 2101, have higher Cr_{eq} to Ni_{eq} ratios that will result in the final microstructure after solidification to retaining significant amounts of δ-ferrite (Shankar, et al., 2003).

The Cr_{eq} to Ni_{eq} ratios can be determined using the following equations and the solidification mode extrapolated from WRC-92 constitution diagram for the welded stainless steel grades (Siewert & Kotechi, 1992):

$$\mathbf{Ni_{eq}} = \%\mathbf{Ni} + \mathbf{35} \times \%\mathbf{C} + \mathbf{20} \times \%\mathbf{N} + \mathbf{0.25} \times \%\mathbf{Cu} \qquad \textbf{Equation 5}$$

$$\mathbf{Cr_{eq}} = \%\mathbf{Cr} + \%\mathbf{Mo} + \mathbf{0.7} \times \%\mathbf{Nb} \qquad \textbf{Equation 6}$$

In the 1900s significant research was done to investigate the mode of solidification of welds and phase formation during solid state solidification. Numerous diagrams where developed to assist in the proper selection and use of austenitic filler materials and to predict weld metal microstructures and properties. These researchers included Schaeffler and Delong (Figure 6 and Figure 7) who developed diagrams that could be used to find the content of austenite and ferrite in the resulting microstructure by entering the Ni-equivalent over the Cr-equivalent for stainless steel.

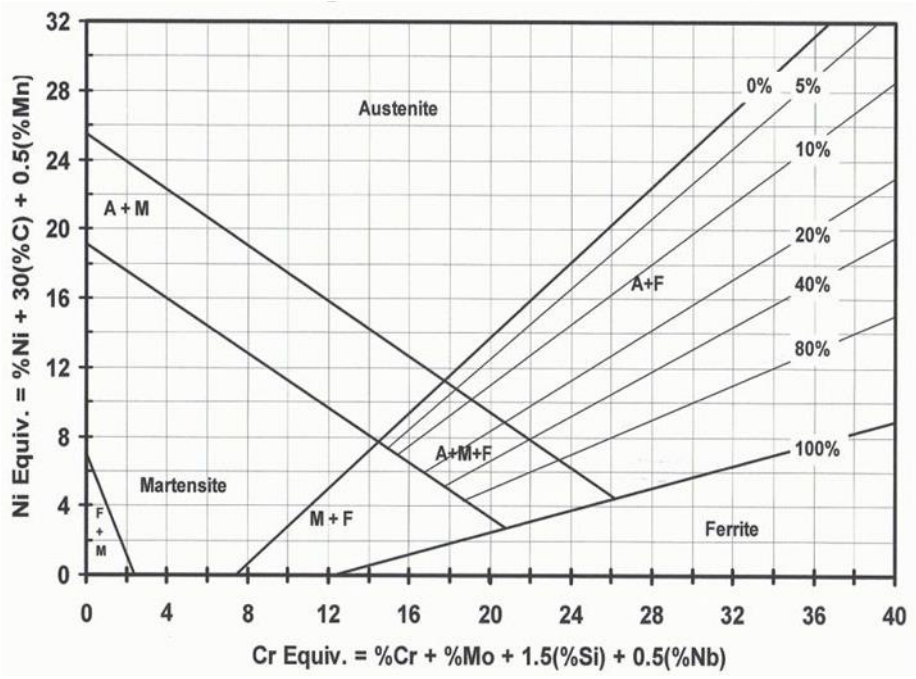


Figure 6: The Schaeffler constitution diagram of 1949 (Schaeffler, 1949).

The Schaeffler diagram was commonly used to predict ferritic-austenitic dissimilar weld metal microstructure. Schaeffler published the final version of his constitution diagram, which is still in use today as seen in Figure 6. This diagram had coefficient changes in the chromium equivalent expression when compared to the Schaeffler diagram of 1948. Additionally, Schaeffler did not include a nitrogen term in the nickel-equivalent equation, although nitrogen is known to be a strong austenite former. This was probably due to the difficulty in determining the nitrogen content in his time.

The Delong diagram is shown in Figure 7 from 1973. DeLong's diagram improved the prediction accuracy for most commonly used austenitic stainless steel weld metals, however it still dealt with a limited composition range.

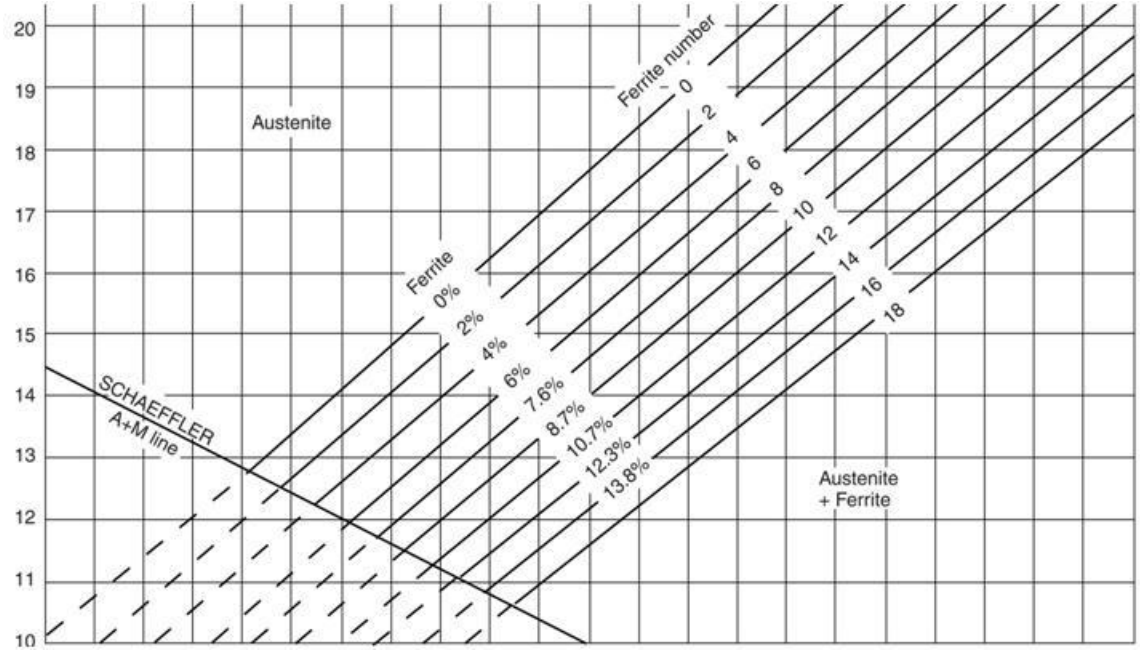


Figure 7: DeLong constitution diagram of 1973, introducing the concept of Ferrite Number (Long & DeLong, 1973).

With the increased use of duplex stainless steels, the DeLong diagram was found no longer adequate. These diagrams were found to incorrectly handle Mn and to overestimate the FN of more highly alloyed stainless steels. Siewert et al (1988) proposed a new ferrite diagram that predicted ferrite up to 100 FN and thus covered the complete range of austenitic and duplex stainless steels. By 1992 the WRC-92 diagram in Figure 8 was published which was a modification of the WRC-1988 diagram. The proposed new diagram included the coefficient 0.25

for copper in the nickel-equivalent formula as seen in Equation 5. This diagram offered a more accurate FN prediction for Cu-containing stainless steels and dissimilar metal joints (Siewert & Kotechi, 1992).

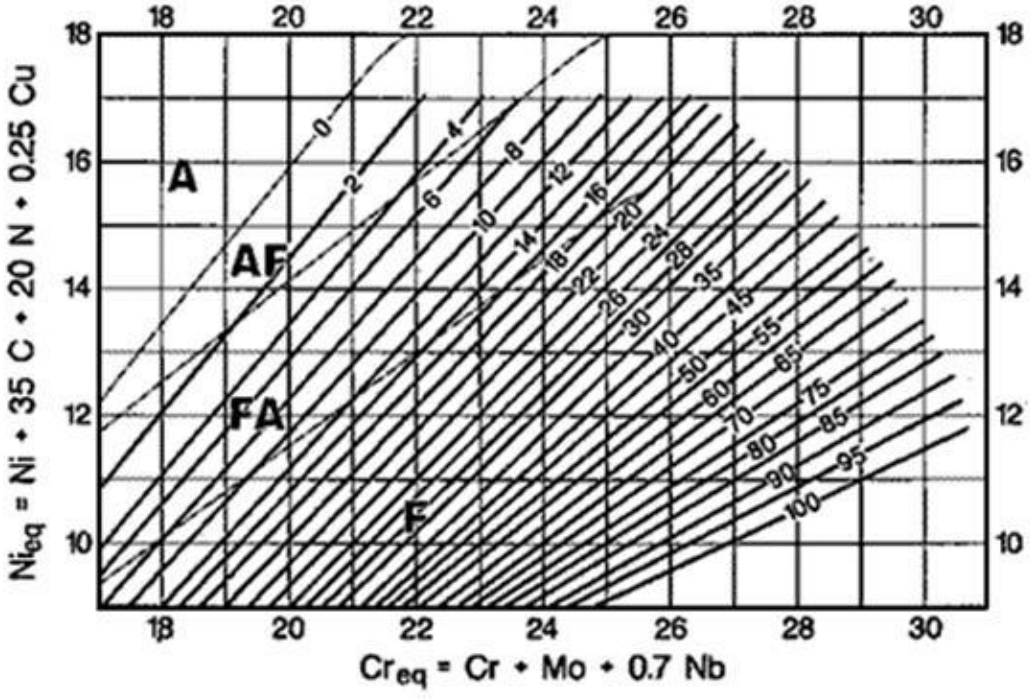


Figure 8: The WRC-92 constitution diagram for weld metal ferrite, including solidification mode boundaries (Siewert & Kotechi, 1992).

The WRC-92 constitution diagram for solidification mode boundaries improves the FN prediction accuracy for stainless steel weld metals that have significant Cu contents. In practice the WRC-92 diagram can be used as a general guide to maintain a desirable solidification mode during welding.

2.8 Weld solidification defects: Hot cracking

During solid state solidification, welds are prone to a phenomenon known as hot cracking. Hot cracking refers to cracking that occurs during welding, casting or hot working at temperatures close to the melting point of the material.

There are typically two types of hot cracks namely:

Type 1 segregation cracks, form at temperatures close to the solidus, where a small volume fraction of liquid still exists. Of the various types of segregation cracks, solidification cracking, which occurs during the last stages of solidification, is the most common and most investigated type of segregation cracking (Kujanpaa, et al., 1986).

Type 2, ductility dip cracks, may occur at lower temperatures in the weldment. These cracks form at newly migrated grain boundaries, and are always free from liquid films (Kujanpaa, et al., 1986).

In 1960 Borland presented the generalised theory with regards to hot cracking. The cracking conditions were known to occur both above the liquation temperature known as supersolidus cracking and in the solid state, called subsolidus cracking. He stated that depending on the distribution of the liquid and solid phases for a binary alloy, solidification involves four stages as shown in Figure 9 (Borland, 1960).

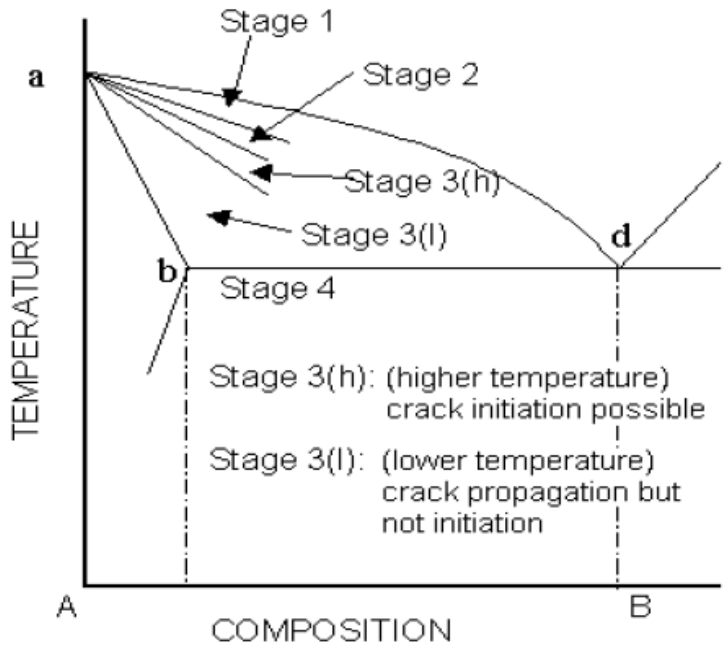


Figure 9: Modified concept of the effect of constitution on cracking susceptibility in binary systems (Borland, 1960).

According to the generalized Borland theory (1960), in stage 1 the solid phase is dispersed with the liquid phase continuous throughout the microstructure and both the phases can accommodate relative movement. In stage 2, both liquid and solid phases are continuous, but the solid dendrites are interlocked and only the liquid is capable of movement. At this stage, the liquid can repair any cracks produced. In stage 3, the free movement of liquid is hindered due the solid crystals approaching full development. The liquid is present in very small quantity. Due to the lack of liquid present at this stage, any stress applied which surpasses the tolerance of the material may undergo cracking. These initiated cracks cannot be filled by the remaining liquid phase due the reduced quantity. This stage is referred to as critical solidification range (CSR). In stage 4, solidification has reached completion and no cracking involving the liquid phase is possible (Shankar, et al., 2003).

A fully austenitic stainless steel weld is more prone to hot cracking than one containing between 3-8% of delta ferrite. Essentially all of the duplex alloys (such as LDX 2101) are less susceptible to hot cracking than the austenitic SS (such as 316L). The presence of delta ferrite decrease grain growth and increases strength properties of steel. However, the ferrite phase presence is not a sufficient condition to prevent hot cracking. The chemical composition can also affect the precipitation of delta ferrite. Composition affects the tendency of stainless steel weld metal towards cracking in two major ways. First, as discussed previously, the primary mode of solidification from the liquid is a function of composition and FA/F mode of solidification has been found to be beneficial in reducing cracking. Solidification mode determines the nature of the solid interfaces present during solidification. The second effect of composition is through segregation, which determines the wetting characteristics and constitutional supercooling in the interdendritic regions. This second effect was essential to Borland's theory as a continuity of liquid at the base of the dendrites, during the last stage of solidification could cause a continuous network of liquid and can provide back-filling. Whereas if wetting is prevented, this will restrict strain within the material due to the bridging and joining of dendrite arms thus reducing the chances of hot cracking.

The presence of nitrogen introduces complexities in the weld metal microstructure and increases the possibility of cracking. Other reasons for hot cracking in stainless steel welds are the presence of low-melting eutectics containing impurities such as S and P and alloy elements such as Ti and Nb.

2.9 Different types of corrosion of stainless steels

2.9.1 General corrosion

Usually, stainless steels do not corrode uniformly compared to ordinary carbon and alloy steels. Uniform corrosion on stainless steel occurs mostly with exposure to strong acid or hot alkaline environments, such as Hydrochloric acid (HCl) and Sulphuric acid (H_2SO_4). HCl and H_2SO_4 at some concentrations are particular aggressive towards stainless steel. In these instances, the passive layer may be attacked uniformly depending on concentration and temperature and the metal loss occurs over the entire surface of the steel.

2.9.2 Localised corrosion

2.9.2.1 Pitting and Crevice Corrosion

Stainless steels like other passive metals are susceptible to localized corrosion in aggressive chloride (Cl^-) containing environments. Localized corrosion in the form of pits and crevices will initiate above a characteristic breakdown potential in a given environment. Pitting corrosion starts when the chromium-rich passive oxide film breaks down in a Cl^- rich environment. Higher Cl^- concentrations and temperatures will most likely increase the breakdown of this passive film. Localized corrosion will tend not to initiate below the breakdown potential, and one design criterion for preventing localized corrosion is to keep the corrosion potential below the breakdown potential. However, localized corrosion pits can propagate at potentials lower than the breakdown potential, but not below a characteristic repassivation potential (Wong, 2009). Therefore, a more conservative design criterion is to keep corrosion potential below the repassivation potential. Pits may also initiate at the austenite-ferrite interfaces in stainless steel weld metal. This makes it crucial that the appropriate filler metal and welding technique is used to ensure localised corrosion does not occur at the weld.

For crevice corrosion to occur, the crevice has to be wide enough to permit entry of moisture, but narrow enough to prevent free circulation. This will result in the depletion of oxygen inside the crevice, but would rather be enriched in a Cl^- rich environment. As a result, the solution inside the crevice becomes acidic and breakdown of the passive film occurs via anodic dissolution. The

mechanism of crevice corrosion is similar to pitting corrosion. To ensure crevice corrosion does not occur, the design temperatures should be at least 15–25°C below the temperatures where pitting corrosion is a risk. Therefore, resistance to crevice corrosion most often goes hand in hand with resistance to pitting corrosion.

The corrosion resistance of a stainless steel can be quantified based on the chemical constituents. The elements which have a significant impact are Cr, Mo, and N. If compared with the lower alloyed grades such as ASS, the duplex stainless steels (DSSs) are characterized by a higher pitting corrosion resistance, which is ranked by the Pitting Resistance Equivalent Number (PREN) (Jargelius-Pettersson, 1998). Pitting resistance equivalent number is a predictive measurement of the corrosion resistance of various types of stainless steel. In general: the higher PREN value, the more corrosion resistant the steel. The Pitting Resistance Equivalent number can be calculated by using the equation:

PREN=%Cr+3.3 %Mo+16%N **Equation 7**

An exception is stainless steels with Mo content equal to or above 1.5%; these may have a PREN value of 30 or more (Gunn, 1997). In these cases the PREN value takes into account tungsten (W) in the alloy and is defined with Equation 8:

PREN=%Cr+3.3 (%Mo+0.5%W) +16%N **Equation 8**

According to Szklarska-Smialowska, in 1986 there are different ways to estimate and compare the different alloy's susceptibility to pitting, namely by:

- Stainless grades PREN
- determining the characteristics of the metal's or alloy's pitting potentials
- determining critical temperature at which pitting is instigated
- measuring the number of pits per unit area, weight loss, and if possible, the size and depth of pits formed in the standard solution and
- determining the lowest concentration of aggressive ions causing the pitting (Szklarska-Smialowska, 1968).

The formation of pits in stainless steels in aqueous environments is suggested to be in accordance with a sequence. Involving; initially chloride adsorption and complexing with the outer layers the passive film, a process which initiates local mechanical film rupture. This is followed by

competitive adsorption of passivating species $[MO.OH]_{ads}$ and $[MOMOH]_{ads}$ and non-passivating species $(MOMCl)_{ads}$ and $(MOH)_{ads}$ leading to either film repair or metal dissolution (Dawson & Ferreira, 1986).

2.9.3 Intergranular corrosion

Austenitic stainless steels are prone to sensitization when subjected to higher temperatures (673 K to 1173 K) during the manufacturing process, particularly during welding. During sensitization, chromium in the matrix precipitates out as carbides and intermetallic compounds (sigma, chi and Laves phases) decreasing the corrosion resistance and mechanical properties, significantly in the HAZ of a weld (Unnikrishnana, et al., 2014).

The effects of sensitization are a loss in corrosion resistance due to chromium depletion and additionally a loss of fracture toughness due to precipitation of complex carbides within and along the HAZ grain boundaries (Korinko & Malene, 2001). By simply reducing the amount of carbon available for the chemical reaction to occur with chromium, the “L” grades of stainless steel result in enhanced weld HAZ resistance to sensitization. Therefore, lower carbon 316L ASS is a suitable alternative to 316 ASS due to the improve resistance to weld decay in 316L ASS. Sensitization refers to the precipitation of carbides at grain boundaries in a stainless steel or alloy, causing the alloy to be susceptible to intergranular corrosion or intergranular stress corrosion cracking.

2.9.3.1 Weld decay

Weld decay is a form of intergranular corrosion, usually of stainless steels or certain Ni-base alloys that occurs as the result of sensitization (as mentioned in 4.10.3) in the HAZ during the welding operation. Figure 10 shows an illustration (will be described in section 4.10.3.) of the weld decay zone in stainless steel weldments.

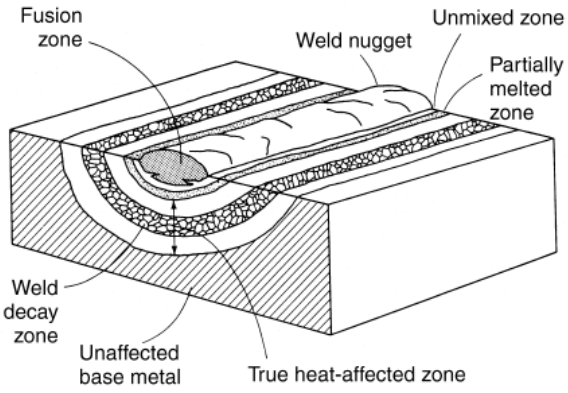


Figure 10: Intergranular corrosion (weld decay) of stainless steel weldments (ASM International, 2006).

Weld decay is due to the chromium carbide formation along grain boundaries. This results in depletion of Cr in the region adjacent to the grain boundary. The depletion of Cr essentially causes small sites of localized galvanic cells. Cr is crucial in maintaining the passivation layer as once it is depleted the metal becomes sensitive to corrosion hence the concept of sensitization causing intergranular corrosion (ASM International, 2006).

Sensitsation can be prevented by reducing the chances of weld decay by adopting the following options. The use of low-carbon grade of stainless steel (e.g. 316L) to avoid carbide formation can reduce weld decay (Fandem.Q.A, 2017). Or to redissolve the Cr at grain boundaries, and hinder chromium carbide formation by carrying out a postweld high-temperature anneal and quench.

2.9.3.2 Stress corrosion cracking

Stress corrosion cracking is the cracking induced when a susceptible material experiences both tensile stress and a corrosive environment. The alloy content of stainless steels, particularly nickel, determines the sensitivity of the metal to SCC. The most common grades of stainless steel, 304L and 316L, contain nickel in the range 8-10% and are the most susceptible to SCC (Parrott & Pitts, 2011). The LDX 2101 has a superior SCC resistance than the standard austenitic grades (Zanotto & Zucchi, 2014). Corrosive environments that are chloride containing are the most frequent causes for stress corrosion cracks. These cracks are classified as Chloride Stress

Corrosion Cracking (CSCC) and remain the most life limiting failure for ASSs. The CSCC can occur in hot acid chloride solutions, sodium chloride solutions, and they cause SCC of the 300 series stainless steels (Parrott & Pitts, 2011). The combination of residual stresses from welding, the cold work from fabrication, and the cyclic stress from operating conditions are sources of tensile stress that when increased above a certain threshold stress, will cause the metal to be susceptible to SCC.

2.9.4 Galvanic corrosion

Galvanic corrosion can be defined simply as being the effect resulting from contact between two different metals or alloys in a conducting corrosive environment. When two different metals are electrically coupled (as are a weld and base metal) and exposed to the same environment, galvanic interactions will occur. The more active metal (or less-noble metal, i.e. the one with the lower corrosion potential in that environment) will undergo accelerated attack and the more noble metal will be protected. This galvanic protection is a form of cathodic protection and is the mechanism explaining how a steel substrate is protected from corrosion by the Ru coating in a galvanized structure.

One key aspect in galvanic coupling is the area ratio of the two metals. It can be shown that i_a, the anodic current density or corrosion rate of the anode or less noble metal, depends upon the ratio of the areas of the cathode and anode, A_c and A_a, and the current density at the cathode, i_c, according to:

$$\mathbf{i_a = \frac{A_c}{A_a} i_c} \qquad \textbf{Equation 9}$$

The galvanic potential will also depend upon the area ratios. If one area is significantly larger than the other, then the galvanic potential of the couple is pinned at the uncoupled corrosion potential of the larger metal. For a welded stainless steel structure, the area of the weld metal is much less than the area of the substrate being welded, which means that the potential of the weld will be set by the corrosion potential of the stainless steel in the particular environment. If the weld metal is less noble than the stainless steel, the galvanic coupling will result in an increase in the potential of the weld. This can result in aggressive attack of the weld if the stainless steel corrosion potential

is above the breakdown potential of the weld, or if the less noble weld metal does not passivate and dissolves actively. However, if the weld metal is noble relative to the stainless steel, then the galvanic coupling will result in cathodic protection of the weld metal by the stainless steel (Lippold & Frankel, 2009).

2.10 Corrosion of stainless steel alloyed with Ru

Corrosion has cost the stainless steel industry significant amounts of money resulting in mechanical failure and increased maintenance costs. Typically, stainless steels will not corrode in normal atmospheric and pH environments as demonstrated by our household cookware, sinks and cutlery etc. However, in more aggressive conditions the independent stainless steel grade susceptibility to corrosion will be dependent on its constituent elemental composition.

The corrosion resistance of austenitic and duplex stainless steel is important to understand as these are the most widely used steels. In particular, the corrosion resistance of DSS's is important to understand as these are developing rapidly today and are gaining an increased usage across numerous industries. DSS's have microstructures approximately equal to austenitic stainless steels and have become competitors on the same field. The understanding of these materials corrosion capabilities becomes crucial during the material selection processes for joining applications such as welding. Although duplex stainless steels and some ASSs have similar alloying elements, duplexes have higher yield strength and greater stress corrosion cracking resistance to chloride containing environments than ASSS. With the addition of platinum group metals to stainless steels, researchers have shown improved corrosion resistance of host metals.

2.10.1 Effect of Ru addition to corrosion of stainless steel

Potgieter, Ellis, and Van Bennekom (1995), showed that stainless steels alloyed with minor Ru additions passivate spontaneously due to the formation of a stable passive surface layer with a significant increase in corrosion resistance. This shifts the corrosion potential of these alloys towards more noble (more positive) values (Lippold & Frankel, 2009). Other researchers have further validated that during active dissolution of ASS weld metal; Ru increases the corrosion potential and lowers the critical density as well as the passivation current density. The mechanism of corrosion also depends on the medium of exposure. When exposed to a hydrogen ion (H^+) environment during active corrosion the Ru modified stainless steel weld metal, it would increase

the resistance of the stainless steel to the anodic dissolution while decreasing the overpotential for hydrogen (Chernova, et al., 1978). Additionally when exposed to a chloride environment the Ru addition decreased the cathodic Tafel constant and had a retarding influence on the cathodic part of the corrosion reaction (Potgieter, et al., 2014).

The polarisation characteristics of a typical stainless steel, show a large passive region as shown in Figure 11. During active dissolution, Ru increases the corrosion potential and lowers the critical as well as the passivation current density (Van der Merwe & Tharandt, 2015). In essence during active corrosion, Ru additions increase the resistance of stainless steel to anodic dissolution and lower the hydrogen overpotential. This implies that Ru inhibits the corrosion of the alloy by a combination of these two mechanisms (Potgieter, Ellis, and van Bennekom, 1995).

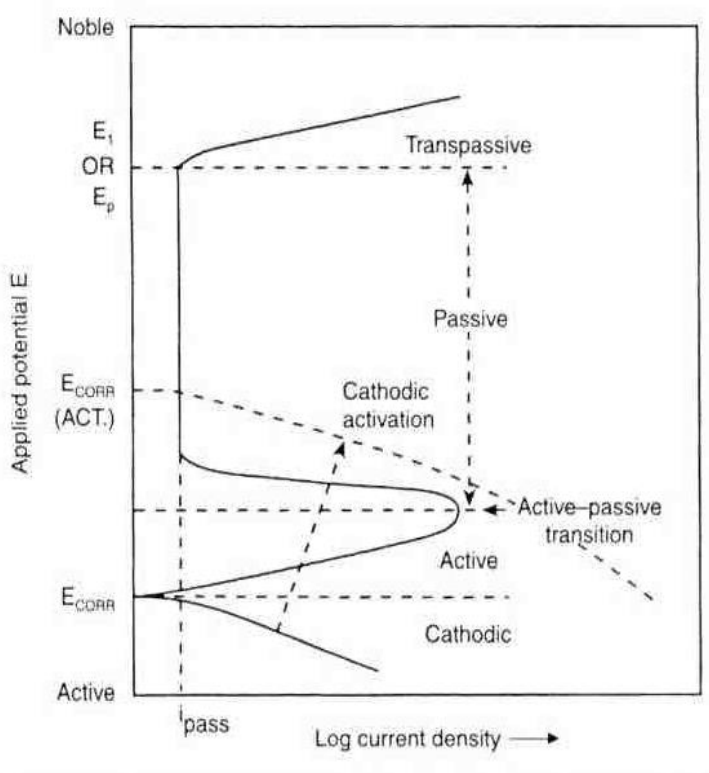


Figure 11: Typical polarization curve of Fe-Cr alloy showing effect of cathodic modification (Wolff, 1999).

The corrosion of the welded metal can be controlled by galvanic corrosion if the 316L ASS is welded with a filler metal that is a different composition to parent metal. However, in this study,

the modes of corrosion of passive metals such as stainless steels are usually localized in nature, such as pitting corrosion. Therefore, to understand the approach used in this project, it is necessary to understand some fundamental aspects of localized corrosion.

Furthermore, the fact that Ru is the cheapest of the PGMs has drawn significant interest in its capability to induce the spontaneous passivation processes of steels containing small amounts of Ru as alloying element (Potgieter, et al., 1995) (Varga, et al., 1997).

2.11 Mechanism of cathodic modification

Cathodic modification is an electrochemical mechanism of improving the corrosion resistance of alloys, particularly of stainless steels. This modification is expected to be possible by the addition of an element exhibiting high exchange current density for the reduction of the hydrogen over potential to raise the corrosion potential (E_{corr}) of the matrix.

There are four possible ways in which corrosion-resistant alloys can be produced and the resistance of alloys against electrochemical attack increased, according to Tomashov in 1986 (Tomashov, 1896):

I. an increase in the degree of thermodynamic stability,
II. retardation of the kinetics of the cathodic processes,
III. retardation of the kinetics of the anodic processes, and
IV. the production of stable passivating oxide layers.

The widespread approach to effectively improving corrosion properties of stainless steels has been through the addition of major and / or minor alloying elements. In particular, the use of noble materials as minor additions to base materials has shown significant improvement corrosion resistance.

Researchers at the University of the Witwatersrand have confirmed this in the early 2000's. That the corrosion resistance of virtually all stainless steels can be increased by alloying them with minor additions of platinum group metals (PGMs) (Sherif, et al., 2009). The research validated that this can be done by retarding the anodic dissolution of steels to which they are added and also increase the effectiveness of cathodic processes owing to the reduced overvoltage of

hydrogen. Therefore, the increased thermodynamic stability of the alloy, mechanism (i), and the retardation of the anodic process, (iii), can widely be achieved through minor additions of noble elements such as the PGM's. Platinum group metal (PGM), Ni or Mo additions facilitate cathodic depolarisation (ii) by providing sites of low hydrogen overvoltage, which shifts the alloy potentials in the positive direction where oxide film passivation (iv) is possible as shown in Figure 12 and Figure 13. Therefore the mechanisms (i) and (iii) and (iv) are also achievable even through additions of less noble elements such as Ni, Mn, and Cr (Potgieter, 1996).

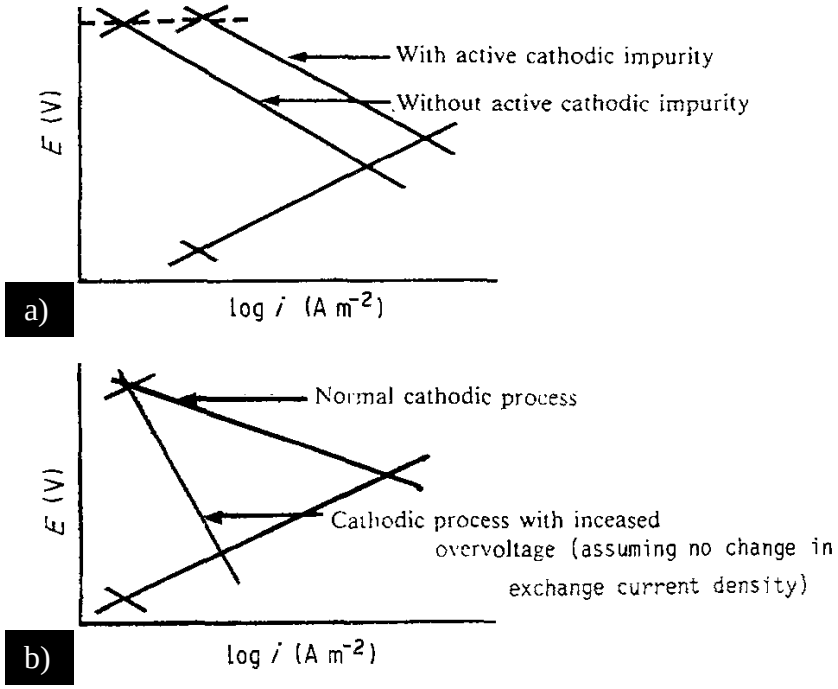


Figure 12: (a) Graphical representation of the effect of addition of cathodic impurity and (b) graphical representation of ways in which cathodic reactions can be retarded by increasing over potential (Potgieter, et al., 1990).

The effect of the addition of a cathodic impurity is shown in Figure 12(a) and then the influence increased overportential has on these cathodic process is shown in Figure 12(b). Figure 13 shows the impact of cathodic modification.

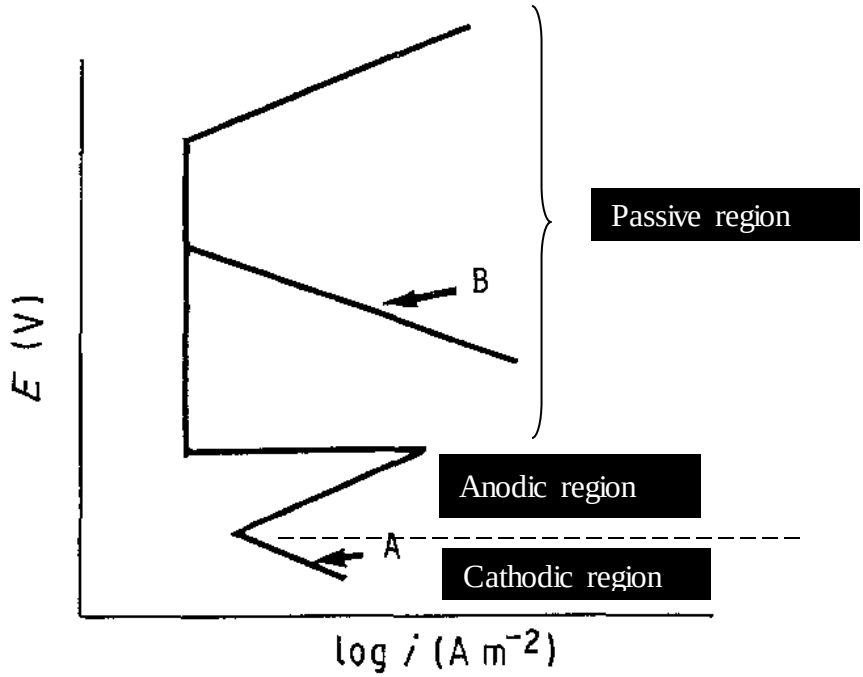


Figure 13: Schematic representation of effect of cathodic modification (Potgieter, et al., 1990).

The impact cathodic modification has on a typical polarisation curve path “A” is shown in Figure 13 above image and the cathodically modified alloy is represented by line “B” which is in the passive region of the polarisation curve, therefore indicating the ability of the alloy to undergo spontaneous passivation.

2.12 Effect of NaCl solution on corrosion of stainless steels

When chlorides are present in the medium, the decrease in the concentration of NaCl is manifested by a shift of corrosion potential towards more positive values. Increasing the NaCl concentration will considerably increase the risk of pitting corrosion, which is a significant problem for stainless steels. In order to reduce the corrosion rate, it is necessary to reinforce the passive layer by increasing the chromium, nickel or molybdenum content. In this study this reinforcement of the passivation layer in expected to be possible by the introduction of Ru.

The susceptibility of a stainless steel to pitting corrosion increases and decreases is essentially understood as kinetic competition between the formation of non-passivating species $(MOMOHCl)_{ads}$, $(MOMCl)_{ads}$ and passivating species $[MOOH]_{ads}$, $[MOMOH]_{ads}$. At the potential in the passive region, the observed constant current density is due to the conversion of $Fe(OH)_2$ to more stable FeOOH according to this reaction:

$$\mathbf{Fe(OH)_2 \leftrightarrow FeOOH + H^+ + e^-} \qquad \textbf{Equation 10}$$

At high potentials the chloride ions are able to inhibit film formation by complexing with the adsorbed species and increasing the rate of dissolution and formation of non-passivating species. The resultant reactions at high potentials would therefore be (Asaduzzanman, et al., 2011):

$$\mathbf{[MOMOH]_{ads} + Cl^- \leftrightarrow [MOMCl]_{ads} + OH^-} \qquad \textbf{Equation 11}$$

$$\mathbf{(MOMCl)_{ads} + H_2O \leftrightarrow [(MOH)_{ads} + MOH^+ + Cl^-} \qquad \textbf{Equation 12}$$

Or

$$\mathbf{[MOM(OH)_2]_{ads} + Cl^- \leftrightarrow (MOMOHCl)_{ads} + OH^-} \qquad \textbf{Equation 13}$$

$$\mathbf{(MOMOHCl)_{ads} + H^+ \leftrightarrow (MOH)_{ads} + MOH^+ + Cl^-} \qquad \textbf{Equation 14}$$

For Austenitic and Duplex stainless steels these reactions can be expressed as follows, for the electrochemical reaction in NaCl:

$$\mathbf{Fe(OH)_2 + Cl^- \leftrightarrow FeOCl + H_2O + e} \qquad \textbf{Equation 15}$$

$$\mathbf{Fe(OH)_2 + 6Cl^- \leftrightarrow FeCl_6^{3-} + 2OH + e^-} \qquad \textbf{Equation 16}$$

The initiation of the film rupture process is associated with chloride ion adsorption on the outer part of the film, which would therefore thin the film locally at the sites of weakness (inclusions, grain boundaries, flaws, etc.) (Dawson & Ferreira, 1986). According to Equation 16 pit initiation is dependent on the accumulation of six chloride ions for generation of each Fe^{2+} ion. Overall the susceptibility of pitting corrosion of austenitic stainless steel increases with the increase of chloride ion concentration in acidic chloride media. Moreover the pitting potential (Epit) and pitting induction time decreases with the increase of chloride ion concentration (Asaduzzanman, et al., 2011).

2.13 Corrosion rate determination

The corrosion rate can be determined from mass loss of the specimen when exposed to an aqueous environment. However this technique is time consuming and has limited sensitivity. Corrosion rates are determined by applying a current to produce a polarization curve. The variation of potential as a function of current enables the study of the effect of concentration and activation processes. Polarisation measurements can be used to determine the rate of the reactions involved in the corrosion process, which gives the corrosion rate (Adenike, 2014). The corrosion rate can therefore be determined electrochemically from measured polarization curves using an understanding of polarization behavior, by:

1. Tafel extrapolation,
2. Non linear least squares fit to ideal equation, which is similar in form to the Butler-Volmer equation, and
3. Linear polarization resistance.

1. **Tafel extrapolation**: With electrochemical kinetics, it is then possible to present mixed potential theory, which predicts corrosion potential and the rate on the basis of the kinetics and thermodynamics of all of the reactions occurring on an electrode surface. By extrapolating from the Tafel plot corrosion rates can be measured from potentiodynamic corrosion tests (Frankel, 2016).

The linear regions of the log(i) vs E plot show the tafel plots as shown in the Evans diagram in Figure 14.

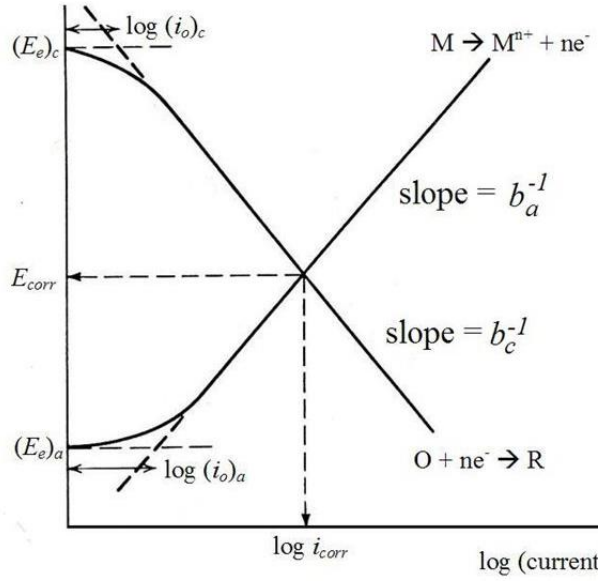


Figure 14: Evans Diagram (Frankel, 2016).

2. **Butler-Volmer:** For a reaction in which the rate is limited by activation overvoltage, the relationship between the rate of reaction, which can be expressed by a current density i, and the driving force for the reaction, or potential E, is given by the Butler-Volmer equation (Bockris & Reddy, 1973) (Gellings & Bouwmeester, 1997).

$$\mathbf{i = i_0 \exp\left[\frac{\alpha n F(E-E_{corr})}{RT}\right] - i_0 \exp\left[\frac{-(1-\alpha) n F(E-E_{corr})}{RT}\right]} \qquad \textbf{Equation 17}$$

Where

i- The electrode current density (A/cm^2)

i_o- the exchange current density (A/cm^2)

F- Faraday's constant [96,485 C mol^{-1} or J mol^{-1} V^{-1}]

R- Universal gas constant [8.314 J/mol.K]

T- Temperature [K]

n- Number of electrons transferred in reaction

α- reduction charge transfer coefficient

E_{corr} - the corrosion potential (V), and

E- The cell potential (V).

Thereafter for high anodic or cathodic over potentials, the Butler-Volmer equation can be reduced to the following linear expressions, for anodic:

$E - Ecorr = \log icorr + \beta_a \log|i|$ **Equation 18**

and for the cathode process:

$E - Ecorr = \log icorr - \beta_c \log|i|$ **Equation 19**

Where the β_a and β_c are the Tafel constants (V/dec) for the anodic and cathodic respectively (Metrohm Autolab B.V, 2011).

The estimated value of the polarization resistance can be calculated from the intercept and the Tafel slopes, according to following equation:

$$\mathbf{R_p} = \frac{\mathbf{1}}{\mathbf{2.303}(\frac{\mathbf{1}}{\beta_a}+\frac{\mathbf{1}}{\beta_c})\mathbf{i_{corr}}}$$ **Equation 20**

Where, R_p is the polarisation resistance (Ω) (Metrohm Autolab B.V, 2011).

3. **Linear polarization resistance**: Linear polarization is a non-destructive method designed for measuring polarization resistance. By using polarization resistance, the corrosion rates from the measured polarisation curves for a specific sample under electrochemical analysis can be determined. By using the modified version of Faraday's Law the corrosion rate can be determined very accurately based on Equation 21. The linear polarisation method has many advantages in calculating instantaneous corrosion rates for many metals in various conditions. Linear polarisation is based on the theoretical and practical demonstration that at potentials very close to E_{corr} ±10mV, the slope of the potential/applied current curve is approximately linear. The corrosion current (i_{corr}), generated by the flow of electrons from anodic to cathodic sites, can be used to compute the corrosion rate (Frankel, 2016).

$$\mathbf{C} = \frac{\mathbf{i_{CORR} \times E}}{\mathbf{A \times D}} \times \mathbf{128.67}$$ **Equation 21**

Where,

C – Corrosion rate in mils per year (m/y), and

i_{corr} - corrosion current density (A/cm^2).

Where the following are required inputs for specific material being analysed:

A-area of corroded electrode (cm^2),

D - Density of corroded metal (g/cm^3).

In general there are four major factors that will determine the corrosion rate in an electrochemical reaction occurring at the electrode surface:

1) mass transfer of reactants or products to/from the electrode surface by diffusion, migration, convection and agitation,

2) kinetics of electron transfer;

3) preceding and ensuing reactions, and

4) kinetics of adsorption/desorption.

The rate determining step is therefore determined by the slowest process.

Shreir further defined rate determining factors as follows (Shreir, 1963):

1) Transportation: The movement of charged or neutral species that allows the flow of electricity through an electrolyte solution in an electrochemical cell is referred to as a mass transport process.

When an electrochemical cell undergoes transportation via diffusion/ migration/ convection/ agitation; the electrode kinetic, diffusion and convection steps need to be solved, to be able to predict the current flowing and therefore the corrosion rates.

2) Activation energy: The rate of an electrochemical reaction is controlled by the magnitude of one or more energy barriers that every electrochemical reaction involved must overcome to be transformed. When the activation energy or anodic process controls the rate, the process is said to be under activation control. The energy required to be overcome by the material is known as the activation Gibbs free energy ΔG^*. Figure 15 shows the schematic distribution of the free energy profile.

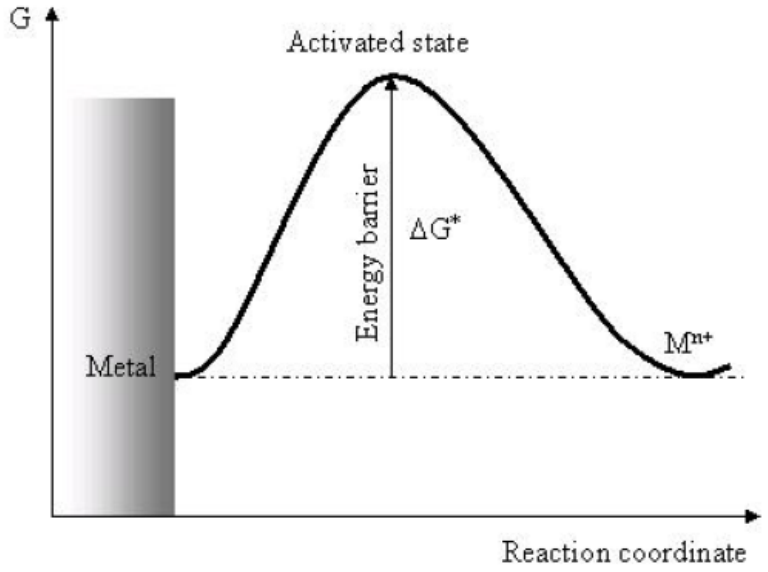


Figure 15: Schematic distribution of the free energy (Amri, 2009).

In electrochemical or corrosion reactions this Gibbs free energy is defined as an excess of energy that must be acquired by the metallic element to transform into a soluble metallic ion for example Mn^{+}.

3) Resistance overportential: when the internal resistance of analysed material vs the solutions interface is rate determining, the process is said to be resistance controlled.

2.14 Cost of 316L ASS compared to LDX 2101

There are numerous factors that affect commodity prices. Typically economists account for high commodity prices as a result of scarcity of the particular commodity. Business analysts say that the supply-demand balance determines price. For the stainless steel industry there are particular elements that influence the pricing of the stainless steel grade. In particular, these commodities of interest are chromium, copper, manganese, molybdenum, and nickel which essentially influence the stainless steel price (Papp, et al., 2007). For 316L which is a low carbon austenitic stainless steel and LDX 2101 a lean DSS they contain Cr, Ni and Mo, these alloying elements are crucial in determining these two SS prices. Of all the three critical alloying elements, the pricing of stainless steel is largely dependent on the market prices of worldwide nickel. Two-thirds of all

nickel mined and produced in the world will make its way into stainless steel. The health of the worldwide nickel market is also directly dependent on stainless steel production.

The factors that influence the Ni prices in the world are:

- scarcity,
- supply/demand balance,
- stocks/rate of use,
- actual or anticipated supply disruption,
- earnings, market performance, expectations, and
- investment level.

These key factors have been tried and tested in the South African markets, due to South Africa's relatively small steel market the increase in prices of steel would disadvantage the local market. SA prices had no discernable impact on the world steel market because markets are controlled by the global commodities index. The cost of raw material inputs and the level of demand measured against the capacity to make the steel (the capacity utilisation) remain the two main reasons influencing the price escalation. According to the London metal exchange (LME), over a period of time the Ni price has increased with decreasing stock levels, as in Figure 16. A closer focus to the periods of Dec'2016 and Dec'2017 in Figure 17 shows a similar correlation with an increase in the Ni price.



Figure 16: Nickel stocks vs price from 1990 to 2008 (Papp, et al., 2007).

The rising price of alloying elements, such as nickel, have dramatically increased the costs for 316L and other high nickel bearing stainless steels, which are common materials of construction for numerous products utilized in corrosive environments.

Additionally these factors have influenced our Ni prices these include:

- Globalization
- Government
- Geopolitics
- Growth
- Exchange rate (value of the dollar)
- Cost of production (energy, taxes, labour, etc)

A closer focus on the periods of Dec'2016 to Dec'2017 in Figure 17 shows a similar correlation with an increase in the Ni price.

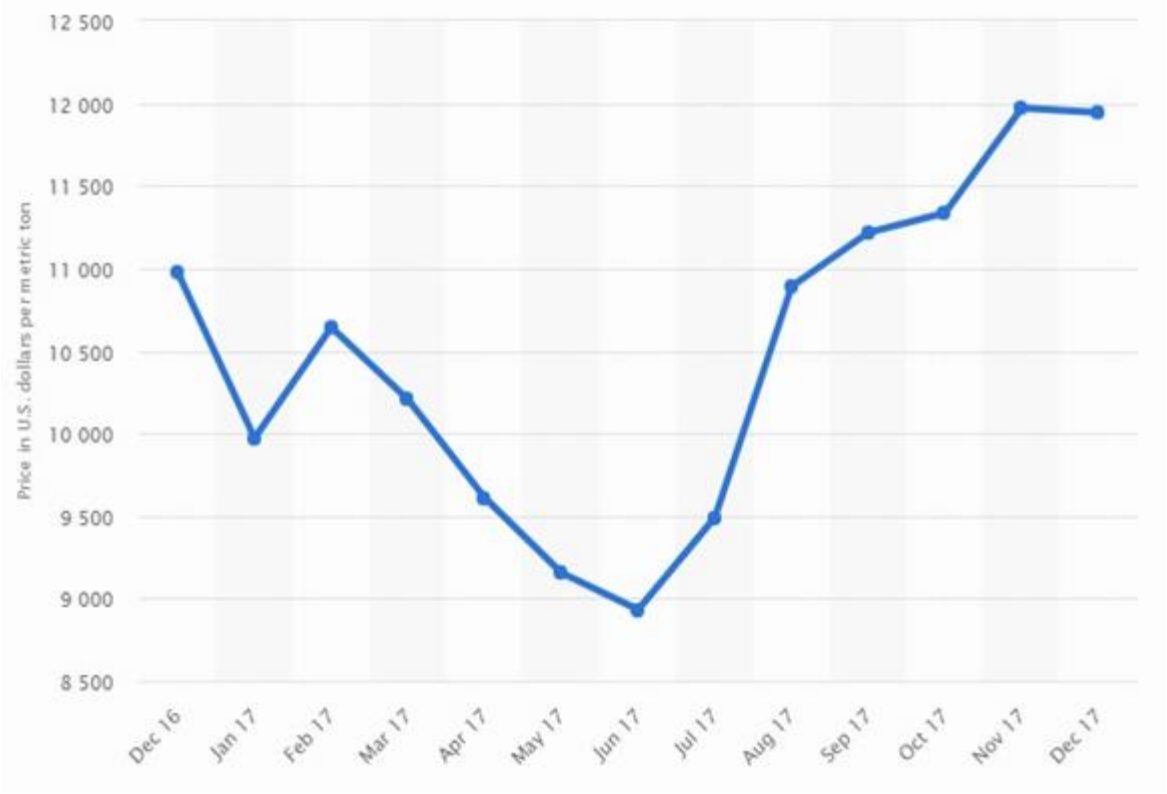


Figure 17: Price of nickel at the London Metal Exchange from Dec'2016 to Dec'2017 (in U.S. dollars per metric ton) (Statisca, 2017).

Overall when considering the cost and price benefits of one steel to another the primary alloying elements cost, weight, strength, malleability and corrosion resistance needs to be considered. The minimum yield strength of LDX 2101 is over twice that of 316L stainless steels. The increased strength of LDX 2101 in comparison to 316L will allow for a lighter wall thickness as the material can be used in thinner gauges to achieve the same result. This will result in less material being used for an application as well as less weld wire costs and even more importantly less transportation costs. Duplex grades offer a potentially cheaper alternative, as most of the DSS only half the Ni of an ASS with similar corrosion resistance. The new development of LDX 2101 from Outokumpu, which was designed to have a lean chemistry, substitutes nearly all of the Ni with Mn thus giving, preferred pricing and corrosive resistance. The conversion costs of 316L vs LDX 2101 must still be taken into consideration in the final cost analysis. Although LDX 2101's welding costs per kg seem higher than other ASSs, which is to be expected given that less material is used overall. However, the process of welding LDX 2101 is also significantly faster. The LDX 2101 DSS requires similar welding techniques at conventional stainless steels. The only significant difference is how joints need to be configured and in the type and quantity of fillers required. Seeing that LDX 2101 welds faster this also means that the total assembly time is faster, this yields labour savings. Overall LDX 2101 is a stronger and more corrosion resistant alloy than 316L for about the same cost.

2.15 Background on Ruthenium

Ruthenium together with rhodium, palladium, osmium, iridium, and platinum form a group of six elements referred to as the platinum group metals. These six platinum group metals are chemically very similar. Ruthenium, which is derived from the Latin for 'Russia', is said to have been discovered by Russian, Karl Klaus in 1844 (Pitchkov, 1996). Ruthenium is hard, brittle and almost unworkable in the metallic state, with poor oxidation resistance, but is valuable as additions to other metals, usually other PGM alloys, and as a catalyst.

In South Africa, it is mined and obtained as a by-product of Ni, Cu and other PGMs in South Africa. With 58% of worlds PGM production taking place in South Africa and Russia, accounts for a further 26%, most of this as a co-product of nickel mining. Nearly all of the rest comes from Zimbabwe, Canada, North and South America, and the USA.

In Table V the mechanical and physical properties of Ru are depicted. Ru depicts superior physical and mechanical properties as a rare earth metal.

Table V: Physical and Mechanical Properties of Ruthenium (AZoM, 2013).

Element	Density (g/cm^3)	Melting point (°C)	Vickers hardness no.*	Electrical resistivity (microhm.cm at 0°C)	Thermal conductivity (Watts/(meter.°C)	Tensile strength (kg/mm^2)
Ru	12.45	2310	240	6.80	105	165

*Annealed conditions.

Ru has a high melting point of 2310°C and a boiling point of 4080°C and is now being considered for use in alloys that need to withstand intense heat. Due the superior thermal resistance and corrosion resistance of Ru, it has been considered for alloying and welding application in an attempt to improve typically weak parent stainless steel metals. When compare to the other PGMs Ru stands out due to its affordability and availability. Figure 18 shows the Ru prices over the past 13 years.

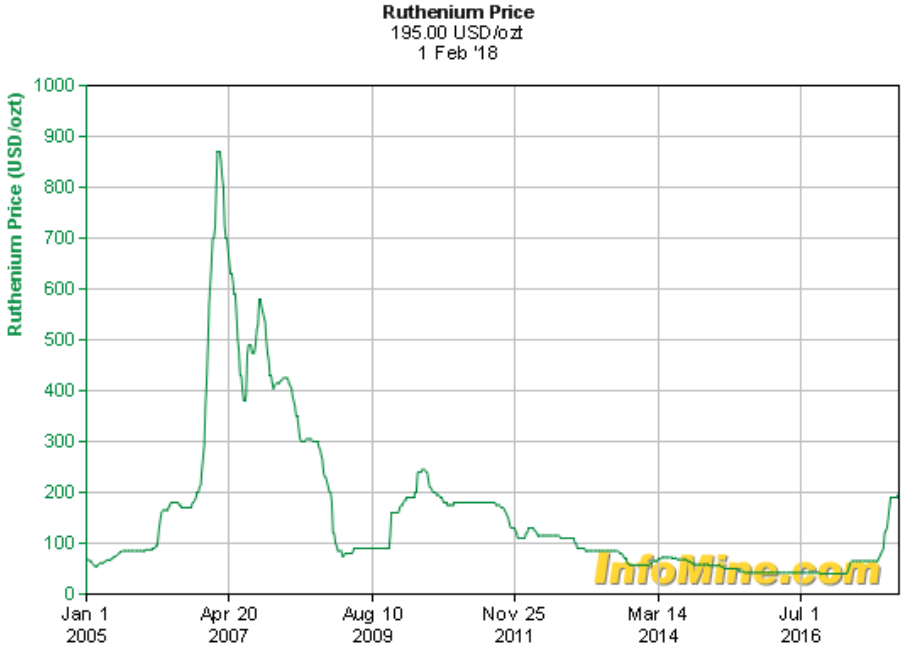


Figure 18: Ruthenium Price over the last 13 years (InfoMine Inc, 2017).

In 2007 Ru saw a significant price boom, where three years prior it could be purchased for as little as $35/oz; in 2007 it rose to peck prices of $800/oz as shown in Figure 18. Peter Duncan, head of market research from a UK based company Johnson Matthey stated that the hard disk industry used to use Ru as a support layer coating on hard disks. The hard disk industry underwent a step change in terms of technology at the end of 2006. This resulted in a considerable increase in the amount of Ru deposited on each disk. While the net demand for Ru in this application was not in itself enough to push the market into deficit, the process by which the metal was deposited required significant pipelines to deposit the materials on the disks. This meant that the entire hard disk industry was suddenly looking to fund enormous pipeline builds, and the only way to do that was to buy the metal. This created a massive surge in demand at the end of 2006 and into 2007 (Duru, 2011).

Impala Platinum (one of the world's foremost South African producers of platinum and other PGM's) marketing executive Derek Engelbrecht in 2007 reported that Ru was additionally being considered in alloys for aerospace where the heat generated was unable to be withstood by unalloyed materials. The price of Ru in 2017 was 40.00 USD/oz; Ru is therefore categorized as the least expensive of the PGM's whereas Pt is the most expensive.

2.16 Effect of Ru addition to stainless steel

Schutz in 2003 documented the positive effects of PGM's addition on the corrosion properties of titanium alloys (Schutz, 2003). The titanium alloys underwent spontaneous passivation by cathodic modification (Mwamba, et al., 2014), it can be assumed that the same mechanism, cathodic modification, should also function in any alloy that is protected by a corrosion resistant oxide film. This is the case for stainless steels, which typically rely on a chromium oxide film to protect the alloy. The addition of PGM's to stainless steels has shown significant corrosion resistance improvement with the open circuit potential breakdown potential and repassivation potential all increasing with Ru addition. In the past 10 years researchers from Ohio University have looked at the addition of Ru in the Ni–Cu weld consumable for conventional stainless steel joining. These studies by Ohio University have also shown improved corrosion behavior of the weld metal (Liang, et al., 2010) . The understanding on what happens to the microstructure of the stainless steels and with additions of Ru has many areas yet to be investigated.

Chapter 3

3 Methodology

3.1 Introduction

In this study the fundamental effect of Ru additions to the weld metal of 316L ASS and LDX 2101 was investigated. In particular this study evaluates the effect of Ru additions on corrosion and mechanical properties of these welded steels. To determine the outcome a microstructural analysis was done to ascertain the effect of ruthenium additions. Additionally, hardness tests were done to determine effect of Ru additions on hardness of the material and to ensure that properties such as hardness did not deteriorate. The impact of Ru addition on the corrosion resistance of the steels in chloride containing environments needed to be understood. The effect of Ru addition to the morphology of the steel needed to be observed over a period of time after exposure to corrosive environment. This was done to assess if there was an improvement from Ru addition (if any) on surface condition of the stainless steel in corrosion environments. This result could aid in future commercialization of the welding with Ru additions for stainless steels in harsh environmental applications where stainless steels would usually not be considered.

3.2 Stage 1: Weld fabrication

3.2.1 Gas Tungsten Arc button welds

A compact vacuum arc melting system furnace from Mintek in Figure 19(a) was used to fabricate the GTAW button welds. These button welds would represent the heat affected zone (HAZ).

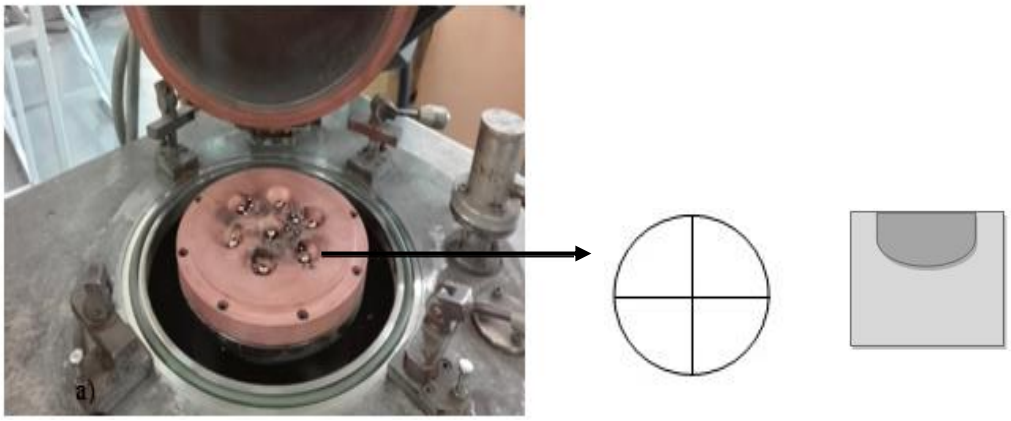


Figure 19: (a) The copper hearth for compact vacuum arc melting system, (b) schematic of spherical button weld and (c) cross sectional view of mounted sample.

Buttons with a total weight of 10 g each were made by gas tungsten arc (GTA) melting 316L with compacted powder Ru feed material using the copper hearth button-arc furnace at Mintek (South Africa). This process was done under a compact vacuum atmosphere using titanium as an oxygen-getter, and the samples were cooled in the furnace, on a water-cooled copper hearth as shown in Figure 19(a). This GTA melting technique was similarly used for the fabrication of the LDX 2101 stainless steel button welds. The following compositions were also button welded: 0.1 wt% Ru, 0.5 wt% Ru, 1 wt% Ru, and 2 wt% Ru. Since the Ru was in the form of a powder which can be easily be blown away by the arc, the powder was compacted and compressed and placed beneath a piece of 316L or LDX 2101 parent material. The resultant sample from the furnace was an oval like ball as shown in schematic Figure 19(b).Thereafter a variety of tests were performed on the GTAW button-melted samples.

3.3 Stage 2: Material preparation

3.3.1 Test samples preparation: Metallography

The oval-like GTAW button samples were cut into four quarters as shown in Figure 19(b) ready for testing. A quarter section from each alloyed sample was mounted in thermosetting plastic leaving only one side exposed. The thermosetting plastic was a hot mount Bakelite resin. After the thermosetting plastic dried, the exposed surface areas of the sample were used for further analysis.

3.3.2 Preparation for metallography

The exposed oval-like alloyed quarter surface of the mounted samples shown in Figure 19 (c) schematic was wet ground with silicon carbide papers from 220 to 1200 grit for each alloy. Before every subsequent step the samples exposed area was rinsed in distilled water and air dried. Thereafter all the samples were polished with several successively finer polishing grits. Finally distilled water was used to clean the sample, acetone was used to degrease the sample, and the samples were dried using a hair dryer. The sample microstructure was examined using a Zeiss Axiotech 25 HD microscope and JSM 5800 LV SEM with energy dispersive X-ray spectroscopy (EDX).

For the optical microscopy the stainless steel samples were etched with a reagent that had one part HNO_3, one part HCl and one part H_2O. The samples were stirred in the solution at 20°C for uniform, stain-free results. The reagent further outlined the button welds constituents and revealed grain structure. Finally distilled water was used to clean the sample, and acetone was used to dry and degrease the sample. The EDX and SEM analysis were carried out using an electron microprobe set to 10 kV accelerating voltage and 200 nA beam current.

Spectrometry Analysis was carried out on the as received samples of 316L and LDX 2101 to determine the elemental composition of the samples prior to welding. The Optical Emission Spectrometer for metal analysis, Bruker Q4 Tasman was used to carry out the test. ISO 78-2:1999 for chemical analysis was the utilized standard.

3.4 Stage 3: Solidification and Heat treatments

3.4.1 Heat treatment of samples

316L samples required no further heat treatment once samples had undergone Ru addition via GTAW. The 316L samples post weld, exhibited satisfactory microstructural homogenization of the different phases. However, the duplex stainless steels unlike austenitic stainless steels require additional heat treatment due to the microstructural changes that occur during welding. Duplex stainless steels have both the beneficial properties of ferritic and austenitic steels. The size and distribution of the ferrite and austenite phases is dependent on both the thermomechanical cycles and heat treatment. Once LDX 2101 button welds have been formed by GTAW the DSS requires a heat treatment at high temperatures (typically 1000-1200°C) to transform the ferrite in the austenite. Close attention must be paid to the cooling rate and kinetics of the system.

The correct heat treatment and rapid cooling can eliminate intermetallic phases from forming that can be detrimental to the toughness and strength of the weld metal. The button weld samples need to undergo isothermal heat treatment to establish austenite and ferrite contents evenly distributed throughout the matrix. Therefore, the button welds underwent isothermal heat treatment at temperatures of 1050°C for 1 hour thereafter these were water quenched to obtain a duplex microstructure. The temperature range was selected based on a TTT diagram shown in Figure 20 for lean duplex stainless steels (Olaseinde, et al., 2015).

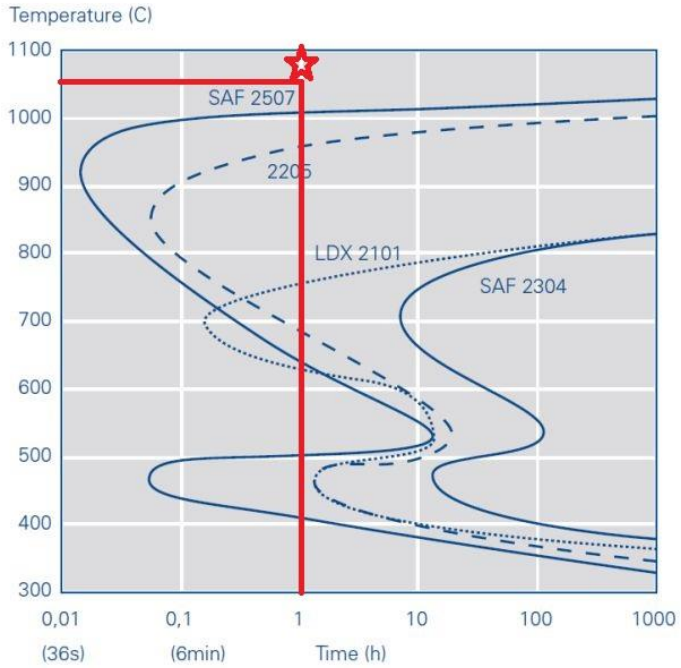


Figure 20: TTT Diagram of Outokumpu duplex stainless steel LDX 2101® and the heat treatment utilised (British Stainless Steel Association, 2016).

3.4.2 Mode of solidification characterisation

The integrity and performance of a weld is, to a large extent, controlled by the solidification behavior of the weld metal or fusion zone. During the fabrication of the GTA button welds with the compact vacuum arc melting system from Mintek, the copper mould is continuously cooled with circulating water. This resulted in rapid solidification, and affected the mode of solidification, additionally the microstructural features were much finer, and solute segregation patterns were altered. For conventional welding processes such as gas tungsten arc as used in the experiment, cooling rates in the order of 103 °C/s were expected.

Schaeffler and DeLong constitutional diagrams (Schaeffler, 1949) (DeLong, 1973) are successfully used to predict the ferrite content in austenitic stainless steel welds at room temperature. This ferrite content is typically quantified by the ferrite number (FN). The WRC-92 diagram is however preferred to be used to determine the mode of solidification for duplex stainless steels. The mode of solidification was therefore determined by calculating the Ni equivalent (Ni_{eq}) and Cr equivalent (Cr_{eq}).

The Ni_{eq} and Cr_{eq} equations were estimated by imputing the EDX elemental bulk analysis results in the following equations (Siewert & Kotechi, 1992).

$$\mathbf{Ni_{eq}} = \%\mathbf{Ni} + \mathbf{35} \times \%\mathbf{C} + \mathbf{20} \times \%\mathbf{N} + \mathbf{0.25} \times \%\mathbf{Cu} \qquad \textbf{Equation 22}$$

$$\mathbf{Cr_{eq}} = \%\mathbf{Cr} + \%\mathbf{Mo} + \mathbf{0.7} \times \%\mathbf{Nb} \qquad \textbf{Equation 23}$$

By using the WRC-92 diagram the mode of solidification could be determined for 316L and for LDX 2101 stainless steel button welds.

Austenitic Stainless steels

It is therefore important to determine the ferrite number (FN) to gauge the susceptibility of the weld to hot cracking. Some researchers challenge that 3 to 8 volume percent delta ferrite is required to reduce hot cracking susceptibility. The content of delta ferrite should not exceed 10% because at higher contents, secondary phase such as sigma (σ) phase could occur. However, ferrite alone is not sufficient to prevent hot cracking in the presence of a ferrite – austenite (FA) mode of solidification is also beneficial. The FN can be determined using the Schaeffler diagram for 316L austenitic stainless steels.

Duplex stainless steel

The mode of solidification for duplex stainless steels such as LDX 2101 can be determined by using the WRC-92 diagram (Siewert & Kotechi, 1992). The WRC-92 diagram has the solidification mode boundaries indicated. Similarly, to the austenitic stainless steel the Ni equivalent (Ni_{eq}) and Cr equivalent (Cr_{eq}) can be used to extrapolate the mode of solidification from the WRC-92 diagram. This diagram was noted to be more accurate due to the higher Nitrogen coefficient being removed. The Ferrite Number (FN) can also be determined by extrapolating from the WRC-92 graph.

3.5 Stage 4: Corrosion tests

In order to study the effect of Ru additions on the general and pitting corrosion of the samples in diluted NaCl solution electrochemical tests were conducted. Potentiodynamic electrochemical tests were performed and the cyclic polarization characteristics were determined.

3.5.1 Sample preparation –Corrosion test

A single quarter of each of the alloyed samples was used from each sample. Each quarter sample was placed face down and the rear end connected to an insulated copper wire with aluminium adhesive tape. Thereafter samples were cold mounted in resin leaving one side exposed for interaction with the corrosive environment during testing.

3.5.2 Potentiodynamic polarisation test

The potentiodynamic tests will be conducted mostly by following ASTM G61-86 (ASTM Standard G61 1986-1998). An Autolab PGSTAT302 with a differential electrometer amplifier, controlled by computer, was used to conduct the potentiodynamic tests.

The cell setup:

The prepared samples were exposed to aqueous environment namely 1 M NaCl. The electrochemical cell was composed of about 500 ml NaCl aqueous solution in a beaker as the electrolyte, a glassy carbon electrode as the counter electrode; silver/silver chloride [Ag/AgCl, KCl (3 M)] electrode as the reference electrode and the sample was tested as the working electrode. The electrochemical cell was partially immersed in a water thermal bath with a temperature controller in order to control the cell electrolyte temperature throughout the experiment. A thermometer was placed in the electrolyte in order to continuously monitor the actual temperature of the electrolyte and, the thermal bath temperature was adjusted accordingly. This was to ensure that temperature remains constant and does not influence the test results because if the temperature is too high it will accelerate the corrosion rate.

3.5.3 Actual test setup technique

The glassy carbon counter electrode was connected to the counter electrode terminal of the PGSTAT302, similarly the silver/silver chloride [Ag/AgCl, KCl (3M)] reference electrode to the reference electrode terminal and the sample to be tested to working electrode terminal. Each sample was anodically polarised separately by connecting it to the working electrode terminal of the PGSTAT302.

3.5.4 Open Circuit Potential (OCP)

The cyclic voltammetry potentiostatic technique of Metrohm Autolab Nova software was used to conduct the polarisation scans. The open circuit potential for each scan was determined 1 h after immersing the sample in the electrolyte. The OCP is the voltage of the electrode (in this case the sample) measured against a reference electrode using a high impedance voltmeter so that no current flows between the working electrode in question and the reference electrode. It is the corrosion potential of the sample being tested in the aqueous solution.

3.5.5 Potentiodynamic polarization

After determining the open circuit potential each sample was anodically polarised at a scan rate of 0.167 $mV.s^{-1}$ from 200 mV to -200 mV. This had to be below its open circuit potential/corrosion potential, passing through the corrosion potential to more noble values.

For each scan, the scan was reversed at 1 $mA.cm^{-2}$ and, where applicable, the repassivation potentials of the alloys were determined. It is important to note that fresh NaCl aqueous solution was used for each polarisation scan, and the electrolyte temperature was maintained at 25 ± 2°C throughout each the experiment.

3.5.6 Parameters

A number of parameters were used to indicate corrosion resistance. These included the corrosion rate (mm/annum); the observed corrosion potential, Ecorr (V); the passivation exchange current density, i_{pass} (A/cm^2); the open-circuit potential, OCP (V); and the critical exchange current, i_{crit} (A).

3.5.7 Corrosion rate determination

Corrosion rate can be determined electrochemically from measured polarization curves from the Nova Autolab software using polarization behavior:

1. Tafel extrapolation,
2. Non linear least squares fit to ideal equation, which is similar in form to the Butler-Volmer equation, and
3. Linear polarization resistance.

In this study the use of Tafel extrapolation and linear polarisation resistance were used.

3.5.7.1 Tafel extrapolation

The electrochemical reactions under activation control, polarization curves exhibiting linear behavior in the E Vs log (i) plots also known as Tafel behaviour, were used for extrapolation.

The corrosion current I_{corr}, corrosion potential E_{corr}, and corrosion rate as presented in Table VIII and Table XVI for 316L and LDX 2101 respectively were directly extracted from the Metrohm Autolab Nova software for each potentiodynamic curve. Correct estimates of the Tafel slopes were possible by choosing two points on the linear Tafel region of each slope which were at least a decade in current apart.

3.5.7.2 Linear polarization resistance

Polarization methods are faster experimental techniques compared to classical weight loss estimation. The slope of the E Vs log (i) plot near the E_{corr} value is defined as polarization resistance (Rp) as shown in Figure 21.

In this region Ohms Law, Equation 24 applies therefore:

$$\mathbf{R_p = \frac{\Delta E}{\Delta i} \quad where\ \Delta E \rightarrow 0} \qquad \textbf{Equation 24}$$

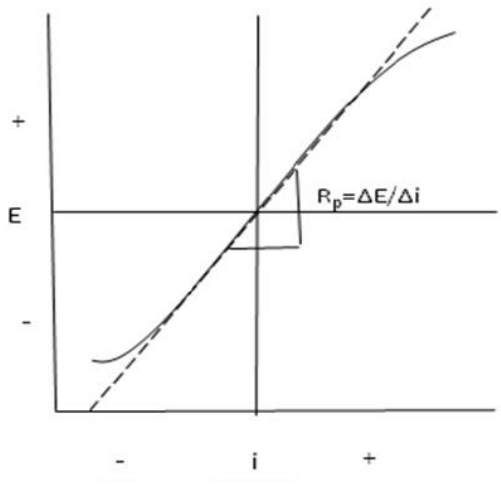


Figure 21: Linear Polarisation Resistance curve (K.A.Natarajan, 2012).

The extent of linearity of the E Vs log (i) plot depends on βa and βc values which can be obtained from the Metrohm Autolab Nova software.

3.6 Stage 5: Post corrosion tests metallography

3.6.1 Optical microscope: Pitting corrosion evaluation

Mechanical failures have a number of causes can be caused by a number of reasons. These need not necessarily be applied stresses, but can also be residual stresses from manufacturing operations such as forming and welding. After potentiodynamic polarisation, the evaluated 316L and LDX 2101 samples were examined under a metallurgical microscope for the physical presence of pits.

The range of duplex steels allows them to be matched for corrosion resistance with the austenitic and ferritic steel grades. It was convenient to use the Pitting Resistance Equivalent Number (PREN) in Equation 7 as a means of ranking the grades. Researchers have shown that the higher the PREN value, the greater the materials pitting resistance.

3.7 Stage 6: Mechanical properties

3.7.1 Hardness test: Post GTA welding

Vickers hardness tests were carried out on the Bakelite samples for the 316L and LDX 2101. Hardness profile measurements of the button welds were measured with micro hardness 10 HV and a dwell time of 30 seconds. The exact positioning of the test points was towards the centre of the sample, as ISO 9015-1 standard specific for arc joints (Struers, 2012).

Chapter 4

4 Results and Discussion

The results of the microscopic investigation by light microscope and SEM will be discussed in this section. The spectrometer results of as received samples will also be discussed. The results for the 316L ASS mode of solidification are shown and the corrosion resistance quantified using the potentiodynamic polarization curves. The corrosion rate was then calculated using Tafel and linear polarization. The pitting corrosion susceptibility was assessed using an optical microscope. The mechanical properties are evaluated using Vickers hardness. The results for LDX 2101 are also shown similarly.

4.1 Microstructural evaluation: GTAW button 316L samples

4.1.1 Optical Microscope - 316L ASS

Metallographic analysis exhibited the phase constituents of each sample. The electrochemically etched 316L ASS standard sample is shown in Figure 22. Austenitic and ferrite regions are shown.

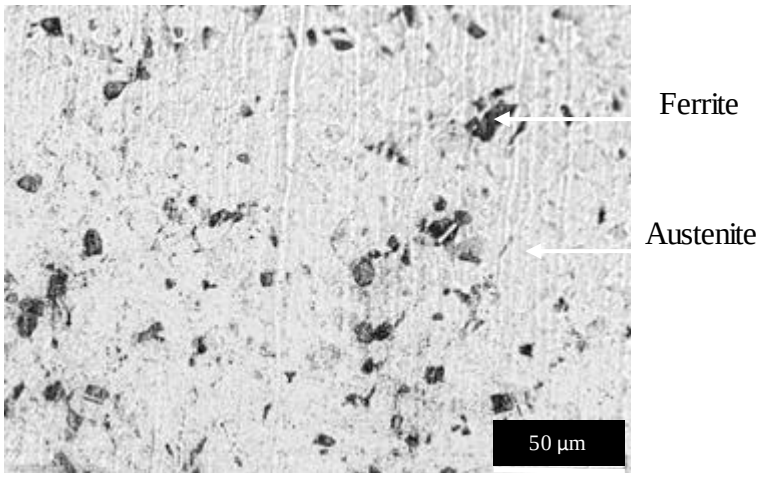


Figure 22: Optical micrograph of 316L ASS as-received standard material etched with one part HNO_3, one part HCl and one part H_2O.

The microstructural evaluation of the GTAW button welds depicted the typical fusion boundary microstructure for GTA welded 316L ASS at 20x magnification in Figure 23(a) to (d). The 316L weld metal solidifies as primary δ ferrite dendrites as shown in Figure 23(a) to (d) with increasing Ru addition. During solid state transformation, ferrite transforms to austenite by a diffusion controlled process. Under normal weld solidification conditions, the solidification mode in ASS is

a function of composition, with a shift from primary ferrite to primary austenite accomplished by reducing the Creq/Nieq ratio to below 1.5 (Perricone, et al., 2007).

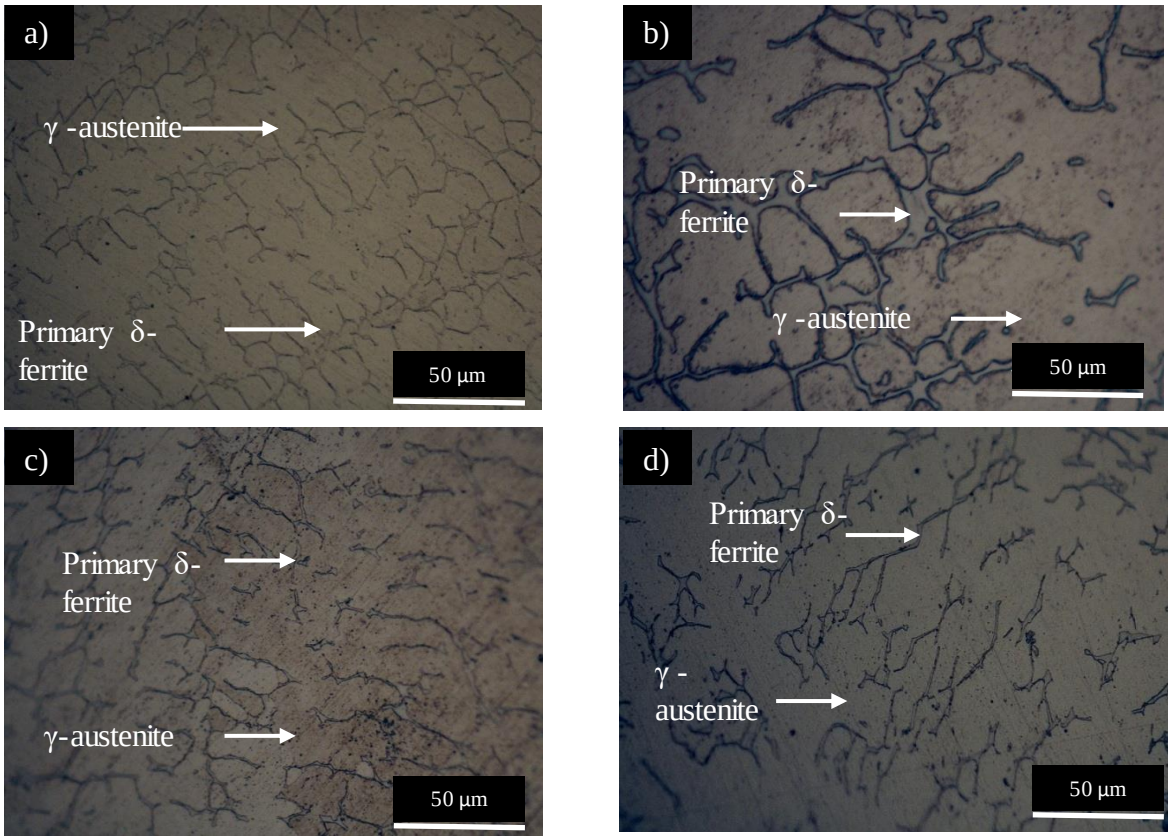


Figure 23: (a) 0.1 wt% Ru (b) 0.5 wt% Ru (c) 1wt% Ru and (d): 2 wt% Ru to 316L ASS after GTAW

Columnar dendrite zones were observed in all the 316L button welds with increasing Ru addition. Figure 23(a) to (d) show the columnar dendrite zone and the typical morphologies of σ-ferrite in the fusion zone for 0.1 wt%, 0.5 wt%, 1 wt% and 2 wt% Ru additions respectively. The typical morphology is: (a) lathy δ (ferrite) with 0.1 wt% Ru addition and (d) skeletal microstructure with lathy δ-ferrite in the 2 wt% Ru 316L button weld. This ferrite morphology was observed due to the melting of the 316L into a conical shaped copper mould. Baldission et al (2007) suggested that formation of this ferrite morphology was a result of the suppression of the δ→γ (austenite) solid-state transformation due to higher cooling rate (Baldissin, et al., 2007).

4.1.2 Spectrometry results for 316L ASS.

The spectrometer results of the as received samples of 316L ASS are shown in Table VI.

Table VI: The spectrometry results of 316L ASS as received.

C	Fe	Si	Mn	Cr	Mo	Ni	Cu	N	Ti	W
0.022	69.50	0.453	1.522	17.03	1.788	9.205	0.120	0.052	0.024	0.063

The elemental composition is similar to literature specification described in section 2.2.1. The actual nitrogen content is lower than the 0.1% suggested by literature. The nitrogen in the metal helps to balance the weld metal. The addition of alloying element increases the activity coefficient of nitrogen; the solubility of nitrogen will decrease.

4.1.3 Scanning Electron Microscope (SEM) and Energy-dispersive X-ray spectroscopy (EDX) analysis

316L SEM and EDX results for 316L ASS

Figure 24 to Figure 27 shows the microstructure obtained using SEM- Backscattered electron detector (BSE) image with a 10 µm scale. The regions were analysed for chemical composition to determine the phase present and their composition.

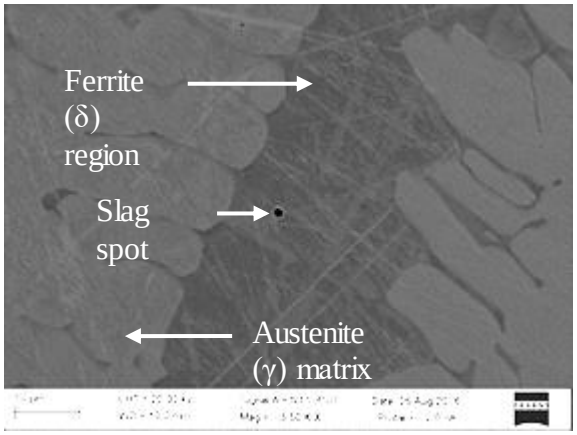


Figure 24: The SEM back scattered image for 0.1 wt% Ru alloyed 316L button welded sample.

The microstructure showed the expected dual phase microstructure of δ-ferrite and γ-austenite. The austenite phase appeared brighter and the ferrite phase darker due to the face centered cubic structure of austenite, compared to ferrite which has a body centered cubic structure. The lattice parameters of austenite are larger than that of ferrite. In addition the austenite formers will

concentrate in the austenite phase, such as nickel, in same way chromium will concentrate in the ferrite phase. Figure 24 showed a thick primary (δ) ferrite region at 0.1% Ru addition, this extended to lathy, thin dendritic arms.

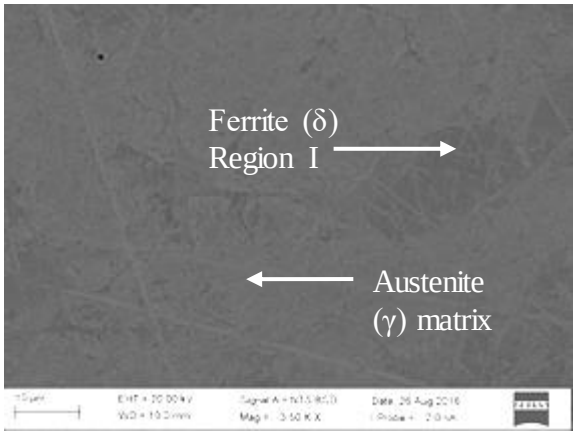


Figure 25: The SEM back scattered image for 0.5 wt% Ru alloyed 316L button welded sample.

The 0.5 wt% Ru addition micrograph Figure 25 showed a reduction in the dendritic structure thickness. The Ru distribution did not remain homogenous throughout the microstructure. Figure 26 showed the back scattered image for the 1 wt% Ru addition to the 316L ASS, the dendrite arm sizing reduced further with a more homogenous bulk microstructure, with a relatively even distributed volume of fraction of austenite to ferrite.

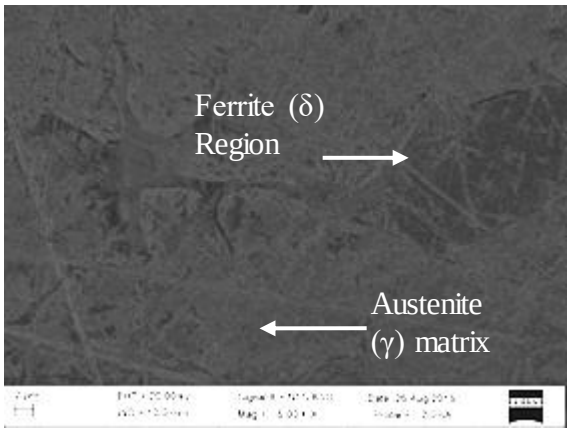


Figure 26: The SEM back scattered image for 1 wt% Ru alloyed 316L button welded sample.

Figure 27 shows δ-ferrite region for the 2 wt% Ru addition. The ferrite region is enriched in Cr and depleted in Ni and its morphology appears more skeletal in nature. The grains now appear far thinner than the 0.1 wt%, 0.5 wt% and 1 wt% Ru addition.

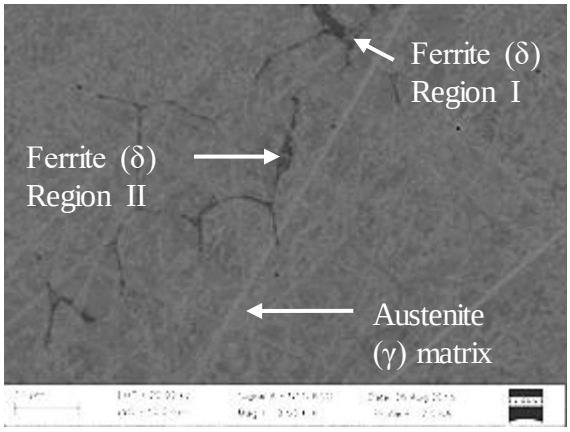


Figure 27: The SEM back scattered image for 2 wt% Ru alloyed 316L button welded sample.

The addition of a noble metal such as Ru has grain refining capabilities (Baldissin, et al., 2007). The EDX analysis of the matrix (austenite region) of the 2 wt% Ru button weld shown in Figure 28 indicate enrichment in Cr and depletion in Ni. The EDX was also used to verify the phases identified in the micrographs.

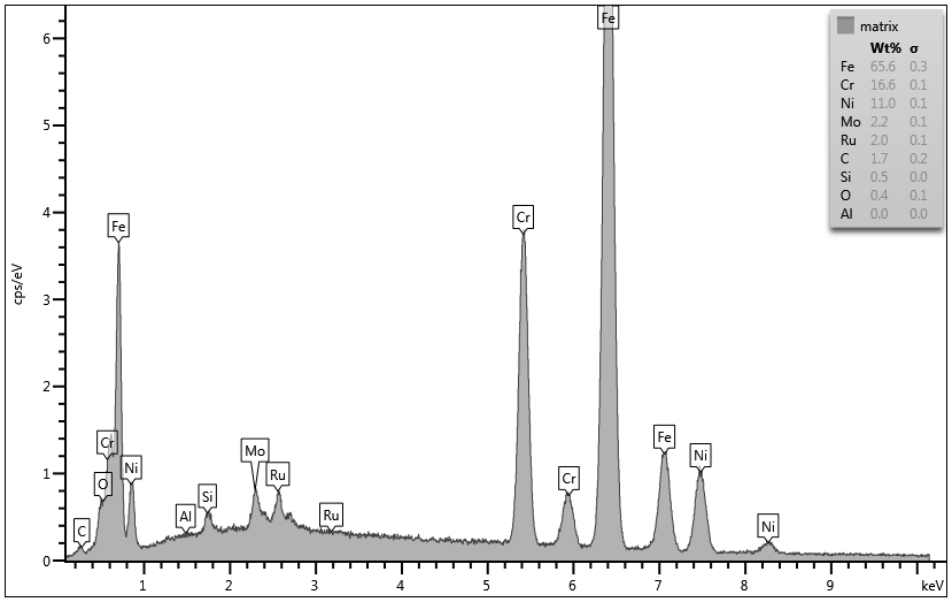


Figure 28: EDX analysis of matrix region of the 2 wt% Ru sample.

Due to the fast cooling nature of the copper hearth the austenite region had been enriched in Ni and depleted of Cr. The Ni diffused in the ferrite towards the advancing austenite (Kujanpaa, et

al., 1986). The Cr was rejected by the advancing interface as shown by the EDX microprobe results. The chemical compositions of the different phases for the 2 wt% sample are shown in Table VII.

Table VII: Chemical Compositions of GTAW 316L button samples alloyed with 2 wt% Ru analysed by EDX.

Phases	**Elements (wt %)**							
	Cr	Ni	Mn	Mo	Fe	Si	Ru	Ti
Region I **Ferrite (δ)**	21.3±.1	5.1±0.1	-	3.6±0.1	61.3±0.2	0.8±0.1	1.8±0.2	-
Region II **Ferrite (δ)**	15.2±0.1	9.2±0.2	1.4±0.1	2.1±0.1	55.7±0.3	0.5±0.2	1.7±0.3	2.9±0
Matrix **Austenite (γ)**	16.6±0.2	11±0.1	-	2.2±0.1	65.6±0.1	0.5±0.2	2±0	-
Overall Composition	16±01	11±01	1.5±0.2	2.7±0.1	66±0.1	0.8±0.1	1.9±0.1	

The ruthenium distribution was homogenous throughout the weld bead and this was shown in the EDX results. The elemental composition of the alloyed 316L with Ru is consistent throughout the material. Titanium was detected after welding as slag forming compounds (such as Ti, Ca, and Al) accumulate together and precipitate as a spot on the button welds (Collins, 1997). The solidification behaviour of these alloys was categorized into four basic solidification modes according to the morphologic criteria presented in the literature by several authors (Brooks, et al., 1991) (Junwei, et al., 2009).

4.1.4 Mode of Solidification for 316L

Figure 29 depicts the Schaeffler constituents diagram used to predict or determine the stainless steel weld metal structure.

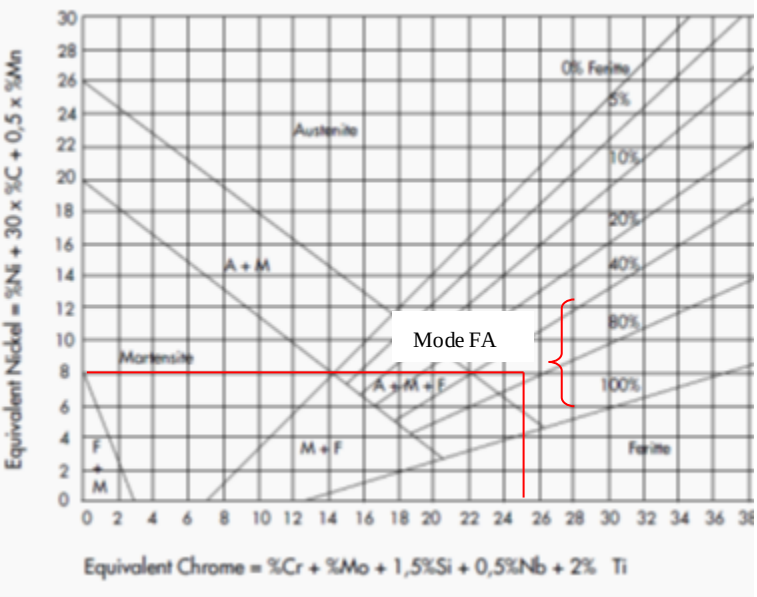


Figure 29: Schaeffler diagram for stainless steel weld metal (British Stainless Steel Association, 2016).

The Ni_{eq} and Cr_{eq} equations can be estimated by imputing the EDX analysis results from Table VIII in the following equations (Siewert & Kotechi, 1992).

$$\mathbf{Ni_{eq}} = \%\mathbf{Ni} + \mathbf{35} \times \%\mathbf{C} + \mathbf{20} \times \%\mathbf{N} + \mathbf{0.25} \times \%\mathbf{Cu} \qquad \textbf{Equation 25}$$

$$\mathbf{Cr_{eq}} = \%\mathbf{Cr} + \%\mathbf{Mo} + \mathbf{0.7} \times \%\mathbf{Nb} \qquad \textbf{Equation 26}$$

In the current study, the solidification mode was characterised as FA alloys for GTAW 316L ASS. FA alloys consist of primary δ-ferrite with a eutectic γ at the end of solidification. Under equilibrium solidification conditions, the 316L ASS exhibited a mixed mode of freezing (Perricone, et al., 2007).

The Table VIII shows the Cr_{eq} and Ni_{eq} ratio of as received samples of 316L and Ru containing samples.

Table VIII: The Creq to Nieq ratios of as received samples for 316L and Ru containing alloys.

	0 wt% Ru	0.1 wt% Ru	0.5 wt% Ru	1 wt% Ru	2 wt% Ru
Ni_{eq}	11.045	11.04	10.16	11.33	12.77
Cr_{eq}	18.823	18.9	19.1	21.2	24.9
Ratio	1.704	1.66	1.88	1.87	1.95

The following ratio was used to determine the type of mode of solidification.

F mode $1.95 \leq Cr_{eq}/Ni_{eq}$

FA mode……$1.48 \leq Cr_{eq}/Ni_{eq} \leq 1.95$

A, AF mode $Cr_{eq}/Ni_{eq} \leq 1.14$

With 2 wt% Ru addition to the weld metal the Cr_{eq} /Ni_{eq} ratio was in the range of 1:48-1:95 and therefore it was classified as a FA alloy. This confirmed the microstructural phases observed in the optical microscope and SEM images analysis. With Mo contents of ±2.5 wt% the microstructure could contain the Mo-rich σ-sigma intermetallic, often as a coupled growth with γ-austenite (Perricone, et al., 2007). The EDX results for this Mo bearing 316L ASS showed that it had a homogenous chemical distribution throughout the different phases. Numerous studies have demonstrated the susceptibility of Mo-depleted regions of the microstructure to preferential corrosive attack when the chemical distribution of the alloy is not homogenous (Girner, 1979)(Garner, 1982)(Rockel & Renner, 1984). This can further be assisted by the addition of Ru to the weld metal of 316L ASS by GTAW, to further decrease susceptibility to corrosion attack the particularly when sample is homogenous.

4.1.5 316L Hardness results

The Vickers hardness tests were carried out according to ISO 9015-1:2001 using a Future-Tech FM-800 Vickers Hardness testing instrument (ISO, 2001). Figure 29 shows the influence of Ru addition on the hardness of GTAW 316L button samples. The hardness results showed that 316L has an increase in hardness as Ru addition was increased due to grain refining nature of Ru.

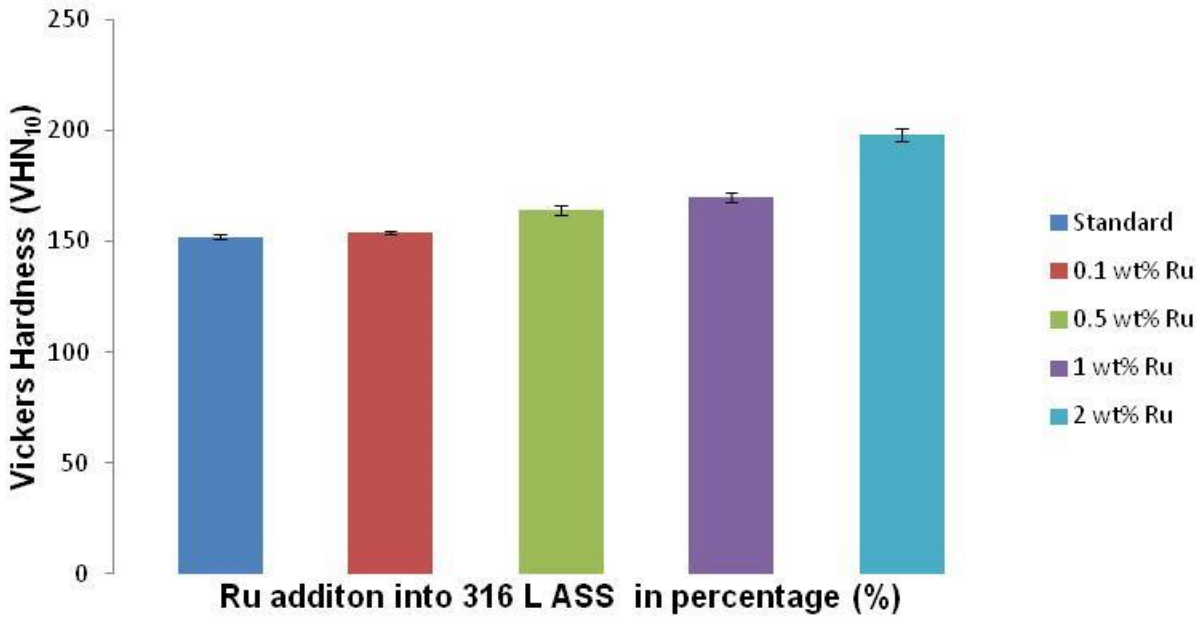


Figure 29: Vickers hardness test results for different Ru additions for the GTAW 316L button samples at: 0.1 wt%, 0.5 wt %, 1 wt % and 2 wt % Ru additions.

The Vickers hardness measurements of the button weld substrate interface revealed a significant increase in hardness with increased Ru addition, varying from 152 HV for the AISI 316L parent material to 198 HV for the GTAW button samples, for 2 wt% Ru alloyed sample shown in Figure 29. The increased hardness of alloys with 1 wt% Ru and 2 wt% Ru as compared to the 0.1 wt% Ru and 0.5 wt% Ru can be attributed to their high Ru and Ni content, as well as the microstructural changes due to heating in the vacuum arc furnace. The Ru was evenly distributed in the solution, precipitates were not noted. The hardening effect of both Ru and Ni on alloys is well-known (Hampel, 1954).

4.2 Potentiodynamic results

The potentiodynamic results for 0.1 wt% to 2 wt% Ru addition were analysed. Each sample was analysed against the control sample to assess the effect Ru additions have on the corrosion resistance of the stainless steel.

4.2.1 316L Potentiodynamic curves

The introduction of a PGM such as Ru into 316L was expected to give a general improvement of corrosion resistance of the ASS by shifting the corrosion potentials to nobler values. Figure 30 shows the potentiodynamic curves of 0.1 wt%, 0.5 wt%, 1 wt% and 2 wt% Ru containing GTAW 316L button welds in 1 M NaCl.

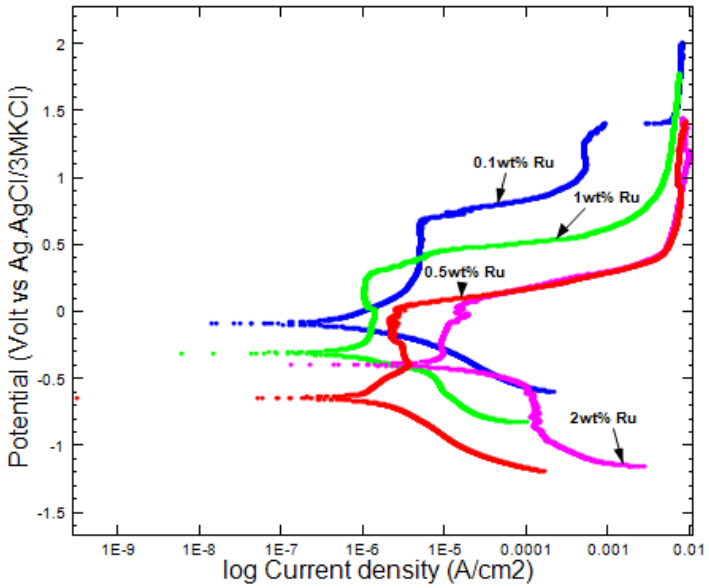


Figure 30: Potentiodynamic polarisation curves for 0.1 wt%, 0.5 wt%, 1 wt% and 2 wt% Ru addition to 316L GTA welded buttons in 1M NaCl.

Figure 30 shows the potentiodynamic polarisation curves obtained when the GTA welded samples were anodically polarised in 1 M NaCl aerated solution at 25°C ±1°C following the procedure stated in section 3.5. The samples were scanned from -160 mV to 160 mV.

Figure 31 shows the comparison potentiodynamic polarization test in 1M NaCl between the control sample and the effect of 0.5 wt% Ru addition to the 316L ASS.

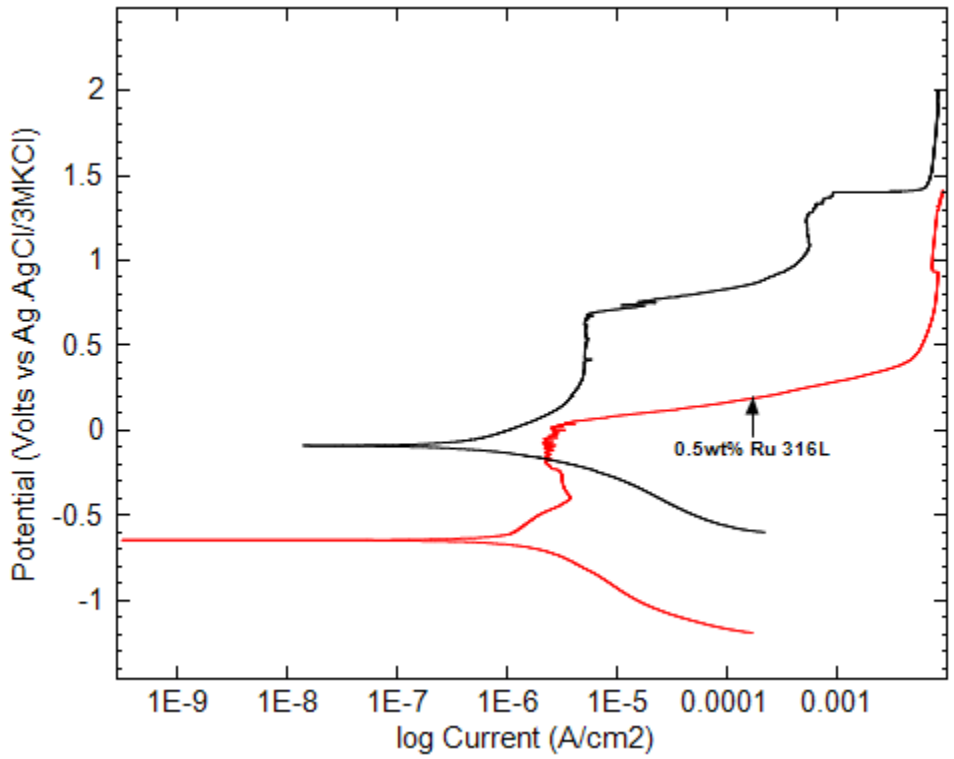


Figure 31: The potentiodynamic polarisation curves of E vs log (i) for standard 0 wt% Ru addition GTAW 316L button weld and 0.5 wt% Ru addition.

The addition of 0.5 wt% Ru shifted the corrosion potentials to more negative values. Scan began at -1.60 V, the curve passed through the observed corrosion potential of -0.63 V. At just above -0.60 V an increase in current density was observed, suggesting the onset of pit initiation. E_{pit} was observed above 0 V (SCE) potential for 0.5 wt% Ru addition. At +0.1 V potential the current density increased with a slightly stabilized polarisation potential. However when 1 wt% Ru was added to 316L the corrosion potential became more positive, as shown in Figure 32. Compared to the corrosion result of 0.5 wt% Ru addition.

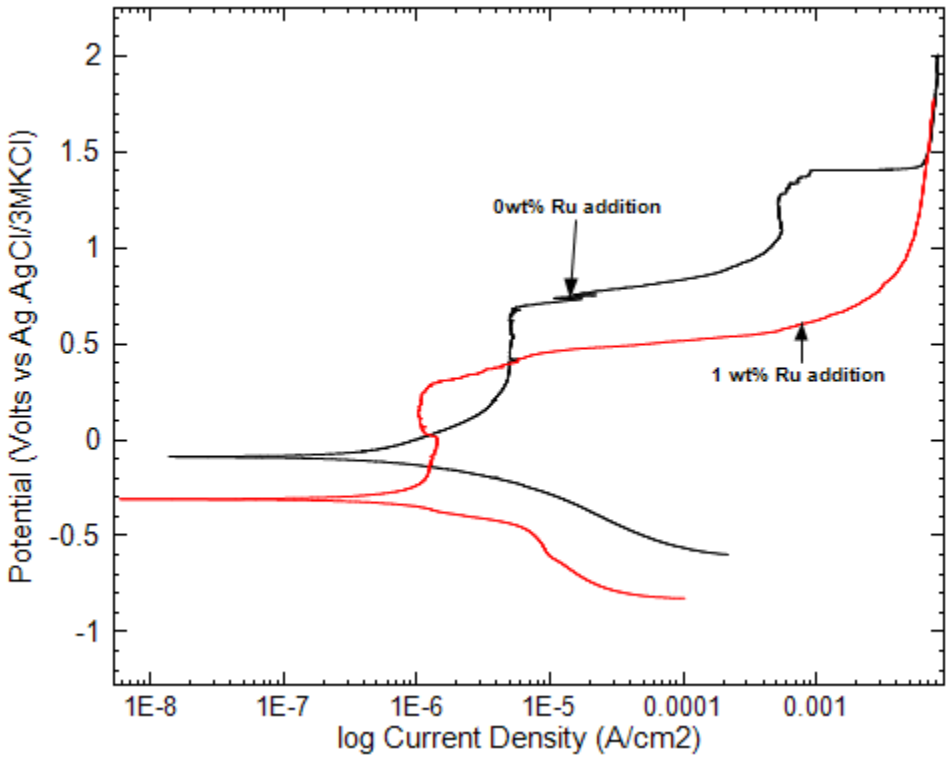


Figure 32: The potentiodynamic polarisation curves of E vs log (i) for standard 0 wt% Ru addition GTAW 316L button weld and 1 wt% Ru addition.

The 1 wt% Ru sample was scanned from -0.8 V. The curve passed through the observed corrosion potential of -0.3 V. At -0.3 V an increase in current density was observed, suggesting the point of pit initiation. At +0.4 V potential the current density increased with little or no increase in polarisation potential. The 1 wt% Ru curve passed the anodic and passive region of the standard material. The 1 wt% Ru addition shifted the corrosion potential and the passive point to more negative values.

As more Ru was added to the 316L to values of 2 wt%, the potentiodynamic curve as per Figure 33 was observed.

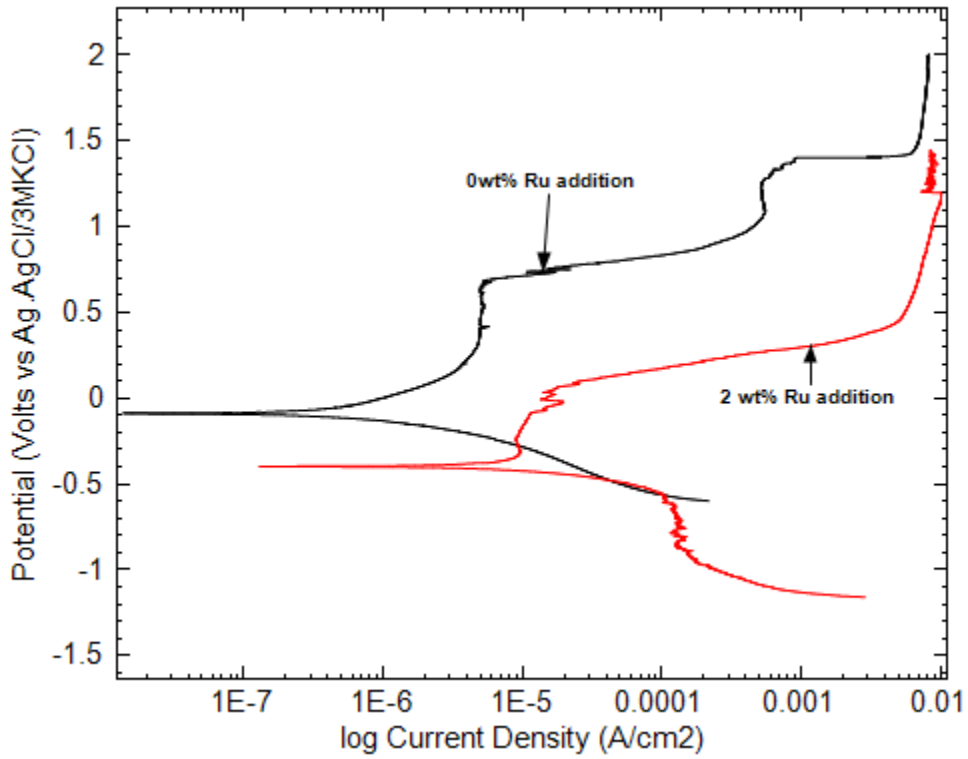


Figure 33: The potentiodynamic polarisation curves of E vs log (i) for standard 0 wt% Ru addition GTAW 316L button weld to 2 wt% Ru addition.

The 2 wt% Ru sample was scanned from -1.3 V. The curve passed through the observed corrosion potential of -0.4 V. At -0.3 V an increase in current density was observed, suggesting the point of pit initiation. At +0.1 to about +0.2 V potential the current density increased with slight increase in polarisation. The 2 wt% Ru curve was seen to pass the cathodic region of the standard 316L GTAW material, thus promoting the cathodic reaction.

4.2.2 Corrosion rate

4.2.3 316L Corrosion rate

The corrosion rate for the 316L was evaluated using the Tafel and Linear polarisation techniques.

4.2.3.1 Tafel Extrapolation

Table IX shows the potentiodynamic polarization data obtained from Nova Software 2011 for the 316L GTAW button samples after exposure to 1 M NaCl.

Table IX: Potentiodynamic polarization data for 316L.

Sample	βa (mV/dec)	βc (mV/dec)	Ecorr (mV)	I corr (µA)	CR (mm/yr)
0.1 wt % Ru	655.5	227.8	-81.271	1.27	0.013
0.5 wt % Ru	98,15	206.8	-255.48	5.29	0.053
1 wt % Ru	127.6	91.8	-205.3	4.628	0.0461
2 wt % Ru	134.5	358.4	-300	5.2	0.052

The more negative the standard electrode potential, the greater the tendency to form metal ions and hence to corrode. The results from the tafel extrapolation depicted that the corrosion rate increased with increase in Ru addition from 0.1 wt% ad 0.5 wt%.

4.2.3.2 Linear Polarisation

The linear polarization method was applied according to Section 2.13 and the equivalent weight for 316L taken to be 27.56 g/mol, the exposed surface area of each sample as 1 cm^2 and the density of 316L (7.8 kg/dm^3), the following corrosion rates were determined as shown in Table X. Subscripts “a” and “c” stand for anodic and cathodic, respectively, while. β_a and β_c are Tafel slopes. $\beta_a = \beta_c = 0.1$ was used as explained by Jones in the literature review (Jones, 1996).

Table X: Potentiodynamic polarization corrosion rate data for 316L using linear polarisation.

Sample	βa (V/dec)	βc (V/dec)	I corr (μA)	Rp (Ω.)	CR (mm/yr)
0.1 wt % Ru	0.1	0.1	0.267	81476	0.0027
0.5 wt % Ru	0.1	0.1	6.74	32.24	0.0692
1 wt % Ru	0.1	0.1	8.48	256.45	0.087
2 wt % Ru	0.1	0.1	1.10	19.739	0.01

The corrosion rate decreased as Ru was increased from 0.1 wt% to 0.5 wt%. However, at 1 wt% a slightly favourable decrease was noticed. For the 2 wt% Ru addition the corrosion rate increased compared to the 1 wt% Ru addition. Based on the potentiondynamic polarisation curves this proves that at 2 wt% Ru the cathodic reaction was promoted hence reducing the polarization resistance (Rp) and increasing the corrosion rate.

4.2.4 Pitting Corrosion for 316L

Once the passive film is breached, an electrochemical cell becomes active. Iron (Fe) goes into solution in the more anodic bottom of the pit, diffuses toward the top, and oxidizes to iron oxide. The concentration of the iron chloride solution in a pit can increase as the pit deepens. The pitting resistance equivalent (PREN) for 316L was calculated according to Equation 7 to be 24.

Figure 34 shows the 0.1 wt% Ru sample post potentiodynamic polarization in 1 M NaCl.

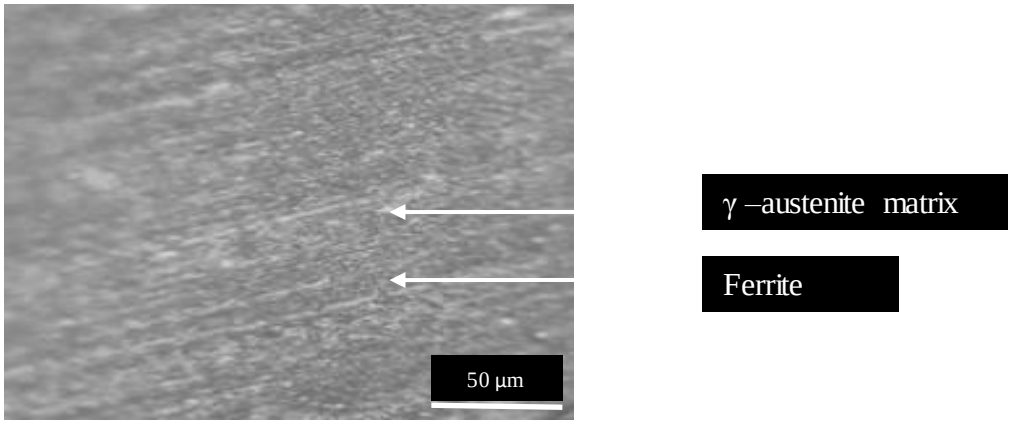


Figure 34: Surface of the 0.1 wt% Ru 316L corroded sample after potentiodynamic polarisation in 1 M NaCl.

Very little corrosion was observed on the electrode substrate. As more Ru was added, in Figure 35 to 0.5 wt% Ru, no surface perforation was observed. The pitting corrosion pits observed for 316L ASS was significantly lower than the LDX 2101. The pitting corrosion of 316L control sample is slightly higher than the 0.5 wt% Ru addition.

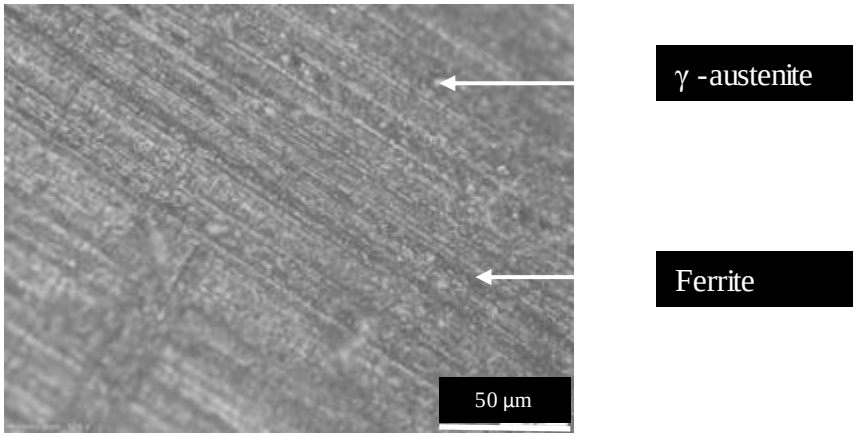


Figure 35: Surface of the 0.5 wt% Ru 316L corroded sample after potentiodynamic polarisation in 1 M NaCl.

Once Ru addition reached 1 wt% addition, pit initiation occurred on certain parts of the sample as shown in Figure 36. The pits were a result of localized corrosion confined to a small area in the metal surface, in the form of a small cavity. This is due to the particle having a different electrochemical potential from the surrounding metal matrix. Therefore this pitting occurred in surface regions where the corrosion protective layer is absent.

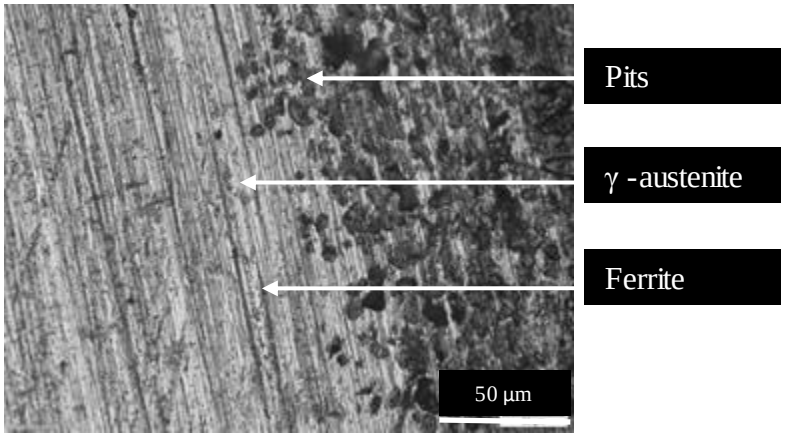


Figure 36: Surface of the 1 wt% Ru 316L corroded sample after potentiodynamic polarisation in 1 M NaCl.

At 2 wt% Ru addition uniform corrosion on sample surface is seen. The sample was severely corroded as shown in Figure 37.

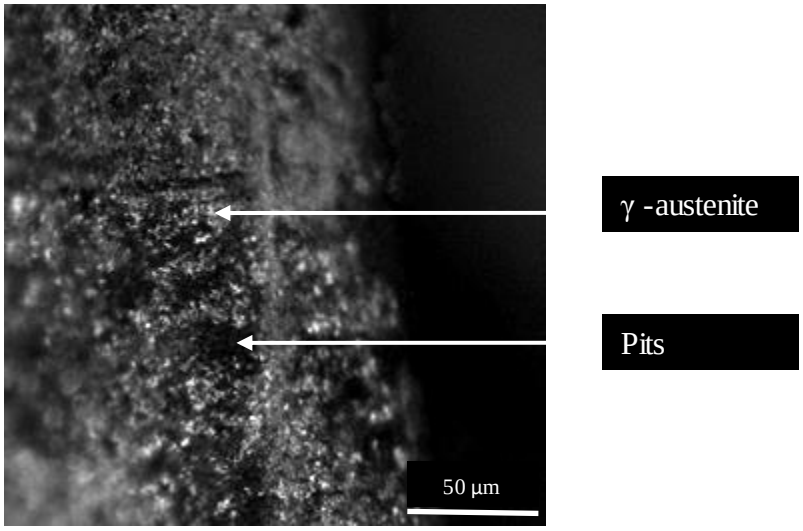


Figure 37: Surface of the 2 wt% Ru 316L corroded sample after potentiodynamic polarisation in 1 M NaCl.

In Figure 37 the corroded 316L samples with 2 wt% Ru addition were analysed. The sample underwent severe pitting corrosion. Ruthenium addition in this case increased corrosion rates as it increases the efficiency of the cathodic hydrogen reaction. Therefore, passivation could be induced only if the passivation potential of the PGM metal alloy was less than the overpotential of the hydrogen evolution reaction on the alloying PGM. In application in industry the consequences of accelerated pitting, can lead to perforation, leaks and/or mechanical failures.

4.3 Microstructural evaluation: GTAW button LDX 2101 samples

4.3.1 Optical microscope: LDX 2101 duplex stainless steel

The etched LDX 2101 DSS is shown in Figure 38 . The lean duplex stainless steel showed dark ferrite regions and light austenitic regions at 20X magnification. The austenite and ferrite showed alternating bands in the direction of rolling.

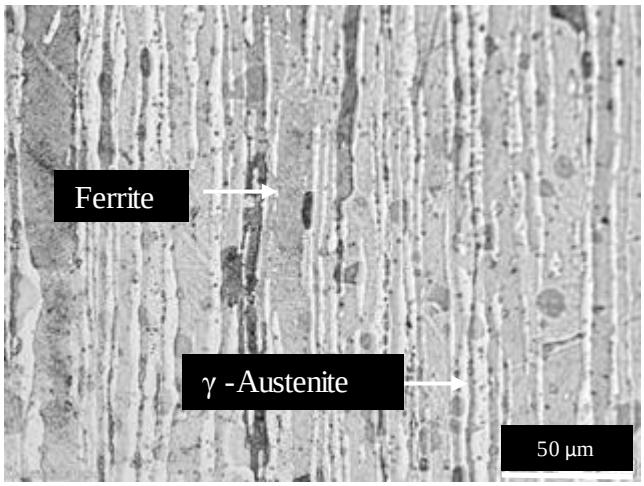


Figure 38: Optical micrograph of LDX 2101 as-received standard material etched with one part HNO_3, one part HCl and one part H_2O.

The volume fractions were calculated using quantitative metallography, and the results of the as-received samples are given in Table XI. The proportion of each phase was determined and verified by using five micrographs for analysis. Thereafter a mean was calculated, divided by the number of points in the grid, and multiplied by one hundred, to give the results in terms of the volume percent of phase (Rhines, 1968).

Table XI: Volume fraction of LDX 2101 DSS using quantitative metallurgy.

Alloy	2101-as received	2101-after GTAW	2101- after heat treatment
Ferrite	51.3±5.8	81.5±0.1	50.5±0.2
Austenite	41.7±5.7	18.5±0.1	49.5±0.2

An increase in soaking time at 1050°C according to literature produces an increase in the proportion of the austenite phase. Therefore, to establish a homogenous austenite to ferrite ratio, 1 hour soak time was administered. Figure 39 and Figure 40 shows the optical micrographs of LDX 2101 for 0.1 wt% Ru before heat treatment and after heat treatment respectively. The volume fraction was 80:20, ferrite to austenite for the 0.1 wt% Ru button sample before heat treatment. The matrix is shown as ferrite (dark matrix) and austenite as light grains. The distribution of the phases was not homogenous therefore heat treatment was required. Figure 40 shows the microstructure of the GTA welded button LDX 2101 sample after a post weld heat treatment.

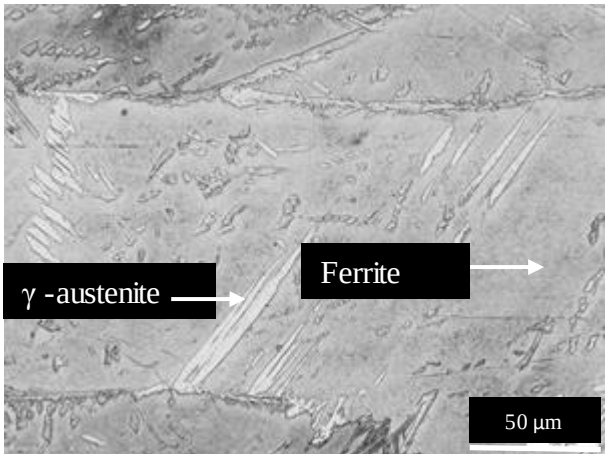


Figure 39: 0.1 wt% Ru in LDX 2101 DSS before heat treatment etched with one part HNO_3, one part HCl and one part H_2O.

Figure 40 shows the microstructure of the GTA welded button LDX 2101 sample after a post weld heat treatment.

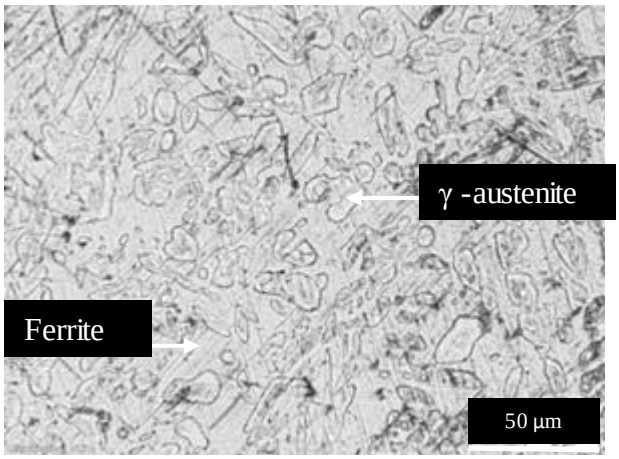


Figure 40: 0.1 wt% Ru in LDX 2101 DSS after heat treatment etched with one part HNO_3, one part HCl and one part H_2O.

The post weld treatment allowed the LDX 2101 to have a volume fraction of austenite to ferrite as 50.2:49.8, with the austenite phase being the round shaped particles in the microstructure. This heat treatment allowed values close to the homogenous 50:50 austenite to ferrite ratio to be reached for LDX 2101. Therefore, due to the favourable microstructure sufficient motivation was established to have a post weld treatment to improve microstructural properties of the welded LDX 2101 but also additionally improve the mechanical properties.

After the post weld heat treatment the 0.1 wt%, 0.5 wt%, 1 wt% and 2 wt% Ru addition to LDX 2101 button samples showed volume fractions as indicated in Table XII.

Table XII: Volume fraction of LDX 2101 DSS using quantitative metallurgy.

LDX 2101 (After Heat treatment)	0 wt% Ru	0.1 wt% Ru	0.5 wt% Ru	1 wt% Ru	2 wt% Ru
Ferrite	51.3±5.8	50.2±0.2	51.0±1.5	53.0±4	47±5
Austenite	41.7±5.8	49.8±0.2	49.0±2.0	40±6	60±6

The microstructure for LDX 2101 with 0.1 wt%, 0.5 wt%, 1 wt% and 2 wt% Ru addition are shown in Figure 41 to 45.

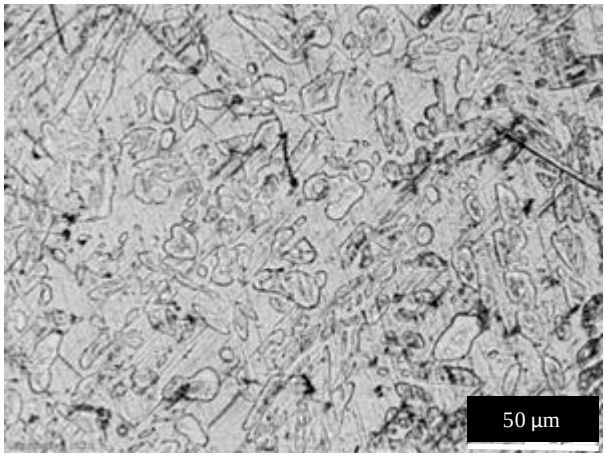


Figure 41: Micrograph of 0.1 wt% Ru addition into LDX 2101 GTAW buttons etched with one part HNO_3, one part HCl and one part H_2O.

The round austenite regions are present in the 0.1 wt% Ru sample; these grains were homogeneously distributed throughout the ferrite matrix. The shape of the grains may result in a softened material due the post weld heat treatment.

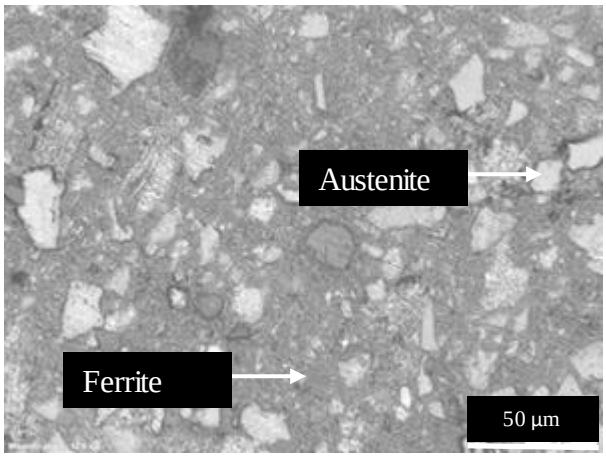


Figure 42: Micrograph of 0.5 wt% Ru addition into LDX 2101 GTAW buttons etched with one part HNO_3, one part HCl and one part H_2O.

Figure 42 once etched revealed two phases, austenite and ferrite. Ferrite depicted as the dark matrix and austenite as lighter phase present. The austenite particles were homogeneously distributed in the ferrite matrix.

The volume fraction of austenite to ferrite was 49.0±2.0 to 51.0±1.5. At 1 wt% Ru addition the micrograph in Figure 43 was taken for the etched sample.

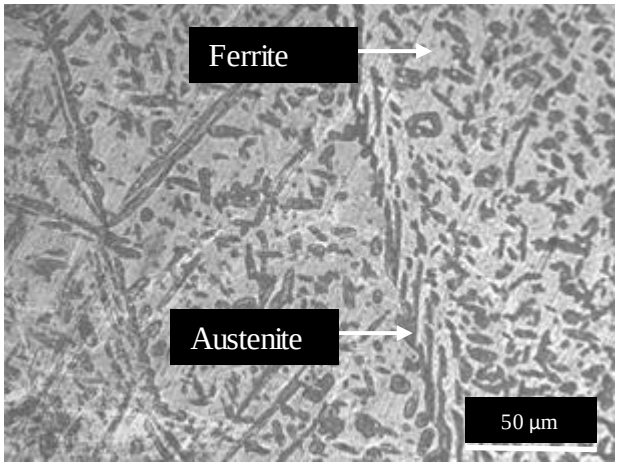


Figure 43 : Micrograph of 1 wt% Ru addition into LDX 2101 GTAW buttons etched with one part HNO_3, one part HCl and one part H_2O.

The austenite phase appeared as elongated particles and the ferrite as the matrix. As more Ru was added as was shown in Figure 44 the austenite grains became thinner and arranged into sub grain boundaries.

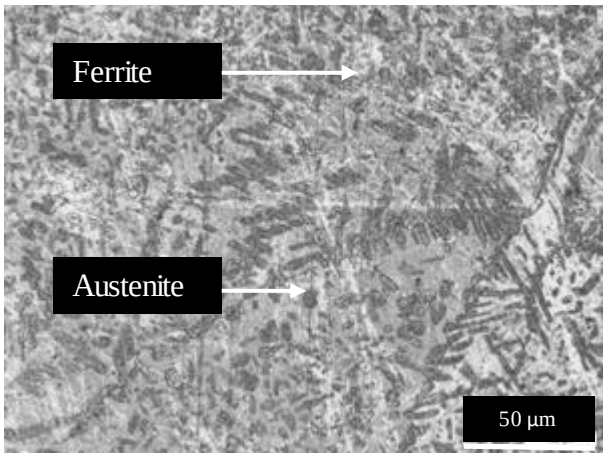


Figure 44: Micrograph of 2 wt% Ru addition into LDX 2101 GTAW buttons etched with one part HNO_3, one part HCl and one part H_2O.

The 2 wt% Ru optical micrograph showed thin austenitic grains which verified the Ru grain refining capability.

4.3.2 Spectrometry results for LDX 2101

The spectrometer results of the as received samples for LDX 2101 in Table XIII were as follows.

Table XIII: The spectrometry results elemental composition for LDX 2101.

C	Fe	Si	Mn	Cr	Mo	Ni	Cu	N	Ti	W
0.028	69.88	0.664	4.920	21.82	0.195	1.576	0.425	0.3	0.0046	0.031

The elemental composition was similar to literature specification described in section 2.4.1. The actual nitrogen content was higher than the N content from literature. The Mo was lower than the 0.3% suggested by literature. The nitrogen in the metal helps to balance the weld metal microstructure improving the in-service corrosion performance, particularly pitting corrosion resistance. As duplex stainless steels are used for their good corrosion resistance, the presence of nitrogen assists in reducing scrapping rates and additional costs.

4.3.3 2101 SEM and EDX results

The SEM analysis was carried out for all LDX 2101 GTAW button samples with increasing Ru additions. Figure 45 to Figure 47 depict the microstructures for 0.1 wt% Ru to 2 wt% Ru addition after the post weld treatment of 1 hour soak time at 1050°C.

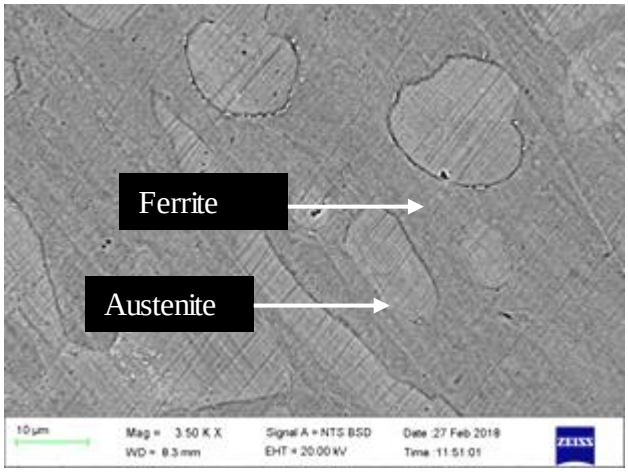


Figure 45: The SEM back scattered image for 0.1 wt% Ru alloyed LDX 2101 button welded sample.

The austenite (light) and ferrite (dark) phases were identified in Figure 45. The austenite region appeared elongated and globular in shape. The austenite particles were well dispersed in the ferrite matrix and some were formed at the grain boundaries.

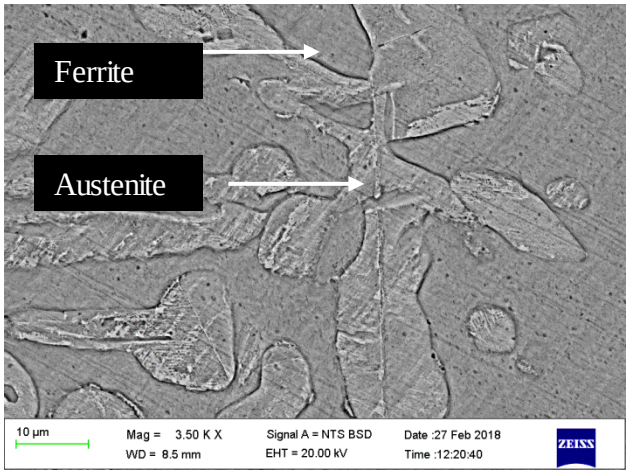


Figure 46: The SEM back scattered image for 0.5 wt% Ru alloyed LDX 2101 button welded sample.

As more Ru was added from 0.1 wt% to 0.5 wt% to the LDX 2101 DSS in Figure 46, the austenite region began to thin and elongate. When 1 wt% Ru is added in Figure 47 the sharp edged grains begin to appear more prevalent. The globular shaped austenite regions were still present.

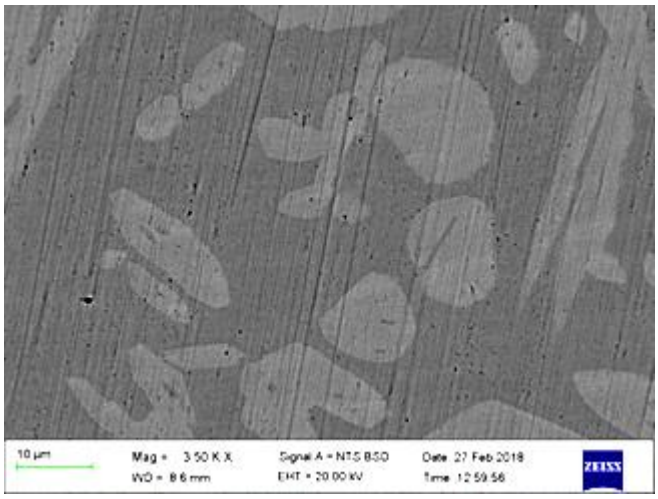


Figure 47: The SEM back scattered image for 1 wt% Ru alloyed LDX 2101 button welded sample.

The austenite elongated grains began to form tapered sharp edges in the 2 wt% back scattered SEM image. Figure 48 was considered as proof of Ru grain refining capability.

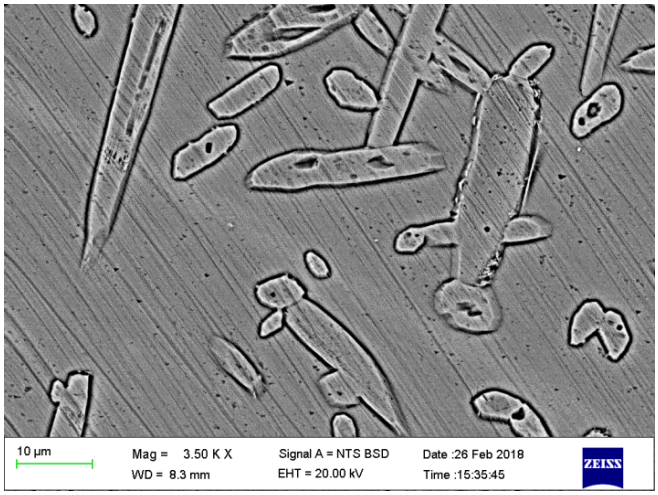


Figure 48: The SEM back scattered image for 2 wt% Ru alloyed LDX 2101 button welded sample.

Sigma (σ) phase was not found after the heat treatment. This phase forms typically due to a eutectoid-type reaction of $\alpha \rightarrow \sigma + \gamma_2$ during tempering treatment. This σ phase typically causes the hardness of the steel to increase. The impact toughness and corrosion resistance of DSS would have decreased if the percentage of σ phase increased.

The EDX analysis was used to verify the phases found and also to analyse more carefully the effect of Ru on the microstructure and elemental distribution. The EDX was carried out on all four variations with increasing the Ru weight percentage as shown in Table XIV.

Table XIV: Chemical Compositions (wt %) of LDX 2101 button samples alloyed increasing Ru analysed by EDX analysis.

Phases	**Elements (wt %)**							
	Cr	Ni	Mn	Mo	Cu	Si	Ru	Fe
0.1 wt%	22.3±0.2	1.6±0.1	4.57±0.2	-	0.5±0.1	0.8±0.2	0.18±0.1	67.43±0.1
0.5 wt%	21.9±0.1	1.6±0.1	4.76±0.1	-	0.4±0.1	0.8±0.2	0.48±0.1	67.99±0.1
1 wt%	22.2±0.1	1.6±0.1	4.81±0.1		0.5±0.1	0.8±0.3	1.2±0.1	69.33±0.1
2 wt%	21.6.±0.1	1.5±0.1	4.57±0.1	-	0.5±0.2	0.8±0.2	1.60±0.2	67.43±0.1

The EDX analyses showed the two phases, austenite and ferrite, in as-received 2101 duplex stainless steel. The EDX analyses of 2101 gave the following elements: Cr, Ni, Mo, Si, Mn, and Fe. The ferrite phase had a higher proportion of Mg, Si, Ca, Cr and Mo, while austenite had a higher proportion of Al, S, Mn, Fe and Ni. As more Ru was added more austenite region was observed. The ferrite phase was found to be enriched in Cr and Mo, while Ni and N were concentrated in the austenite phase.

4.3.3.1 Mode of solidification for LDX 2101

Using the Ni and Cr equivalents the mode of solidification could be determined. By imputing the bulk EDX analysis into Equation 5 and Equation 6 the Ni to Cr ratio was calculated to be 1.5 to 21.5. Table XV shows the Cr_{eq} and Ni_{eq} of the as received samples of LDX 2101 and Ru containing alloys.

Table XV: The Cr_{eq} to Ni_{eq} ratios of as received samples for LDX 2101 and Ru containing alloys.

	0 wt% Ru	0.1 wt% Ru	0.5 wt% Ru	1 wt% Ru	2 wt% Ru
Ni_{eq}	7.710	8.8185	8.16	8.185	8.19
Cr_{eq}	22.023	22.3	21.9	22.2	21.6
Ratio	2.88	2.529	2.68	2.71	2.63

The following ratio was used to determine the type of mode of solidification.

F mode $1.95 \leq Cr_{eq}/Ni_{eq}$

FA mode……$1.48 \leq Cr_{eq}/Ni_{eq} \leq 1.95$

A, AF mode $Cr_{eq}/Ni_{eq} \leq 1.14$

By using the Schaeffler diagram for stainless steel weld metal in Figure 49 the mode of solidification was determined to be an F mode.

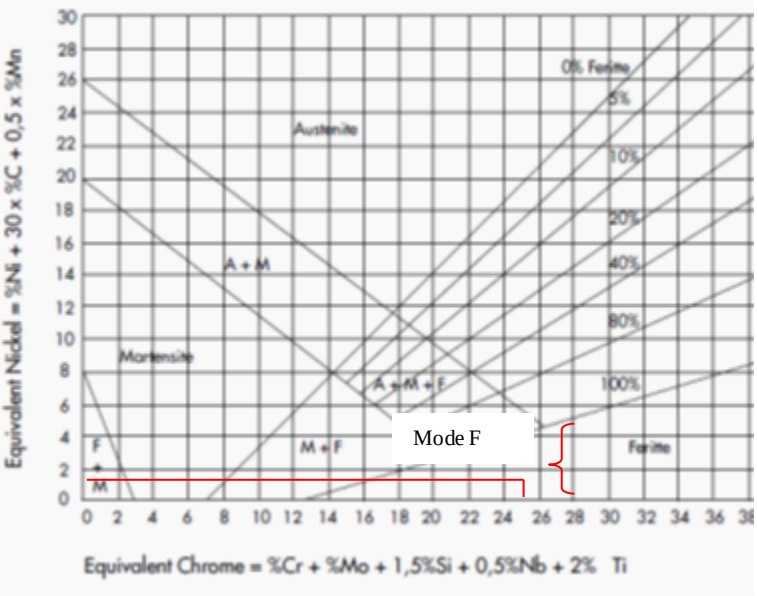


Figure 49: Schaeffler diagram for stainless steel weld metal (British Stainless Steel Association, 2016).

Duplex stainless steels solidify in a ferrite mode and therefore the microstructures of the heat affected zone were fully ferritic at temperatures of 1350± 50°C. Nitrogen has a prominent effect on the formation of ferrite in the LDX 2101, as the dissolution of austenite occurs primarily via the diffusion of nitrogen.

4.4 Hardness results

The Vickers hardness tests were carried out according to ISO 9015-1:2001 using a Future-Tech FM-800 Vickers Hardness testing instrument (ISO, 2001).

4.4.1 LDX 2101

As more Ru was added to the GTAW button welds for LDX 2101, a significant improvement in the hardness of the samples was observed after a post weld heat treatment as shown in Figure 50.

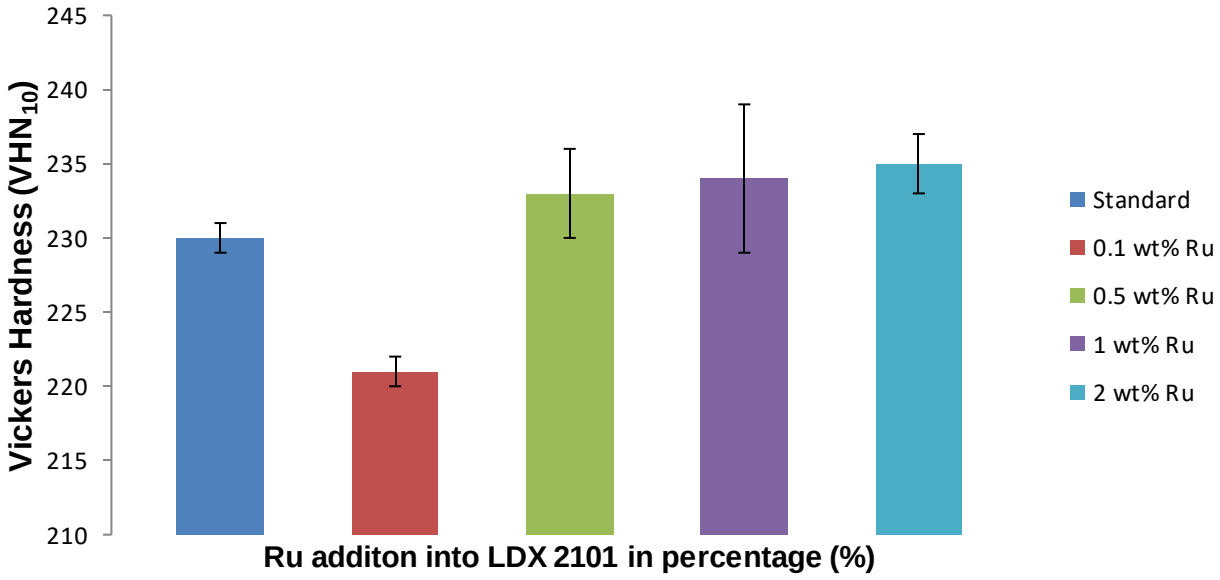


Figure 50: Vickers hardness test results for different Ru additions for the LDX 2101 button samples at: 0.1 wt%, 0.5 wt%, 1 wt% and 2 wt% Ru additions.

The as-received sample had a hardness of approximately 232 HV, once 0.1 wt% Ru was added a slight decline in the hardness profile was noted. The microstructure present in 0.1 wt% had very globular grain structures after heat treatment which is characteristic of lower hardness materials. However, as more Ru was added the grains became thinner and elongated. The hardness values increase to values of 235 HV for 2 wt% Ru addition from 230 HV for the 0 wt% Ru as received material.

4.4.2 LDX 2101 Potentiodynamic curves

Figure 51 shows the potentiodynamic polarisation curves obtained when the GTA welded samples with increasing Ru addition were anodically polarised in 1 M NaCl aerated solution at 25°C ±1°C following the procedure stated in section 3.5. The samples were scanned from -200 mV to 200 mV.

In the current study, the addition of Ru to DSS was expected to improve the corrosion resistance of the alloy as a result of the ability of Ru to inhibit the anodic reactions as well as modify the efficiency of the cathodic process of the alloy.

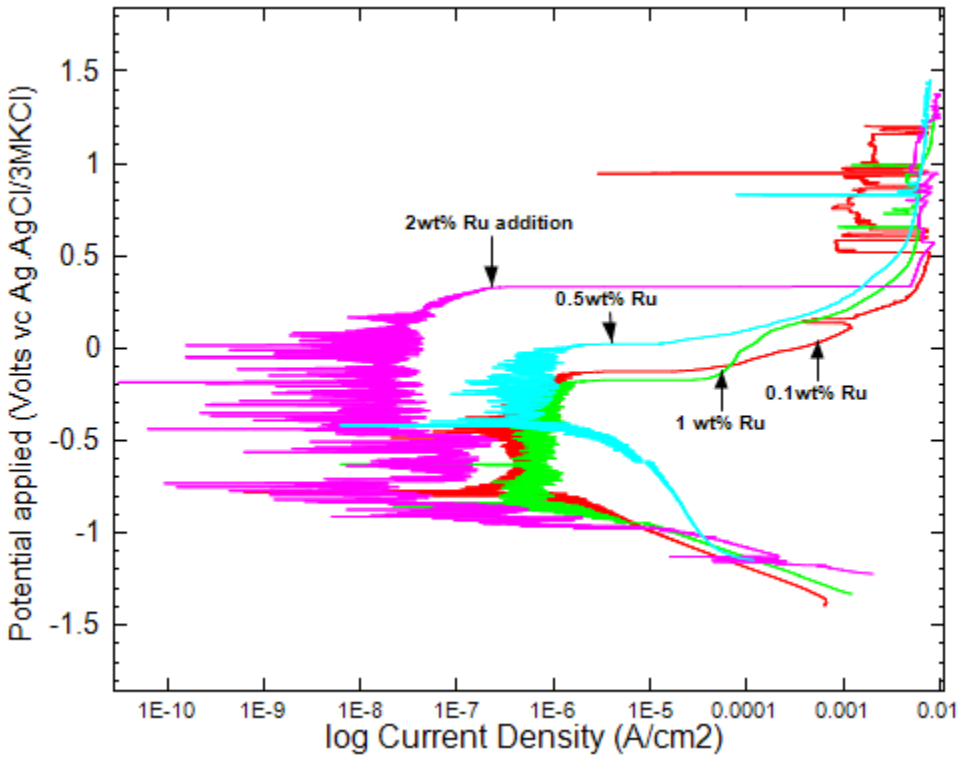


Figure 51: Potentiodynamic polarisation curves for 0.1 wt%, 0.5 wt%, 1 wt% and 2 wt% Ru addition to LDX 2101 DSS GTA welded buttons in 1M NaCl.

Figure 51 shows the potentiodynamic polarisation curves obtained when the GTA welded samples were anodically polarised in 1 M NaCl aerated solution at 25°C ±1°C following the procedure described in section 3.5. The samples were scanned from -1.4 V to 1.4 V.

Figure 52 shows the effect of 0.5 wt% Ru addition to the LDX 2101 once it has undergone potentiodynamic polarization test in 1 M NaCl.

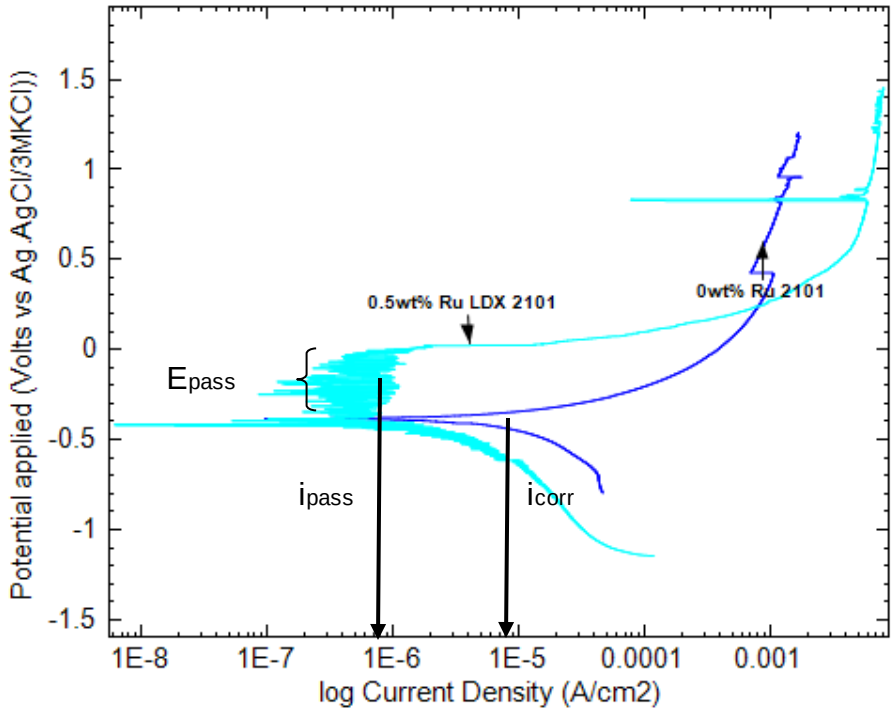


Figure 52: The potentiodynamic polarisation curve (E vs log (i)) for the standard 0 wt% Ru addition GTAW LDX 2101 button weld compared with the 0.5 wt% Ru sample.

The 0.5 wt% polarization curve shifted to more positive corrosion potentials. Scan began at -1.30 V, the curve passed through the observed corrosion potential of -0.4 V. At 0.1 V an increase in current density was observed, suggesting that this was the point of pit initiation. E_{pit} was observed above 0 V (SCE) potential for 0.5 wt% Ru addition. The E_{pass} region was indicated from -0.4 V to 0.1 V with a passivation current density (i_{pass}) of $9x10^{-7}$ A/cm^2. The i_{corr} of the control sample was $9x10^{-6}$ A/cm^2.

When 1 wt% Ru was added to LDX 2101 the corrosion potential moved to more negative values as shown in Figure 53.

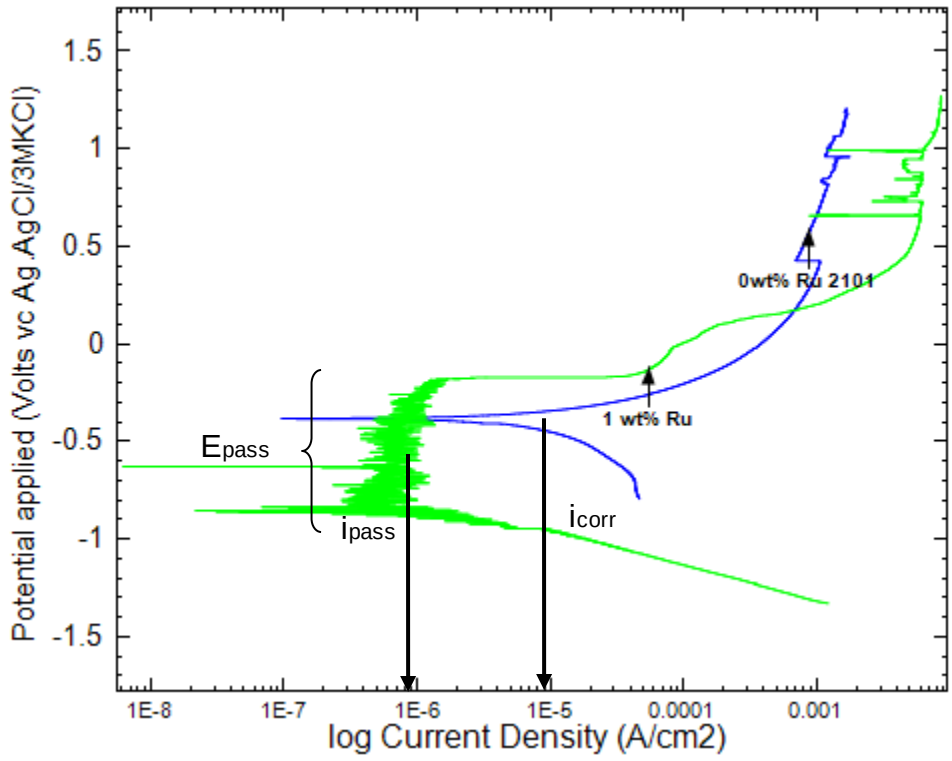


Figure 53: The potentiodynamic polarisation curves (E vs log (i)) for the standard 0 wt% Ru addition GTAW LDX 2101 button weld compared with the 1 wt% Ru sample.

The 1 wt% Ru sample was scanned from -1.3 V to 1.4 V. The curve passed through the observed corrosion potential of -0.8 V. At -0.2 V an increase in current density was observed, suggesting that this was the point of pit initiation. At -0.2 V the current density increased dramatically indicating transpassive behaviour. The E_{pass} region was indicated from -0.9 V to -0.1 V with a passivation current density (i_{pass}) of $9x10^{-7}$ A/cm^2. The i_{corr} of the control sample was $9x10^{-6}$ A/cm^2.

More Ru was added to the LDX 2101 to values of 2 wt%, the potentiodynamic curve as per Figure 54 was observed.

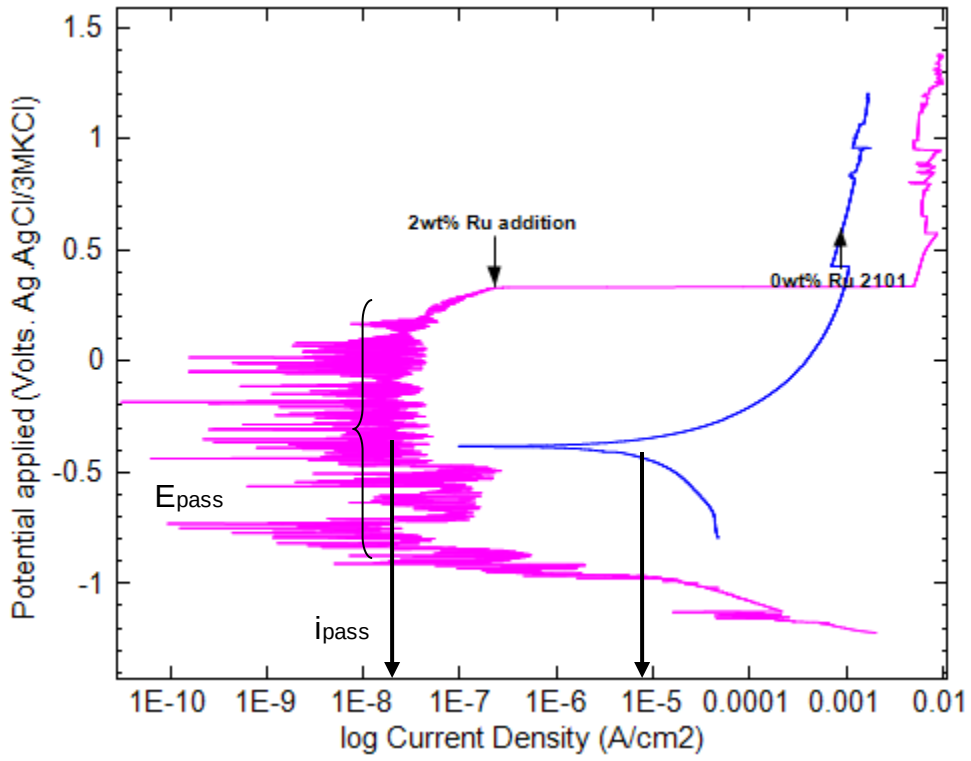


Figure 54: The potentiodynamic polarisation curves (E vs log (i)) for the standard 0 wt% Ru addition GTAW LDX 2101 button weld compared with the 2 wt% Ru sample.

The 2 wt% Ru sample was scanned from -1.3 V to 1.4 V. The curve passed through the observed corrosion potential of -0.7 V. At 0.2 V an increase in current density was observed, suggesting that this was the point of pit initiation. The E_{pass} region was indicated from -0.7 V to -0.2 V with a passivation current density (i_{pass}) of $4x10^{-8}$ A/cm^2. The i_{corr} of the control sample was $9x10^{-6}$ A/cm^2. The 2 wt% Ru curve was seen to pass the passive region of the standard LDX 2101 GTAW material. The 2 wt% Ru curve shifted to more negative corrosion potential and lower values of current density. The presence of Ru slightly improved the general and pitting corrosion of LDX 2101 in 1 M NaCl. From the obtained results it is inferred that the pitting potential (Epit) and the repassivation potential (Erp) are shifted to more negative (active) values with Ru addition, corresponding to increased susceptibility towards the aggressive pitting attack of Cl anions.

4.5 Corrosion rate

4.5.1 LDX 2101 Corrosion rate

4.5.1.1 Tafel extrapolation

The Tafel extrapolation showed the following corrosion rates for 0.1 wt%, 0.5 wt%, 1 wt% and 2 wt% Ru addition to LDX 2101 after potentiodynamic polarization. Table XVI shows the corrosion rates of LDX 2101 from 0.1 wt% to 2 wt% Ru addition.

Table XVI: Potentiodynamic polarization data for LDX 2101.

Sample	βa (mV/dec)	βc (V/dec)	Ecorr (mV)	I corr (µA)	CR (mm/yr)
0.1 wt % Ru	171.01	126.38	-377.40	4.58	0.05
0.5 wt % Ru	172.16	82.0	-409	3.41	0.00039
1 wt % Ru	168.8	261.0	-86.03	2.55	0.0029
2 wt % Ru	198.3	82.0	-194.08	6.06	0.07

According to Tafel extrapolation as Ru addition increased from 0.1 wt% to 0.5 wt% there was a decrease in the corrosion rate. At 1 wt% Ru addition corrosion rate remained decreased due to addition of Ru compared to 0.1 wt% Ru addition. However, with 2 wt% Ru addition the corrosion rate increase compared to 0.1 wt%.

4.5.1.2 Linear Polarisation

The corrosion rate was determined as described in Section 2.13 , where equivalent weight, the exposed surface area of each sample and the density of LDX 2101 (7.8 kg/dm^3) were input to determine the results in Table XVII. Subscripts “a” and “c” stand for anodic and cathodic, respectively, while. β_a and β_c are Tafel slopes. $\beta_a = \beta_c = 0.1$ was used as is explained by Jones in literature Section 2.13 (Jones, 1996). Linear polarization offers a more accurate measure for corrosion rate at instantaneous points within the cycle.

Table XVII: Potentiodynamic polarization corrosion rate data for LDX 2101 using linear polarisation.

Sample	βa (V/dec)	βc (V/dec)	I corr (μA)	Rp (Ω.)	CR (mm/yr)
0.1 wt % Ru	0.1	0.1	3.97E+01	547.99	0.41
0.5 wt % Ru	0.1	0.1	7.76E+02	28.00	7.97
1 wt % Ru	0.1	0.1	9.37E+02	23.20	9.61
2 wt % Ru	0.1	0.1	1.11E+03	19.54	11.41

According to linear polarization the corrosion rate increased as Ru was added from 0.1 wt% to 0.5 wt% Ru. Corrosion rate further increased at 1 wt% Ru compared to the 0.5 wt% Ru. At 2 wt% Ru addition the corrosion rate increased compared to the 1 wt% Ru addition. The Tafel extrapolation data offered more accurate data in this study. Ruthenium reduces the overvoltage of cathodic hydrogen generation thereby increasing the efficiency of the cathodic process. Studies by Tomashov found that Ru possessed better general and pitting corrosion resistance when compared to other PGMs such as Pd due to the ability of Ru to reduce overvoltage of the cathodic hydrogen generation (Tomashov, 1896). However, as more Ru was added into the weld metal of LDX 2101 the corrosion rate increased.

4.6 Pitting Corrosion results

The pitting susceptibility of the LDX 2101 DSS was analysed using an optical microscope. Figure 55 to Figure 58 show the impact Ru addition to LDX 2101 has to the pitting corrosion susceptibility.

The pitting resistance equivalent (PREN) for LDX 2101 was 26. Figure 55 shows the micrograph for 0.1 wt% Ru addition to LDX 2101 button welds after potentiodynamic polarization tests using 1 M NaCl.

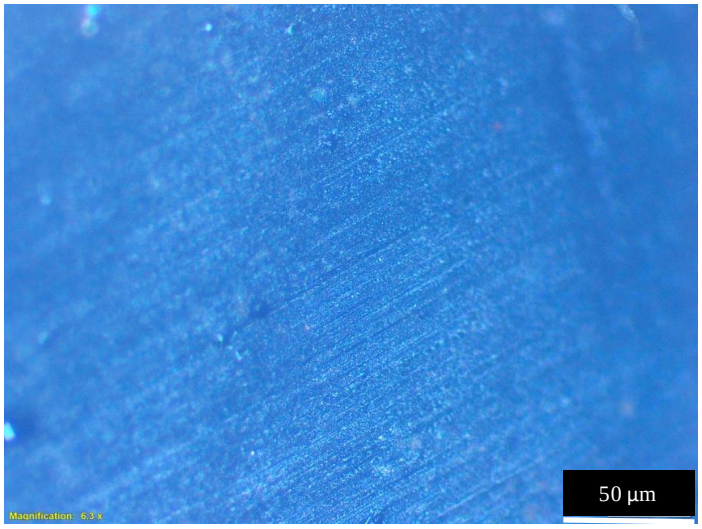


Figure 55: Surface of the 0.1 wt% Ru LDX 2101 corroded sample after potentiodynamic polarisation in 1 M NaCl.

The micrograph Figure 55 for 0.1 wt% Ru did not show any signs of pitting corrosion. The nitrogen concentration in the austenite phase decreased with temperature as the volume fraction of austenite increases. This lead to increasing pitting corrosion resistance for the LDX 2101 Figure 56 shows the micrograph of the 0.5 wt% Ru addition to LDX 2101.

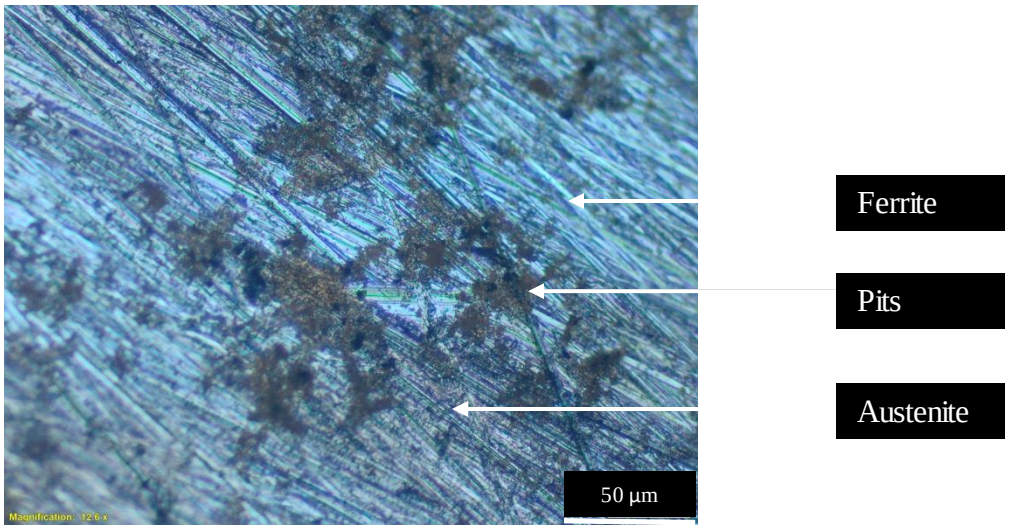


Figure 56: Surface of the 0.5 wt% Ru LDX 2101 corroded sample after potentiodynamic polarisation in 1 M NaCl.

The increase in Ru seems to have triggered corrosion on the sample. Figure 57 shows the corrode sample with 1 wt% Ru addition to the LDX 2101.

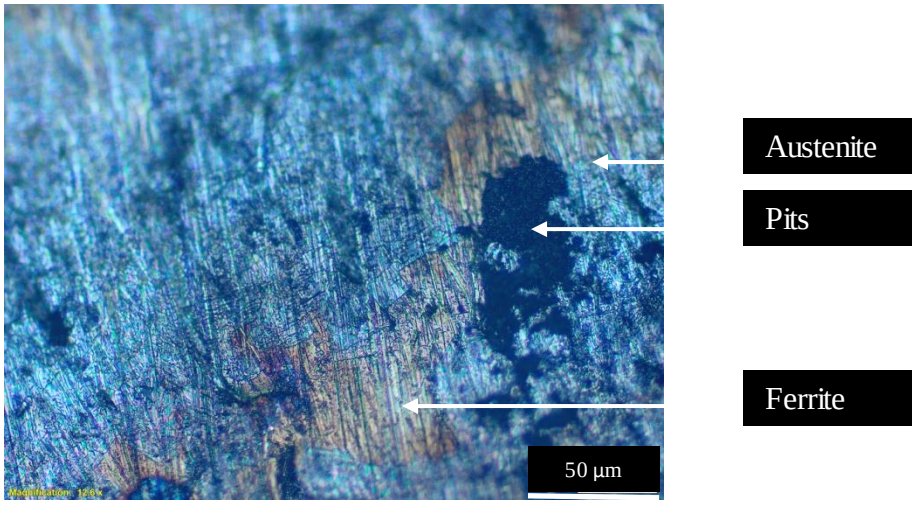


Figure 57: Surface of the 1 wt% Ru LDX 2101 corroded sample after potentiodynamic polarisation in 1 M NaCl.

The corrosion resistance of duplex stainless steel depends mostly on the composition. For chloride pitting and crevice corrosion resistance, the Cr, Mo and N contents are most important. The increase in Ru addition and the post weld heat treatment saw the austenite phase gain prominence in the microstructure at 2 wt% Ru as shown in Figure 58.

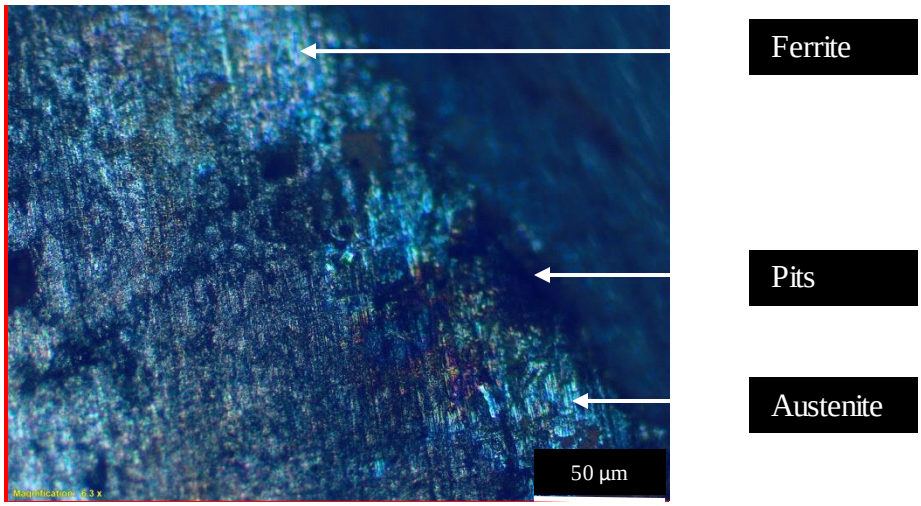


Figure 58: Surface of the 2 wt% Ru LDX 2101 corroded sample after potentiodynamic polarisation in 1 M NaCl.

Generally, the occurrence of pitting corrosion is indicated by an increased current of the alloy with time. The passivated oxide layers on this steel contain ruthenium as well as chromium. Therefore, the resistance of the steel to the activating effect of chloride ions increases; thus, Ru does not impair the resistance to pitting corrosion. This agreed with the microstructures, because there was not much pitting observed microstructurally on the LDX 2101 alloys with ruthenium after the corrosion tests.

4.7 Comparison of 316L vs LDX 2101 corrosion properties

The comparative look at the potentiodynamic polarisation curves of 316L vs LDX 2101 stainless steel is shown in Figure 59. For industrial application the benefits of Ru addition either to 316L or LDX 2101 need to be understood. The alloy wt% that gave most favourable performance in terms of corrosion rate and pitting corrosion was chosen for both 316L and LDX 2101 to be 1 wt% Ru addition.

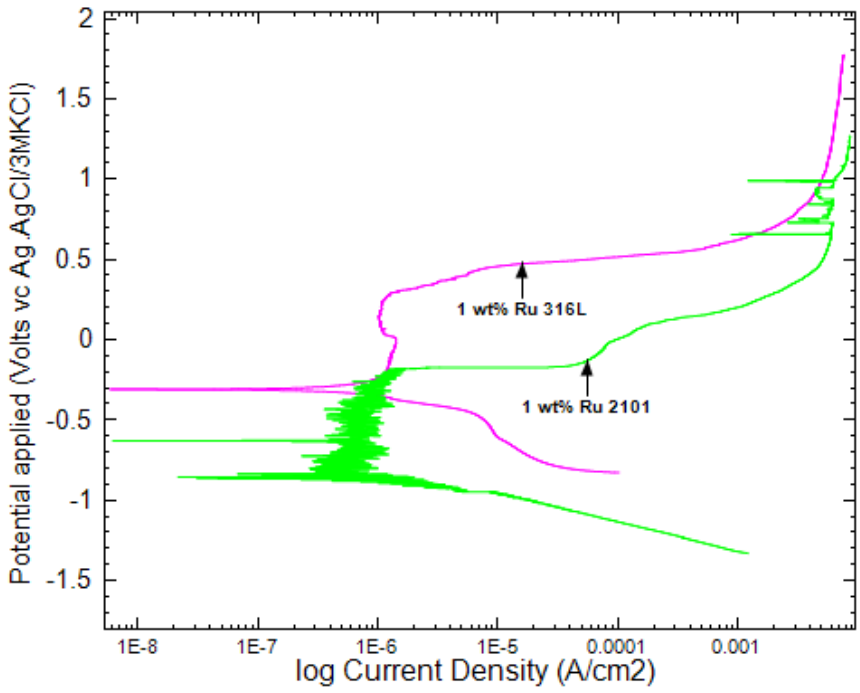


Figure 59: Comparative potentiodynamic polarisation curve for 1 wt% Ru addition to 316L ASS verse LDX 2101 DSS.

From the 1 wt% curves a comparative analysis was done the corrosion resistance of 316L ASS was gathered to be better than LDX 2101 DSS. Figure 60 shows the corrosion comparison of 316L and LDX 2101.

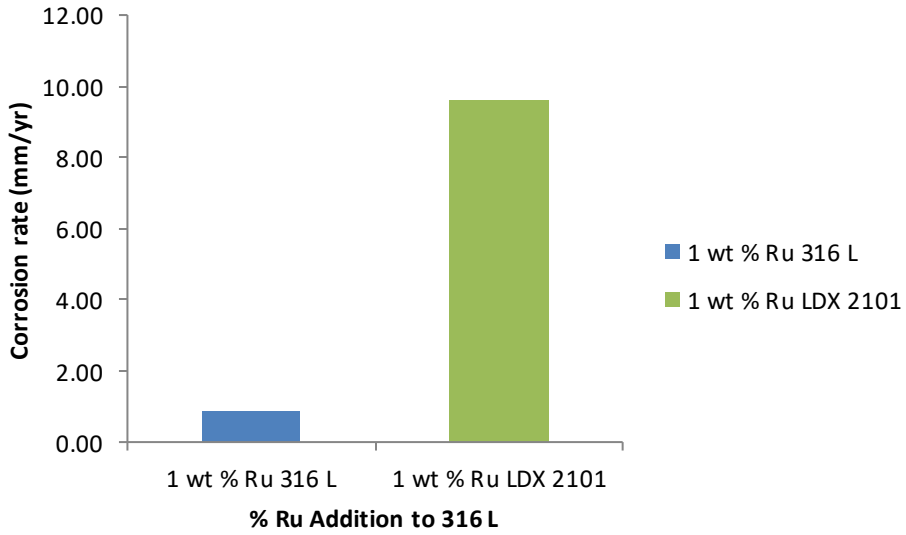


Figure 60: Corrosion rate comparison in mm/yr for 316L ASS and LDX 2101.

From the corrosion data in Figure 60 it was observed that 316L with 1 wt% Ru addition exhibited superior corrosion resistance capabilities. 316L ASS had nitrogen contents of 0.052 wt% while LDX 2101 had nitrogen contents of 0.3 wt%. Nitrogen additions to austenitic and duplex stainless steels improve pitting resistance and retard the kinetics of sigma phase formation. However, the 316L showed more positive potential values and a higher E_{corr} and i_{corr} value whereas LDX 2101 showed more negative E_{corr} values.

5 Commercial viability

In order to consider the commercial viability of adding Ru to the weld metal of 316L ASS versus LDX 2101 DSS, the following critical factors need to be taken into consideration:

- Corrosion resistance,
- metallurgical stability at the operating temperature,
- strength - This influences thickness & weight, and
- cost of the metal.

This also includes looking at other mechanical properties such as fabrication and welding. Not forgetting the physical properties and overall appearance of the material depending on the application. Other factors include; tooling costs, life cycle costs, and availability which takes into consideration the confidence in suppliers. Lastly the recyclability and environmental impacts of that materials production and use need to considered.

Duplex stainless steels have lower nickel and molybdenum contents than their austenitic counterparts of similar corrosion resistance. Compared to austenitic stainless steel, duplex stainless steels can be less expensive, which is usually because of the lower nickel contents. It may often be possible to reduce the section thickness of duplex stainless steel, compared to austenitic stainless steel, because of its higher yield strength. The combination of lower nickel content and reduction of thickness of duplex stainless steel can lead to significant cost and weight savings compared to austenitic stainless steels. LDX 2101 unlike most duplex grades can be machined and can be worked with even greater ease than 316L. However, it is important to note that, stainless steels are good forming materials, but duplex grades tend to require higher forming forces than austenitic grades do, especially when cold forming. Due to the increased hardness of DSS, they generally provide machining challenges. High amounts of Ru addition result in an uneconomical solution to corrosion resistance and therefore an acceptable amount of Ru addition

such as 1 wt% Ru can be considered. This percentage of Ru addition would give desirable mechanical properties, microstructural and corrosion properties according to this study.

6 Conclusions

Ru addition to 316L and LDX 2101 weld metal improved the microstructural morphology of the 316L and LDX 2101 respectively. The Ru was evenly distributed throughout the microstructure, and as the Ru content increased grain refining occurred. The mode of solidification was classified as FA mode for 316L and F mode for LDX 2101. Subsequently, the hardness of the alloyed 316L was increased to values of 198 HV versus 152 HV for the standard material. Similarly, LDX 2101 hardness increased to 235 HV compared to the as-received material at 223 HV. Microstructurally sigma phase was not identified experimentally for LDX 2101. Nitrogen has a prominent effect on the formation of ferrite in the LDX 2101, as the dissolution of austenite occurs primarily via the diffusion of nitrogen. Nitrogen additions to austenitic and duplex stainless steels improve pitting resistance and retard the kinetics of sigma phase formation. After GTAW the LDX 2101 microstructure was non-homogenous with increased ferrite region compared to austenite. There was therefore need for a post weld heat treatment on the alloys to produce a 50:50 austenite: ferrite ratio. Heat treating at 1050°C resulted in austenite increasing and a homogenous 50:50 phase distribution. Corrosion resistance in this study was evaluated at ambient temperature and indicated that as Ru addition increased there was an increase in corrosion resistance. This optimum was found to be 1 wt% Ru addition; thereafter 2 wt% exhibited a decline in corrosion resistance. This was due to the spontaneous passivation of the samples caused by 1 wt% Ru addition. Ruthenium additions increased the corrosion potential to more active values in all the solutions. The pitting corrosion micrographs validated that the optimum Ru percentage to add into a GTAW was 1 wt%, to ensure successful weld application. Overall cathodic modification of stainless steels with minor alloying additions of noble metals has proved to be an effective approach to improving their corrosion resistance in a NaCl environment. However, when more than 1 wt% Ru is added there can be a shift to more positive current density values and a lowering in the corrosion potential thus promoting the cathodic reaction. Ruthenium reduces the rate of anodic dissolution by reducing the critical current density required for passivation especially in media containing chlorides.

7 Recommendations

- Analysis of solutions post corrosion tests to evaluate the metal weight deposited in corrosive solution.
- TEM and WDS for analysing small ruthenium proportions.
- Post welds surface analysis using XPS to determine the composition.

8 References

Kou, S., 2002. Welding Metallurgy. 2nd ed. Hoboken, New Jersey: John Wiley & Sons, Inc..

Lekala, M., van der Merwe, J. & Pitya, S., 2012. Laser Surface Alloying of 316L Stainless Steel with Ru and Ni mixtures. International Journal of Corrosion, pp. 1-4.

Lippold, J. & Frankel , G., 2009. Development of Chromium-Free Welding Consumables for Stainless steels, Ohio: Department of Defense Strategic Environmental Research and Development Program (SERDP).

Adenike, O., 2014. Heat and corrosion behavior of 2101duplex stainless steelcathodically modified with ruthenium. [Online] Available at: wiredspace.wits.ac.za/ [Accessed 2016 February 05].

Alfonsson, E., 2010. Lean duplex- the first decade of service experience. Outokumpu Stainless AB, Issue 4, p. 17.

Alvarez-Armas, I., 2008. Duplex Stainless Steels: Brief History and Some Recent Alloys. Recent Patents on Mechanical Engineering, 1(1), pp. 51-52.

Amri, J., 2009. On Growth and Stifling of Localized Corrosion Attacks in CO2 and Acetic Acid Environments Application to the Top-of-Line Corrosion of Wet Gas Pipelines Operated in Stratified Flow Regime. Génie des procédés. Institut National Polytechnique de Grenoble-INPG,.

Asaduzzanman, M., Mustafa, C. M. & Islam, M., 2011. Effects of concerntration of sodium chloride solution on the pitting corrosion behaviour of AISI-304L austenitic stainless steel. Chemical Industry & Chemical Engineering Quarterly 1, 17(4), p. 477−483.

ASM International, 2006. Basic on the Corrosion of Stainless Steel Weldments. In: J. D. &. associates, ed. Corrosion of Weldments. United States of America: ASM International, pp. 3-7.

ASTM International, 2014. ASTM E290-14. In: www.astm.org, ed. Standard Test Methods for Bend Testing of Material for Ductility. PA: West Conshohocken, p. 3.

ASTM International, 2015. Stadard Test Methods for Tension Testing of Metallic Materials. In: www.astm.org, ed. ASTM E8/E8M-15a. PA: West Conshohoken.

Aung, M., 2016. Phase transformation (Material Science). [Online] Available at: https://www.slideshare.net/MyozinaungMza/phase-transformation-material-science [Accessed 24 March 2018].

AZoM, 2013. Azo Materials: Ruthenium (Ru) - Properties, Applications. [Online] Available at: https://www.azom.com [Accessed 1 2 2018].

Baldissin, D., Baricco, M. & Battezzati, L., 2007. Microstructures in rapidly solidified AISI 304 interpreted according to phase selection theory. Materials Science and Engineering A, Volume 999-1002, pp. 449-451.

Banda, S. K. & Van der Merwe, J., 2014. Effect of small additions of ruthenium on pitting corrosion resistance of LDX 2101 duplex stailess steel. Corrosion 32 Engineering, Science and Technology, 49(1), p. 1.

Bockris, J. & Reddy, A., 1973. In: Modern Electrochemistry, vol 2. New York, NY: Plenum Publishing Corporation, pp. 845-1163.

Bockris, J. & Reddy, A., 1973. In: Modern Electrochemistry, vol 2. New York, NY: Plenum Publishing Corporation, pp. 845-1163.

Borland, J., 1960. Generalized theory of super-solidus cracking in welds (and castings). British Welding Journal, Volume 7, p. 508–512.

British stainless steel association, 2016. The Schaeffler and Delong diagrams for predicting ferrite levels in austenitic stainless steel welds. [Online] Available at: http://www.bssa.org.uk/ [Accessed 12 August 2016].

Brooks, J., Baskes, M. & and F.A. Greulich, 1991. Solidification and solid state transformationin high energy density stainless steel welds. Metallurgical and Materials Transactions A, Volume 22, p. 915–926.

Brytan, Z. & Niagaj, J., 2016 . Corrosion resistance and mechanical properties of TIG and A-TIG welded joints of lean duplex stainless steel S82441 / 1.4662. Arch. Metall. Mater., 61(2), p. 771–784.

BSSA, 2016. The Schaeffler and Delong diagrams for predicting ferrite levels in austenitic stainless steel welds. [Online] Available at: http://www.bssa.org.uk/ [Accessed 12 August 2016].

Chernova, G., Tomashov, N. & Chigiran, L., 1978. The Effect of Alloying on the Passivation of Iron--Chromium-Based Alloys. Corrosion -The Jornal of Science and Engineering, 34(12), pp. 445-446.

Collins, S., 1997. Stainless Steel for semiconductor Applications. 39th Mechanical Working and steel processing Conference of the Iron and steel Society 1998, Indianapolis, Volume 19-22, pp. 607-619.

David, S. & Vitek, T., 1993. Principles of Weld Solidification and Microstructures. International Trends in Welding Science and Technology, pp. 147-157.

Davis, J., 1994. ASM Specialty Handbook: Stainless Steels. Ohio: Davis & Associates: Chagrin Falls.

Dawson, J. L. & Ferreira, M. G. S., 1986. Crevice corrosion of 316 stainless steel in 3% sodium chloride solution. Corrosion Science, 26(12), pp. 127-1040.

DeLong, W. T., 1973. Ferrite in Austenitic Stainless Steel Weld Metal. Welding Journal, 57(7), pp. 193s-203s.

Desu, R. K. et al., 2014. Mechanical properties of Austenitic Stainless Steel 304L and 316L at elevated temperatures, India: Journal of Materials Research and Technology.

Devletian, J. & Wood.W., 1983. Principles ofJoining Metallurgy. Metals Handbook, Volume 6, pp. 22-49.

Duru, A., 2011. Seagate Not Likely to Find 'Ruthenium-Like' Relief From Soaring Rare Earth Prices. Seagate Technology (STX), 28 July, p. 1.

Fandem.Q.A, 2017. Deterioration of Stainless Steel Corrosion Resistance Due to Welding. Journal of Material Sciences & Engineering , Volume 6, p. 2.

Folkard, E., 1988. Welding Metallurgy of Stainless Steels. Wien: Springer.

Frankel, G., 2016. Fundamentals of Corrosion Kinetics, Columbus: The Ohio State University.

Garner, A., 1979. Corrosion Journal, Houston,third ed. 35(3), p. 108-114.

Garner, A., 1982. Materials Performance,eight ed,, Volume 21, p. 9-14.

Gellings, P. & H.J.M. Bouwmeester (Eds.), H., 1997. In: The CRC Handbook of Solid State Electrochemistry. Boca Raton, FL: CRC Press, pp. 269–294, 407–480.

Grocki.J, 2012. A Primer for Duplex stainless steel, Portland: Arcelor Mital.

Gross, C. & Robinson, F., 1981. Effect of the Addition of up to 18% Manganese on the Microstructure and Corrosion Properties of a 14.5% Chromium Stainless Steel. Metallic Corrosion, Proceedings-31st International Congress on Metallic Corrosion, South Africa, Volume 1, p. 114.

Gunn & R.N., 1997. Duplex Stainless Steels: Microstructure, Properties and Applications. England: Elviser: Technology & Engineering.

Hampel, C., 1954. Rare Metals Handbook. New York, NY, USA : s.n.

Haugan, E. et al., 2017. Effect of Tungsten on the Pitting and Crevice Corrosion Resistance of Type 25Cr Super Duplex Stainless Steels. Corrosion, 73(1), pp. 53-67.

Hazza, M. & El-Dahshan, M., 1995. The effect of molybdenum on the corrosion behaviour of some steel alloys. Desalination, 95(2), pp. 199-209.

Hertzman, S. & Charles, J., 2011. On the effect of nitrogen on duplex stainless steels. Revue de Métallurgie, Volume 108, p. 413–425.

Higginson, A., 1989. Passivation of cathodically modified alloys. British Corrosion Journal, 24(4), pp. 297-302.

InfoMine Inc, I., 2017. Investment Mine. [Online] Available at: www.infomine.com [Accessed 26 Septemer 2015].

Inoue, H. & Koskei, T., 2007. Clarification of Solidification Behaviors in Austenitic Stainless Steels Based on Welding Process, Tokyo: Nippon steel technical report.

ISO, 2001 . Destructive tests on welds in metallic materials, Hardness testing -Part 1: Hardness test on arc welded joints. [Online] Available at: https://www.iso.org. ISBN. [Accessed 30 August 2016].

Jan, O. & Snis, M., 2006. Duplex – A New Generation of Stainless Steels for Desalination Plants. Outokumpu Stainless, Avesta Research Centre, 15 November.p. 1.

Jargelius-Pettersson, R., 1998. Application of the Pitting Resistance Equivalent Concept to Some Highly Alloyed Austenitic Stainless Steels. Corrosion engineering, 54(2), pp. 162-168.

Jones, D., 1996. Principles and Prevention of Corrosion. Prentice-Hall, Inc., U.S.A., Volume 75-80, pp. 143-153..

Junwei, F., Yang, Y. & Guo, a. J., 2009. Formation of a blocky ferrite in Fe–Cr–Ni alloy during directional solidification. Journal of Crystal Growth , China, 311(14), pp. 3661-3666.

K.A.Natarajan, K., 2012. National Programme in technology enhacned learning:Advances in corrosion engineering. [Online] Available at: nptel.ac.in/courses [Accessed 2018 February 5].

Klar, E. & Samal, P. K., 2007. Powder Metallurgy Stainless Steels: Processing, Microstructures, and Properties. 1st ed. Ohio: ASM International.

Korinko, P. & Malene, S., 2001. Considerations for the Weldability of Types 304L and 316L Stainless Steels, Aiken: Westinghouse Savannah River Company.

Kujanpaa, V., David, S. & White.C.L., 1986. Formation of Hot Cracks in Austenitic Stainless Steel Welds—Solidification Cracking. Welding Research Supplement, Oulu, Finland, pp. 204-212.

Liang, D. et al., 2010. Corrosion resistance of welds in type 304L stainless steel made with a nickel–copper–ruthenium welding consumable. Elsevier, p. 1.

Lippold, J. & Kotecki, D., 2005. Welding metallurgy and weldability of stainless steels. John Wiley and Sons Inc: Hoboken.

Long, C. J. & DeLong, W. T., 1973. The Ferrite Content of Austenitic Stainless Steel Weld Metal. SUPPLEMENT TO THE WELDING JOURNAL,, pp. 282-297.

Lula, R., 1986. Manganese Stainless Steels. The Manganese Centre, Issue 22.43, pp. 51-57.

M.Pellizzari, Frigo.M & M.Breda, 2005. σ-Phase in Lean Duplex Stainless Steel Sheets. Acta Metallurgica Sinica, 28(3), pp. 331-337.

Matthews, C., 2007. South Africa: The Rise of Ruthenium is Good News. Businees Day, 2 July, p. 1.

Metrohm Autolab B.V, M., 2011. Autolab Application Note COR02:Corrosion Part 2-Measurement of corrosion rates. [Online] Available at: www.ecochemie.nl/Applications/ [Accessed 5 January 2018].

Milada, M., Zreibaa, N., Elhalouanib, F. & Baradaib, C., 2007. The effect of cold work on structure and properties of AISI 304 stainless steel. Journal of Materials Processing Technology.

Mwamba, I. A., Cornish, L. A. & van der Lingen, E., 2014. Effect of platinum group metal addition on microstructure and corrosion behaviour of Ti–47.5 at-%Al, Pretoria, South Africa: University of Pretoria Institutional Repository.

Nana, S. & Cortie, M., 1993. Microstructure and corrosion resistance of experimental low-nickel duplex stainless steels. Journal of The South African Institute of Mining and Metallurgy, Volume 93, pp. 307-315.

Olaseinde, O., Cornish, L. & van der Merwe, J., 2015. Effect of Ruthenium addition on the phases of 2101 duplex stainless steel. International Journal of metallurgical engineering, 4(1), pp. 6-11.

Olson, D. L., 1985. Prediction of Austenitic Weld Metal Microstructure and Properties. WELDING RESEARCH SUPPLEMENT, pp. 281-295.

Outokumpu, 2014. LDX 2101® Comparative for Flat Rolled Products. [Online] Available at: http://www.outokumpu.com [Accessed 1 11 2017].

Papp .J.F., Fenton, C. E. D., Kuck, M., Magyar, M., 2007. Cr, Cu, Mn, Mo, Ni, and Steel Commodity Price Influences, Reston, VA, U.S: Geological Survey.

Parrott, R. & Pitts, H., 2011. Chloride stress corrosion cracking in austenitic stainless steel: Assessing susceptibility and structural integrity, Derbyshire: Crown.

Peckner, D. & Bernstein, I., 1977. Handbook of Stainless Steels. New York, NY: McGraw-Hill Book Company.

Pellizzari, Frigo.M & Breda, M., 2005. σ-Phase in Lean Duplex Stainless Steel Sheets. Acta Metallurgica Sinica, 28(3), pp. 331-337.

Perricone, M. et al., 2007. Effect of Composition on the Formation of Sigma during Single-Pass Welding of Mo-Bearing Stainless Steels. Metallurgical and Materials Transactions A. 38, Volume 9, pp. 1976-1900.

Pilhagen, J. & Sandström, R., 2014. Influence of nickel on the toughness of lean duplex stainless steel welds. Materials Science and Engineering: A, Volume 602, pp. 49-57.

Pitchkov, V. N., 1996. The Discovery of Ruthenium: “I NAMED THE NEW BODY, IN HONOUR OF MY MOTHERLAND”. Platinum Metals & Rev, 40(4), pp. 181-188 .

Potgieter, J., Ellis, P. & van Bennekom , A., 1995. Investigation of active dissolution behaviour of a 22 wt% chromium duplex stainless steel with small ruthenium additions in sulphuric acid. ISIJ International,vol.35, p. 197–202.

Potgieter, J., 1996. The effect of cathodic modifications on the corrosion behaviour of duplex stainless steels, University of Witwatersrand.

Potgieter, J., Heyns, A. & Skinner, W., 1990. Cathodic modification as a means of improving the corrosion resistance of alloys. Jornal of applied electrochemistry, Volume 20, pp. 711-715.

Potgieter, J., Olubambi, P. & Potgieter-Vermaak, S., 2014. The Corrosion behaviour of WC-Co-Ru alloys in aggressive chloride media. International Journal of Electrochemistry, p. 11.

Reidrich, G. & Loib, F., 1941. Archiv für das Eisenhüttenwesen. 15(7), pp. 175-182.

Rhines, F., 1968. Quantitative Microscopy. R.T. de Hoff and McGrawHill, ed. Boot Camp, New York, USA.: s.n.

Rockel, M. & Renner, M., 1984. Pitting, Crevice and stress corrosion resistance of high chromium and molybdenum alloy stainless steels. Materials and Corrosion,, 35(12), pp. 537-542.

Sahua, J., Kruppc, U., Ghosha, R. & Christ, H., 2009. Effect of 475 ◦C embrittlement on the mechanical properties of duplex stainless steel. Materials Science and Engineering A, Volume 508, pp. 1-14.

Salmon, C. G., 2014. Steel Structures. 5th ed. s.l.:Content technologies Inc.

Schaeffler, A. L., 1949. Construction Diagram for Stainless Steel Weld. Metals Progress, 56(5), pp. 680-680B.

Schutz, R., 2003. 2003 F.N. Speller Award Lecture: Platinum Group Metal Additions to Titanium: A Highly Effective Strategy for Enhancing Corrosion Resistance. Corrosion, 59(12), pp. 1043-1057.

Shankar, V., Gill, T., Mannan, S. & Sundaresan, S., 2003. Solidification cracking in austenitic stainless steel welds. Sadhana, Volume 28, p. 359–382.

Sherif, El-Sayed, M., Potgieter, J. & Comins, J., 2009. Effects of minor additions of ruthenium on the passivation of duplex stain-less-steel corrosion in concentrated hydrochloric acid solutions. Journal of Applied Electrochemistry , Volume 39, p. 1385–1392..

Shreir, L., 1963. Corrosion: Corrosion of metals and alloys. George Newnes Limited, London, Volume 1, pp. 1.16-1.66.

Siewert, T., C.N.McCowan & Olson, D., 1988. Ferrite number prediction to 100 FN in stainless steel weld metal. Welding Journal, Volume 37, p. 289s–298s.

Siewert, T. & Kotechi, D., 1992. WRC-1992 Constitution Diagram for Stainless Steel Weld Metals: A Modification of the WRC-1988 Diagram , Refined constitution diagram offers more accurate FN prediction for Cu-containing stainless steels and dissimilar metal joints. Welding Journal, Volume 71, p. 172s.

Solomon, H. & Devine, T., 1983. Duplex stainless steels-a tale of two phases. In: Duplex Stainless Steels Conference Proceedings. Lula, R.A. (ed.). Metals Park (USA), American Society for ed. Metals Park (USA): American Society for Metals, pp. 693-756.

Standard, N., 1994. Common requirements -Welding and Inspection of Piping. 1(M-CR-601), p. 3-5.

Statisca, 2017. Statista: Statistics portal. [Online] Available at: https://www.statista.com [Accessed 1 February 2018].

Struers, 2012. Hardness testing. Harndess testing news, 1(1), p. 2.

Suutala, N., 1983. Effect of solidification conditions on the solidification mode in austenitic stainless steel. Metallurgical and Materials Transactions, Issue 14A, p. 191-197.

Szklarska-Smialowska, Z., 1986. Pitting Corrosion of Metals. University of California: National Assn of Corrosion Engineers.

Tomashov, N., 1896. Prot. Met. 3 (1967). 22(3), p. 679.

Unnikrishnana, R., Satish Idury, K., Ismail, T. & Bhadouria, A., 2014. Effect of heat input on the microstructure, residual stresses and corrosion resistance of 304L austenitic stainless steel weldments. Materials Characterization, p. 1 0 – 2 3.

Van der Merwe, J. & Tharandt, D., 2015. Corrosion resistance of laser-cladded 304L stainless steel enriched with ruthenium additions exposed to sulphuric acid and sodium chloride media. The Journal of The Southern African Institute of Mining and Metallurgy, Volume 115, p. 1-2.

Varga, K. et al., 1997. Comparative study of surface properties of austenitic stainless steels in sulfuric and hydrochloric acid solutions. Electrochimica Acta, 42(1), pp. 25-35.

Vashisth, Y., 2015. Metal Inert Gas Welding. International Journal of Innovative Research in Technology, 2(7), p. 1.

Wahid, A., Olson, D., Matlock, D. & Cross, C., 1993. Corrosion Weldments. In: A. International, ed. Welding,Brazing and Soldering. Vol 6: ASM Handbook, pp. 1065-1069.

Wolff, I. M., 1999. New Applications for Ruthenium. Platinum in South Africa, 1 December, Issue 95, p. 539.

Wong, F., 2009. The effect of alloy compositionon the localised corrosion behaiviour of Ni-Cr-Mo alloys, Ohio: Ohio State University.

www.nsalloys.com, 2011. National Specialty Alloys, Inc.: 3 types of Stainless Steel. [Online] Available at: http://www.nsalloys.com/stainless-steel/3-types-of-stainless-steel.html [Accessed 15 January 2018].

Young.C.A., 2008. Autoclave technology. In: C. A. Young, ed. Hydrometallurgy 2008: Proceedings of the Sixth International Symposium.:SME, p. 1039.

Zanotto, F. & Zucchi, F., 2014. Stress corrosion cracking of LDX 2101 duplex stainless steel in chloride solutions in the presence of thiossulphae. Corrosion Science, Volume 80, p. 205-212.

9 Intellectual property

This projected is funded by the DST/NRF Centre of Excellence in Strong Materials and not funded by any industrial company. It is, therefore, expected that any invention, innovation and research results will be the sole property of the University of Witwatersrand.

10 Ethics

The research to be undertaken does not involve animal experimentation or human participants as defined in A.4 of the Senate Standing Orders on Higher degrees.

11 Appendix

11.1 Appendix A

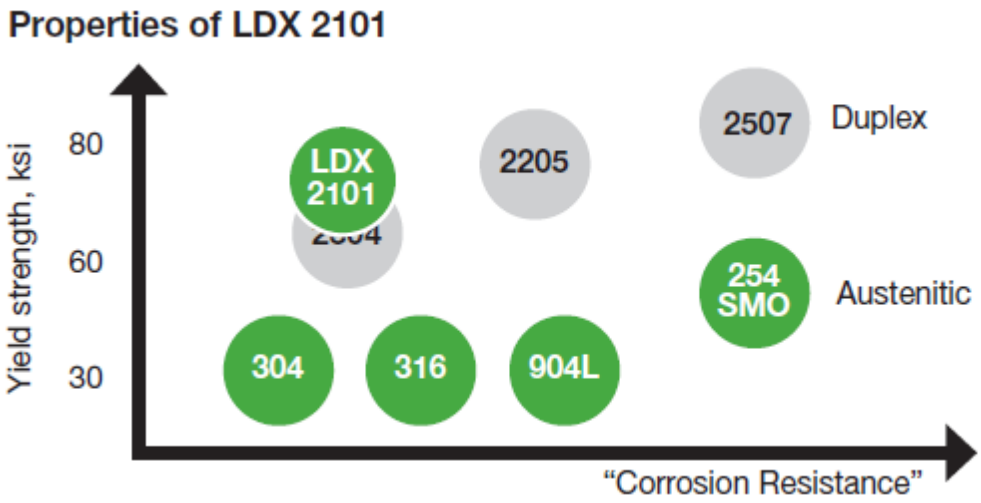


Figure 61: Mechanical properties vs Corrosion Resistance of LDX 2101 DSS compared to standard stainless steels (Outokumpu, 2014).

11.2 Appendix B

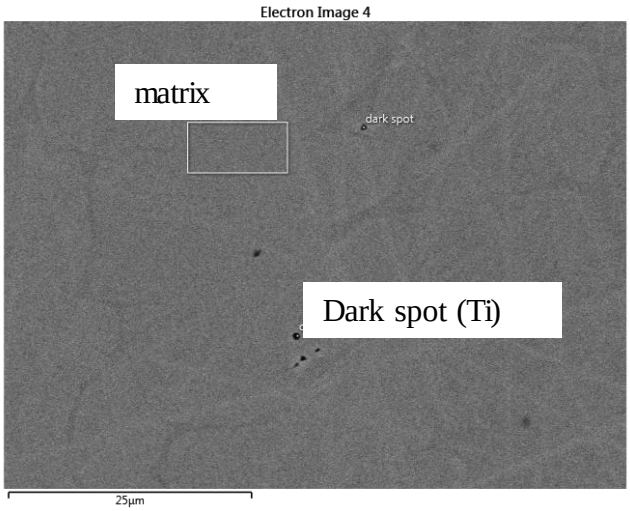


Figure 62: Back scattered image for EDX containing Ti.

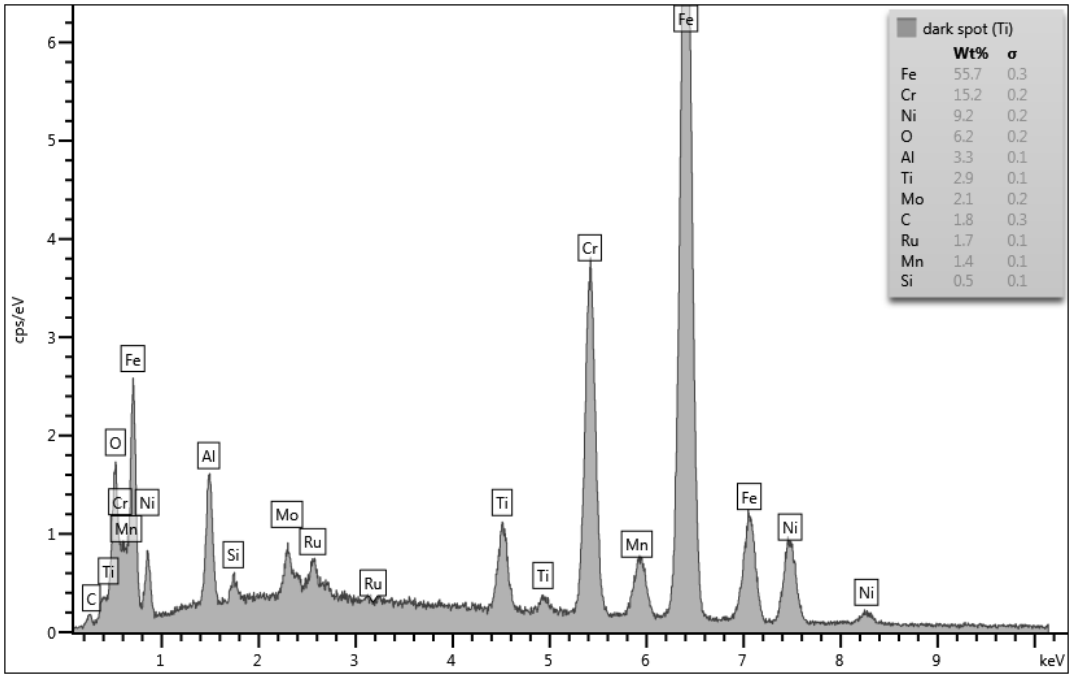


Figure 63: EDX analysis spectrum for 2 wt% Ru addition to 316L ASS.

11.3 Appendix C

EDX trends for 0.1 wt%, 0.5 wt%, 1 wt% and 2 wt% Ru addition to LDX 2101 DSS.

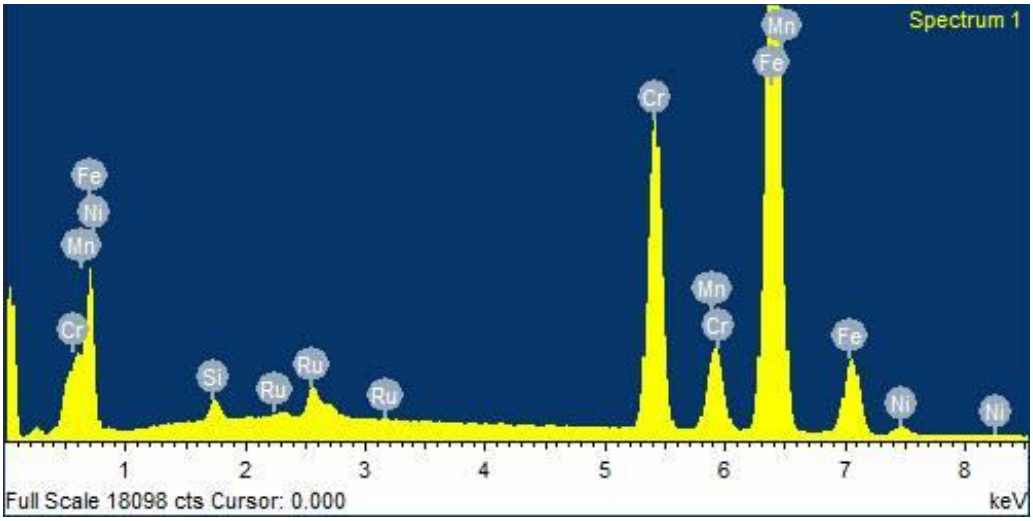


Figure 64 : EDX spectrum for 0.1 wt% Ru addition to LDX 2101.

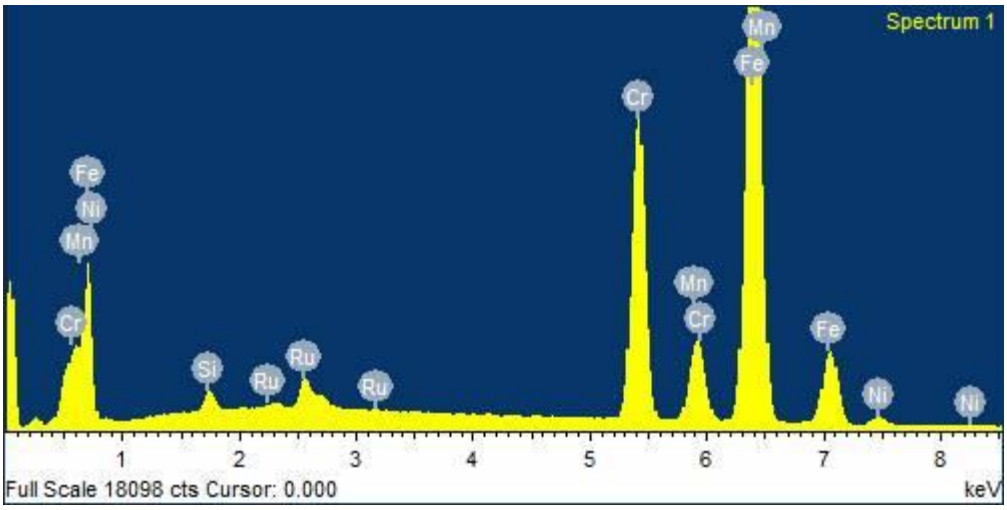


Figure 65 : EDX spectrum for 0.5 wt% Ru addition to LDX 2101.

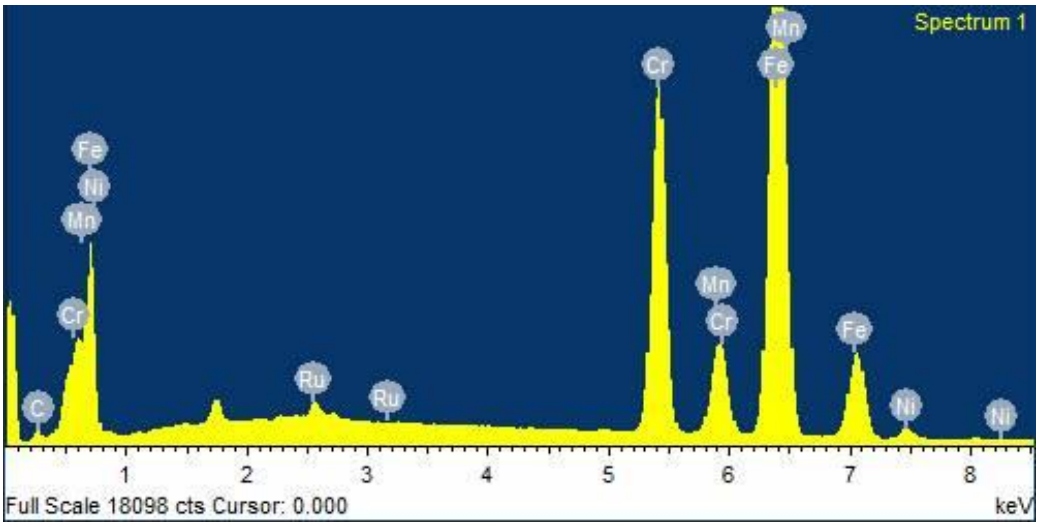


Figure 66: EDX spectrum for 1 wt% Ru addition to LDX 2101.

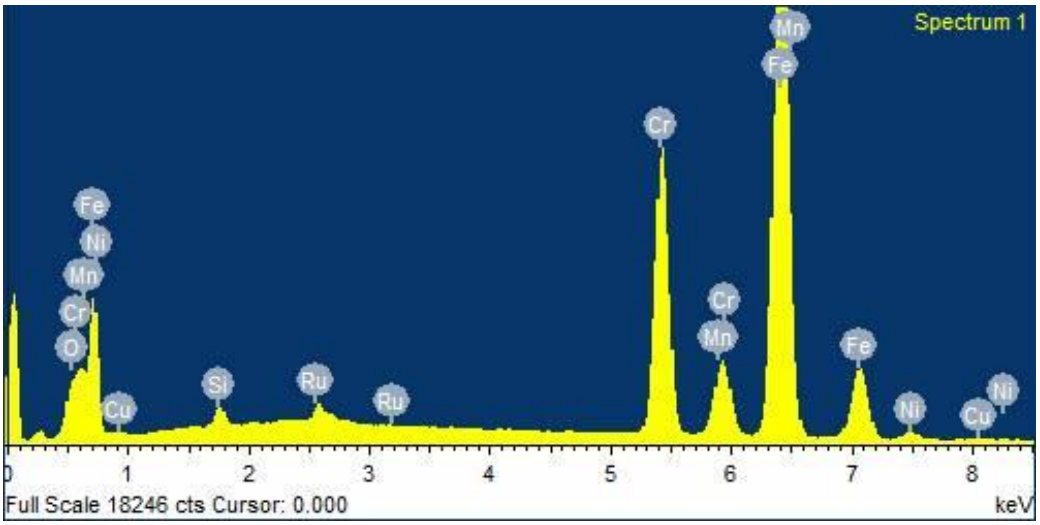


Figure 67: EDX spectrum for 2 wt% Ru addition to LDX 2101.

11.4 Appendix D

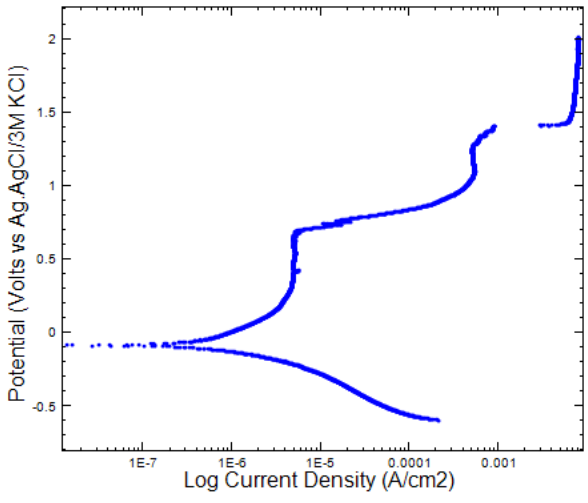


Figure 68: Potentiodynamic curves of 0.1 wt% Ru addition to 316L in 1M NaCl.

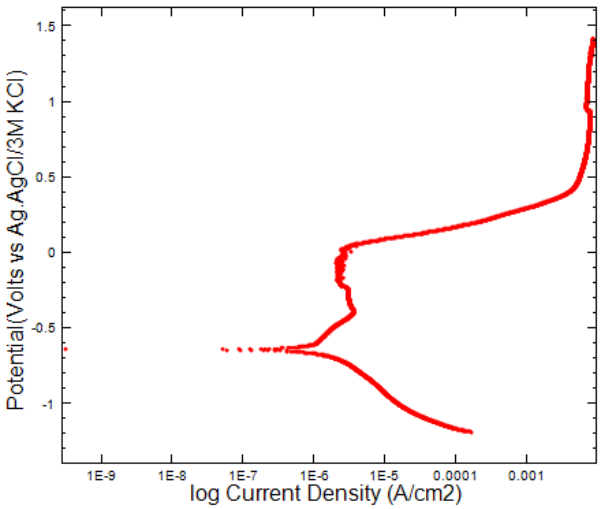


Figure 69: Potentiodynamic curves of 0.5 wt% Ru addition to 316L in 1M NaCl.

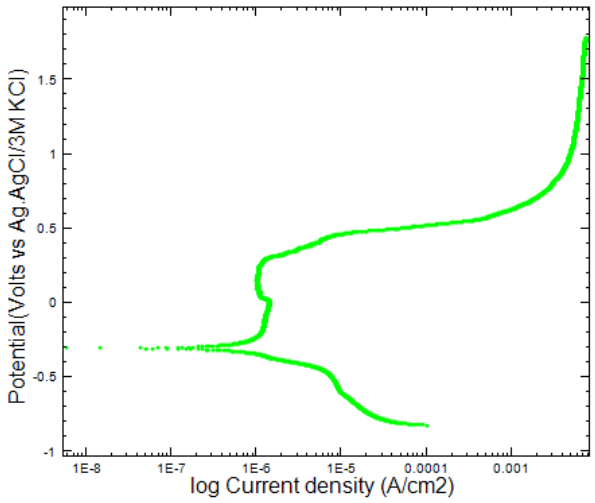


Figure 70: Potentiodynamic curves of 1 wt% Ru addition to 316L in 1M NaCl.

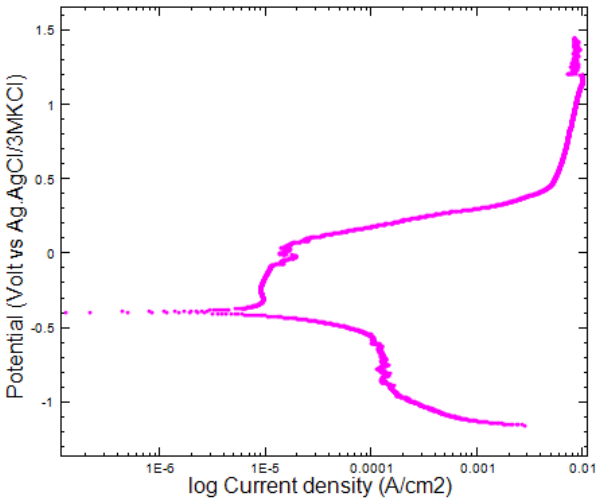


Figure 71: Potentiodynamic curves of 2 wt% Ru addition to 316L in 1M NaCl.

11.5 Appendix E

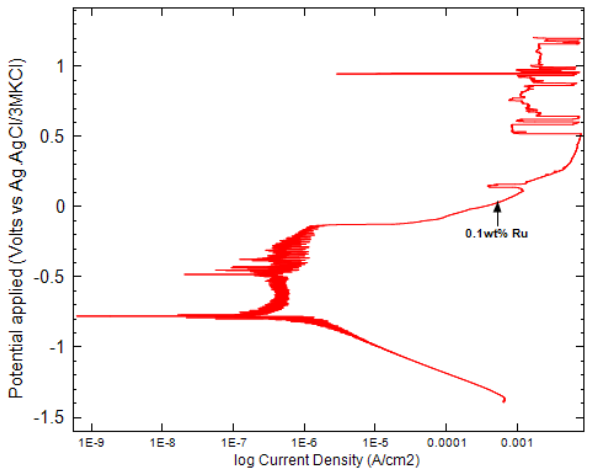


Figure 72: Potentiodynamic curves of 0.1 wt% Ru addition to LDX 2101 in 1M NaCl.

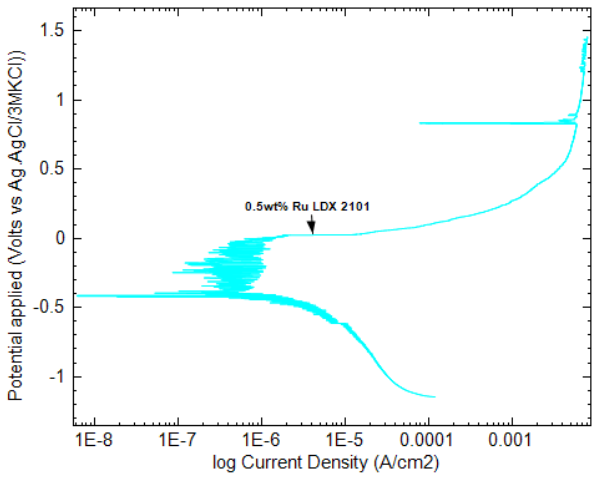


Figure 73: Potentiodynamic curves of 0.5 wt% Ru addition to LDX 2101 in 1M NaCl.

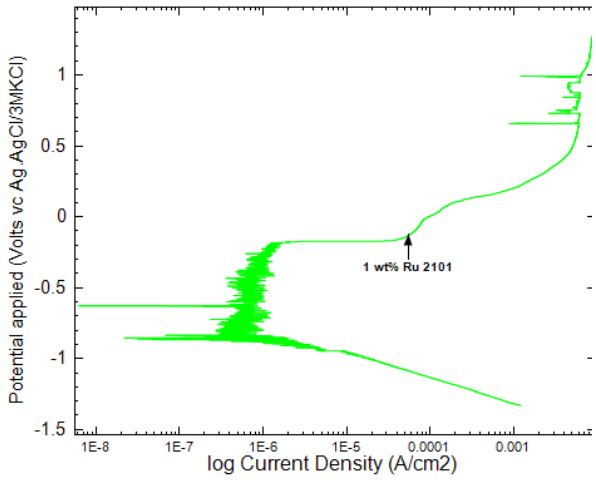


Figure 74: Potentiodynamic curves of 1 wt% Ru addition to LDX 2101 in 1M NaCl.

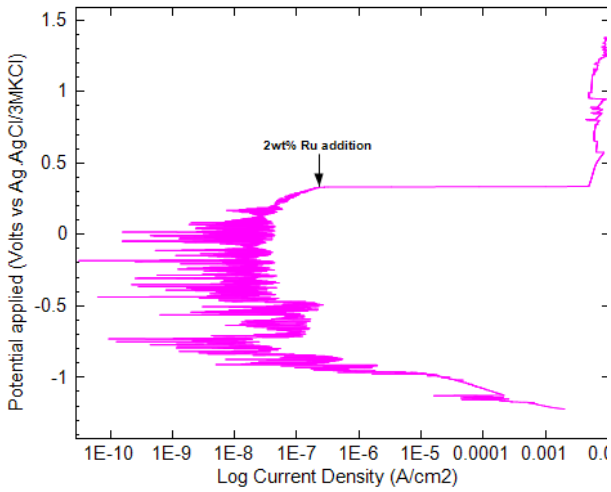


Figure 75: Potentiodynamic curves of 2 wt% Ru addition to LDX 2101 in 1M NaCl.

11.6 Appendix F

The Tafel extrapolation graphs used to calculate corrosion rate (mm/yr) for 0.1 wt%, 0.5 wt%, 1 wt% and 2 wt% Ru addition to 316 L ASS.

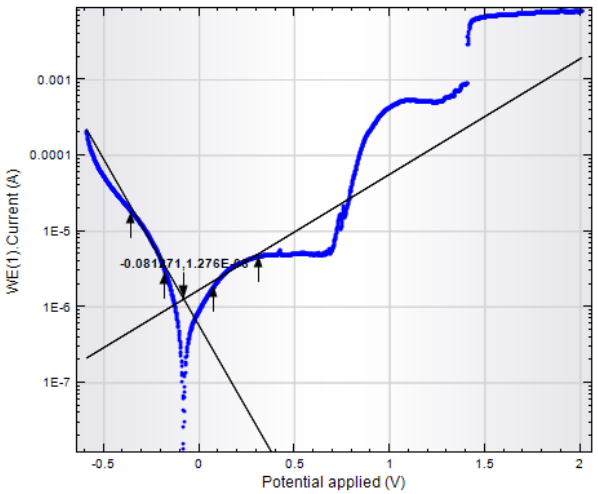


Figure 76: Tafel extrapolation of 0.1 wt% Ru addition to 316L in 1M NaCl.

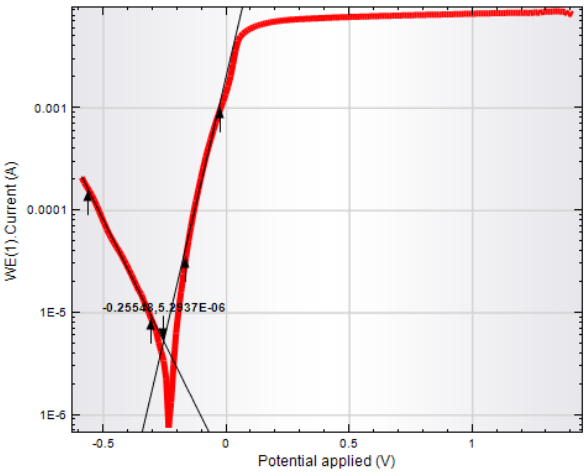


Figure 77: Tafel extrapolation of 0.5 wt% Ru addition to 316L in 1M NaCl.

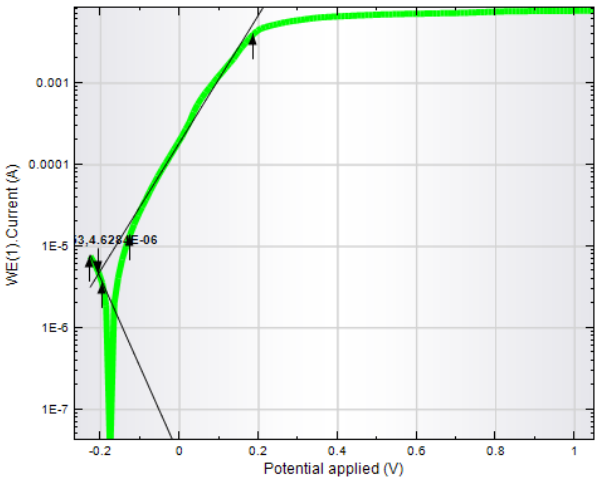


Figure 78: Tafel extrapolation of 1 wt% Ru addition to 316L in 1M NaCl.

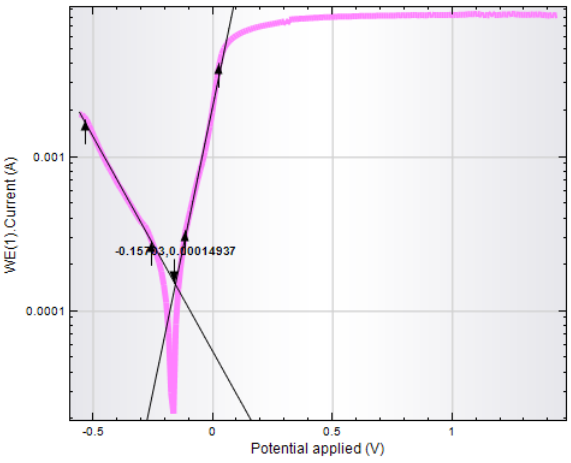


Figure 79: Tafel extrapolation of 2 wt% Ru addition to 316L in 1M NaCl.

11.7 Appendix G

The Tafel extrapolation graphs used to calculate corrosion rate (mm/yr) for 0.1 wt%, 0.5 wt%, 1 wt% and 2 wt% Ru addition to LDX 2101 DSS.

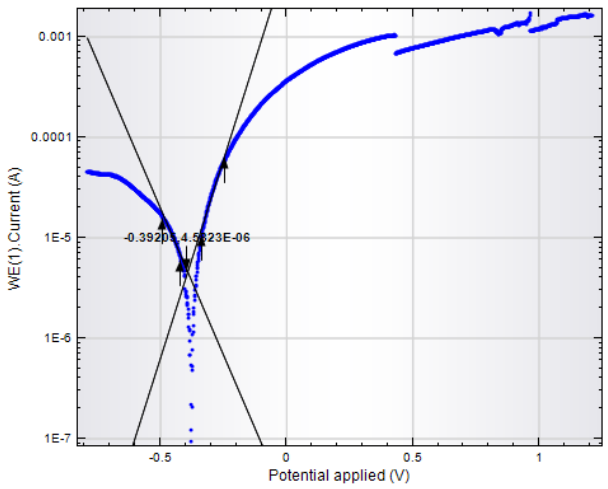


Figure 80: Tafel extrapolation of 0.1 wt% Ru addition to LDX 2101 in 1M NaCl.

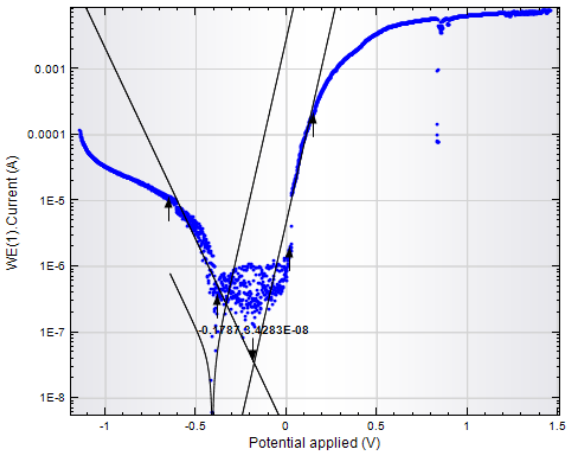
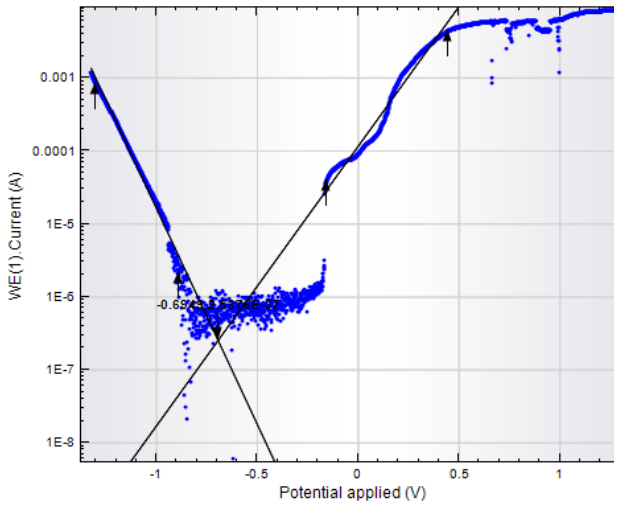


Figure 81: Tafel extrapolation of 0.5 wt% Ru addition to LDX 2101 in 1M NaCl.



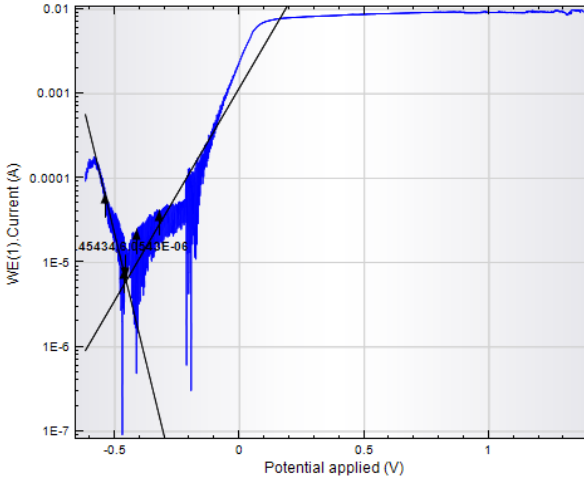
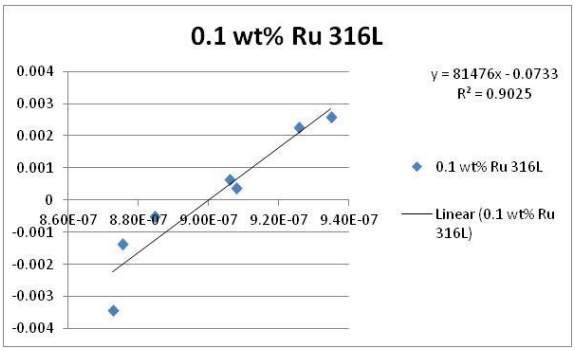


Figure 82: Tafel extrapolation of 1 wt% Ru addition to LDX 2101 in 1M NaCl.

Figure 83: Tafel extrapolation of 2 wt% Ru addition to LDX 2101 in 1M NaCl.

11.8 Appendix H

The linear polarization graphs used to calculate corrosion rate (mm/yr) for 0.1wt%, 0.5wt%, and 1 wt% and 2wt% Ru addition to 316 L ASS.



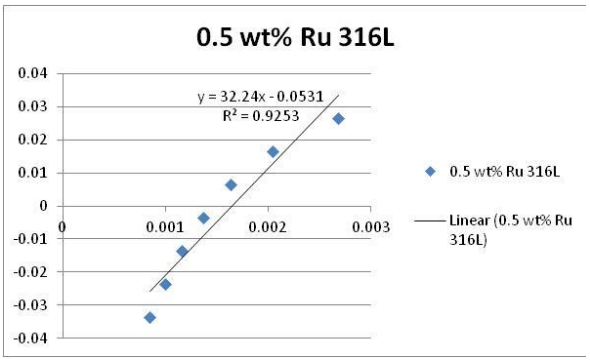
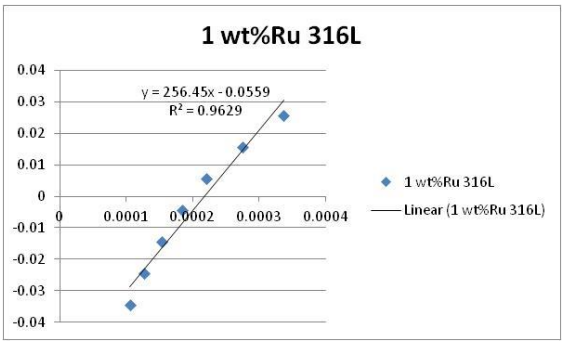


Figure 84: Linear polarisation resistance of 0.1 wt% Ru addition to 316L in 1M NaCl.

Figure 85: Linear polarisation resistance of 0.5 wt% Ru addition to 316L in 1M NaCl.



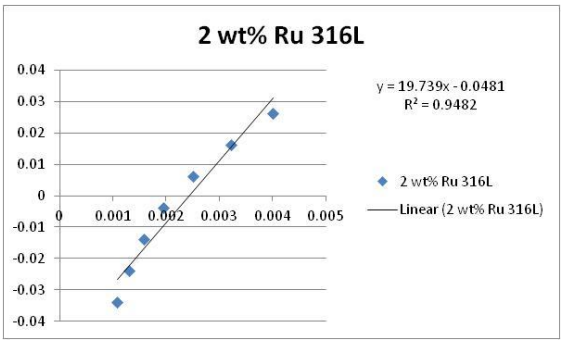


Figure 86: Linear polarisation resistance of 1 wt% Ru addition to 316L in 1M NaCl.

Figure 87: Linear polarisation resistance of 2 wt% Ru addition to 316L in 1M NaCl.

11.9 Appendix I

The linear polarisation resistance graphs used to calculate corrosion rate (mm/yr) for 0.1 wt%, 0.5 wt%, 1 wt% and 2 wt% Ru addition to LDX 2101 DSS.

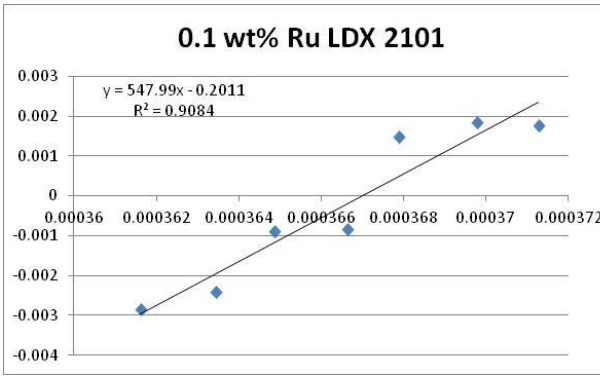


Figure 88: Linear polarisation resistance of 0.1 wt% Ru addition to LDX 2101 in 1M NaCl.

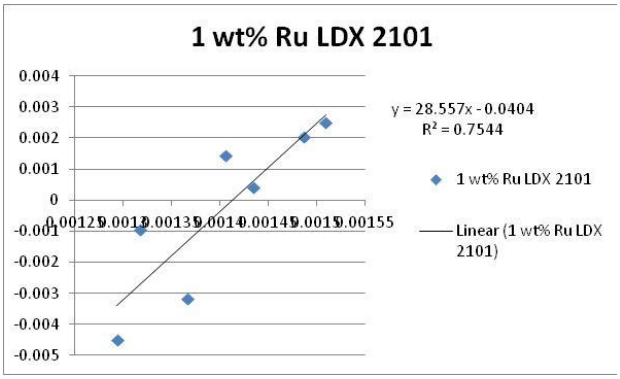


Figure 89: Linear polarisation resistance of 0.5 wt% Ru addition to LDX 2101 in 1M NaCl.

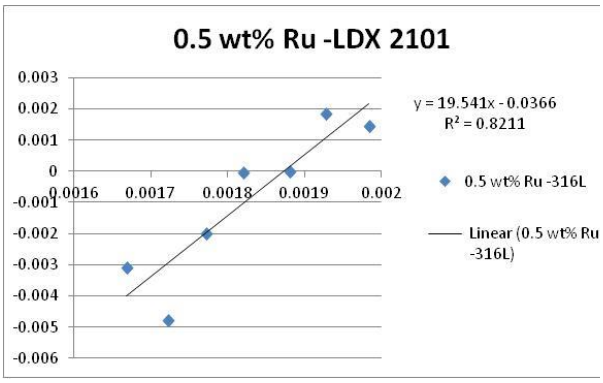


Figure 90: Linear polarisation resistance of 1 wt% Ru addition to LDX 2101 in 1M NaCl.

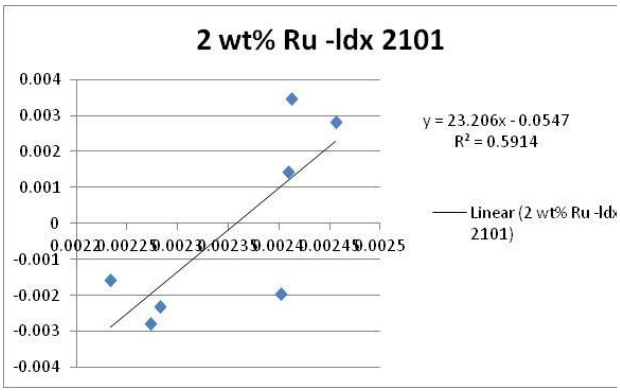


Figure 91: Linear polarisation resistance of 2 wt% Ru addition to LDX 2101 in 1M NaCl.

11.10 Appendix J

11.10.1 Publication from this work

Papers published during the course of this paper, using this work

1) B.N.Zuma and J.W.van der Merwe, 2017. Effect of Ru Addition on the Mechanical Properties and Microstructure of 316L Austenitic Stainless Steel Weld Metal. Procedia Manufacturing, 7, p. 2-7.

Presentations from this work

B.N.Zuma and J.W.van der Merwe. "Effect of Ru Addition on the Mechanical Properties and Microstructure of 316L Austenitic Stainless Steel Weld Metal.", International Conference on Sustainable Materials Processing and Manufacturing, SMPM 2017, Kruger National Park, 23-25 January 2017.

B.N.Zuma and J.W.van der Merwe, "Effect of Ru Addition on the Mechanical Properties and Microstructure of 316L Austenitic Stainless Steel Weld Metal.", SAIMM : 3rd Young professionals conference , Innovation hub, Pretoria, 9–10 March 2017.

B.N.Zuma and J.W.van der Merwe. "Effect of ruthenium additions on the metallographic properties and corrosion of the weld metal of 316l stainless steels.", Microscopy society of Southern Africa Conference 2016, Boardwalk Convention Centre, Port Elizabeth, 5-6 December 2016.

International Presentations

B.N.Zuma and J.W.van der Merwe. "Effect of ruthenium additions on the corrosion and mechanical properties of the weld metal of 316L stainless steels", European Congress and exhibition on advanced Materials and processes, Greece, Thessaloniki, 11-22 September 2017.

Prizes won:

A. Top 3 at Institute of Materials, Minerals and Mining, Southern Africa (IOM3) Annual Young Persons' Lecture Competition Regional's
B. 3rd Place at IOM3 Nationals in Port Elizabeth
C. Second place in University of Witwatersrand Metallurgy Departmental Postgraduate Poster presentation day

Available online at www.sciencedirect.com

ScienceDirect

Procedia Manufacturing 00 (2016) 000–000

Procedia MANUFACTURING

www.elsevier.com/locate/procedia

International Conference on Sustainable Materials Processing and Manufacturing, SMPM 2017, 23-25 January 2017, Kruger National Park

Effect of Ru addition on the mechanical properties and microstructure of 316L austenitic stainless steel weld metal.

B.N. Zuma[a, b] and J.W. van der Merwe[a,b,c,1]

[a]School of Chemical and Metallurgical Engineering, University of the Witwatersrand, Johannesburg, South Africa,

[b]DST-NRF Centre of Excellence in Strong Materials, University of the Witwatersrand,

[c]African Materials Science and Engineering Network

Abstract

The addition of Ru to the weld metal of 316L austenitic stainless steel (ASS) by Gas tungsten arc welding (GTAW) button welds has shown superior mechanical properties. In the present investigation, the effect of Ru additions on the physical properties of 316L weld was evaluated by investigating the microstructural and mechanical properties of weld metal. The microstructure and mechanical properties of the alloyed button welds were analyzed using optical microscope, scanning electron microscopy (SEM), EDX and Vickers hardness test respectively at 0.1%, 0.5%, 1% and 2% Ru addition. Primary ferrite (FA mode) solidification resulted in primary δ-ferrite and eutectic γ-austenite in the button welds, while hardness values increased to 198 HV with increasing Ru addition up to 2% Ru.

© 2016 B.N. Zuma and J.W. van der Merwe. Published by Elsevier B.V.
Peer-review under responsibility of the organizing committee of SMPM 2017.

Keywords: Ruthenium, corrosion, 316L stainless steel.

12 Introduction

Austenitic stainless steels (ASS) are widely used in high performance pressure vessels, nuclear, chemical, process and medical industry due to their very good corrosion resistance and superior mechanical properties [1]. The 316L stainless steel is a Mo bearing austenitic. Welding is a common technique used to join 316L ASS which results in the solidified weld metal behaving as a miniature "casting". The welding procedure influences the mechanical properties and the microstructural morphology of the 316L ASS. The L-grades ASSs are generally recognised as resistant to sensitization in short-term exposures or heat treatments such as welding. However, 316L still remains susceptible to other forms of corrosion such as pitting corrosion to a lesser extent compared to conventional Ni-Cr stainless steels such as 304 ASS. Corrosion has cost the stainless steel industry extensively in maintenance and mechanical failures particularly at the welded joints of ASSs. Chernova and Tomashov (1978) showed that a small addition of Platinum Group Metals (PGM) to the weld metal of ASSs caused the cathodic potential to spontaneously move to the passive region through a phenomenon known as "cathodic modification" thus protecting the ASS from corrosion [1,2,3,4]. This work compromised tests validate the potential benefit that Ru addition would have on the corrosion resistance of the weld metal based on microstructural and mechanical properties. Additionally the increase in availability and affordability of Ru in South Africa makes it more feasible as an alloying element in the weld

* Corresponding author. Tel.: +27 11 717 7524; fax: +27 83 651 8238.
E-mail address: josias.vandermerwe@wits.ac.za

metal of 316L ASS. The microstructural evolution of 316L ASS when it undergoes gas tungsten arc welding (GTAW) and the impact on mechanical properties with increasing Ru addition to the weld metal were investigated. The microstructures of all GTAW button samples exhibited γ-austenite phases with δ-ferrite at the dendritic boundaries. Bulky δ-ferrite phases extending to thin dendrite arms were observed at 0.1 wt% Ru while a skeletal δ-ferrite microstructure was observed with 2 wt% Ru addition. The FA solidification mode suggested that an incomplete solid-state transformation had occurred due the melting of the 316L in water cooled conical shaped copper mould [5,6]. The hardness results revealed that 316L ASS had an increase in hardness as Ru addition was increased due to grain refining nature of Ru. Overall, it was concluded that the addition of Ru exhibits no detrimental effect of the solid state transformation but rather strengthens the alloy as Ru increases. Moreover, it can be deduced that the Ru additions in 316L weld metal not only improve the weld metal mechanical properties but can additionally improve the corrosion resistance of the weld metal [2].

13 Experimental methods

13.1 Generation I welds-GTAW Button on welds

Button melted welds were prepared using GTAW then a variety of tests were performed on button-melted samples. Buttons with total weight of 10 grams were made by gas tungsten arc melting 316L and Ru feed material under argon and then air cooling. The following compositions were added to the button welds: 0.1% Ru, 0.5% Ru, 1% Ru, and 2% Ru (all compositions given as percentage of the 10 grams buttons). Since Ru is a form of powder and can be easily blown away by the arc, the powder was compacted and compressed and placed beneath a piece of 316L parent material. The GTAW button welds were fabricated using a button-arc furnace at Mintek (South Africa) under an argon atmosphere using titanium as an oxygen-getter, and were cooled in the furnace, on a water-cooled copper hearth as shown in Figure 1(a).

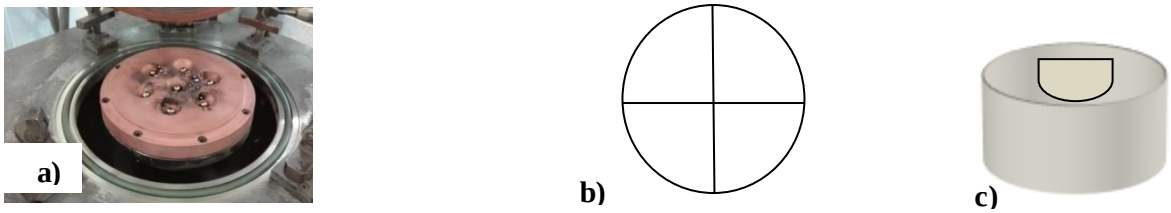


Figure 92: (a) The Copper Hearth for Compact Vacuum Arc Melting System at Mintek. The schematic of the (b) spherical button weld and dimensions it was cut into and (c) the cross sectional view of mounted sample.

13.2 Stage 1: Test samples preparation

13.2.1 Preparation for metallography

The spherical GTAW button samples were cut into four quarters as shown in Figure 1(b) and used separately. The spherical quarter samples were hot mounted in Bakelite resin. The exposed surfaces of the mounted samples shown in Figure 1(c) were then wet ground with silicon carbide papers from 220 down to 1200 grit. Before every subsequent step the sample exposed areas were rinsed with distilled water and air dried. Thereafter the samples were polished with several polishing grits. Finally distilled water was used to clean the sample, acetone was then used to degrease the sample, and samples were dried using a dryer. The sample microstructure can thereafter be examined using an optical microscope, high resolution Zeiss SEM analysis and EDX analysis. For the optical microscope imaging the stainless steel samples were etched with a reagent that had one part HNO_3, one part HCl and one part H_2O.The samples were stirred in the solution at 20°C for uniform, stain-free results. The reagent further outlined the button welds constituents and revealed grain structure. The EDX and SEM analysis was carried out using an electron microprobe set to 10kV accelerating voltage and 200nA beam current.

13.3 Mechanical Tests: Hardness test

Vickers hardness test was carried out on the prepared Generation I button welded samples. Hardness distribution measurements of welds are commonly measured with hardness HV5 or HV10. The exact positioning of the test points depend on the type of weld joint, detailed in various norms and standards, such as EN ISO 9015 [7].

14 Results and Discussion

14.1 Microstructural evaluation: GTAW button samples

14.1.1 Optical Microscope

The microstructural evaluation of the GTAW button welds depicted the typical fusion boundary microstructure for GTA welded 316L ASS. The 316L weld metal solidifies as primary δ ferrite dendrites as can be seen in Figure 2(a) for 0.1wt% Ru. During the solid state, ferrite to austenite transformation occurs by a diffusion controlled process. Under normal weld solidification conditions, the solidification mode in ASS is primarily a function of composition, with a shift from primary ferrite to primary austenite accomplished by reducing the Creq/Nieq ratio below 1.5 [8]. Due to the fast cooling nature of the copper hearth the austenite region had enrichment in Ni and depletion of Cr. The Ni diffused in the ferrite towards the advancing austenite [9]. The Cr was rejected by the advancing interface as shown by the EDX microprobe results.

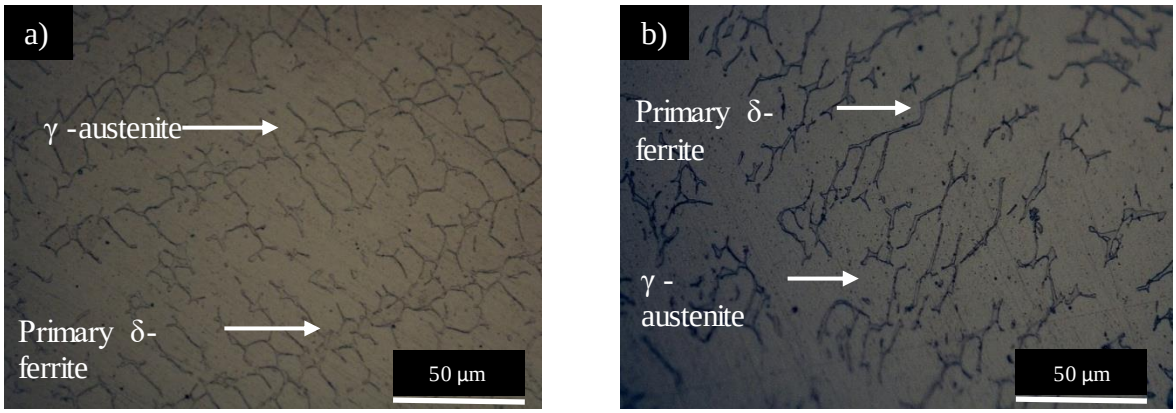


Figure 2(a): Etched optical microstructure of 0.1% Ru 316Lbutton welds and (b) Etched optical microstructure with 2% Ru 316L button welds

Figures 2(a) and (b) shows the columnar dendrite zone and the typical morphologies of σ-ferrite in the fusion zone such as: (a) lathy δ (ferrite) with 0.1 wt% Ru addition and (b) skeletal microstructure with lathy δ-ferrite in the 2 wt% Ru 316L button weld. This ferrite morphology was observed due to the melting of the 316L into a conical shaped copper mould. Baldission et al suggested that formation of this ferrite morphology was a result of the suppression of the δ→γ (austenite) solid-state transformation due to higher cooling rate [10]. These columnar dendrite zones were observed in the 0.5wt% Ru and 1wt% Ru 316L button welds as well.

14.1.2 SEM and EDX analysis

Figure 3(a) and (b) shows the microstructure obtained using SEM- Backscattered electron (BSE) image with a 10µm scale. The regions were thereafter probed for chemical composition to determine the phase present and their composition.

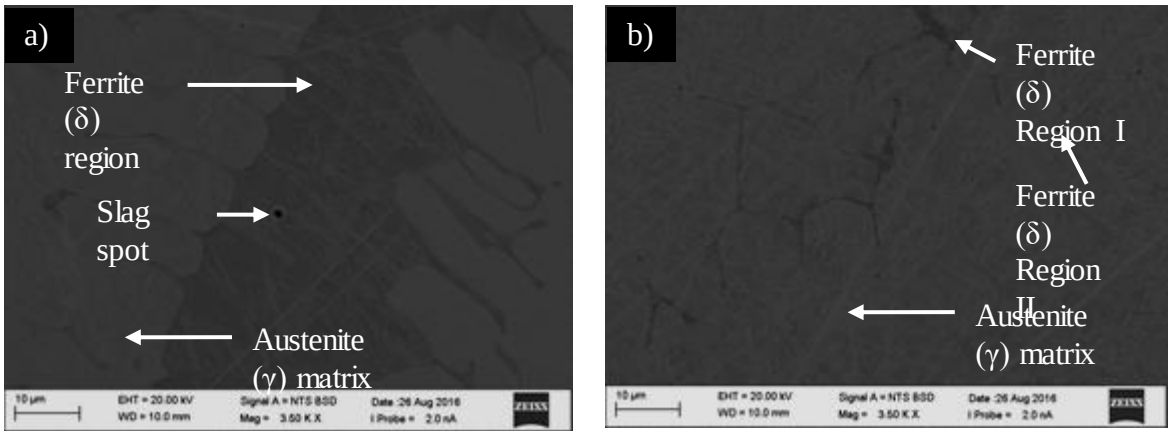


Figure 3(a): The 0.1% Ru alloyed 316L button welded sample and (b) The 2% Ru alloyed 316L button welded sample.

The microstructure showed the expected two phase microstructure of δ-ferrite and γ-austenite, the austenite phase appear brighter and the ferrite phase darker. The Figure 3(a) showed a thick primary (δ) ferrite region at 1% Ru addition , this then extended to lathy ,thin dendritic arms. Figure 3(b) shows δ-ferrite region enriched in Cr and depleted in Ni and its morphology appears more skeletal in nature. This reinforces that the addition of a noble metal such as Ru has grain refining capabilities. The chemical compositions of the different phases for Figure 3(b) are shown by the EDX results in Table 1.

Table 1: Chemical Compositions (wt %) of GTAW 316L button samples alloyed with 2% Ru analysed by EDX analysis.

Phases	Elements (wt %)							
	Cr	Ni	Mn	Mo	Fe	Si	Ru	Ti
Region I **Ferrite (δ)**	21.3±.1	5.1±0.1	-	3.6±0.1	61.3±0.2	0.8±0.1	1.8±0.2	-
Region II **Ferrite (δ)**	15.2±0.1	9.2±0.2	1.4±0 .1	2.1±0.1	55.7±0.3	0.5±0.2	1.7±0.3	2.9±0
Matrix **Austenite (γ)**	16.6±0.2	11.0±0.1	-	2.2±0.1	65.6±0.1	0.5±0.2	2±0	-

The chemical composition of all alloys for the 316L button welds were analysed using the EDX microprobe. Ti was detected after welding as slag forming compounds (such as Ti, Ca, and Al) accumulate together and precipitate as a spot on button welds [11]. The solidification behaviour of these alloys was categorized into four basic solidification modes according to the morphologic criteria presented in the literature by several authors [12,13]. Figure 4 depicts the Schaeffler constituents diagram used to predict or determine the stainless steel weld metal structure.

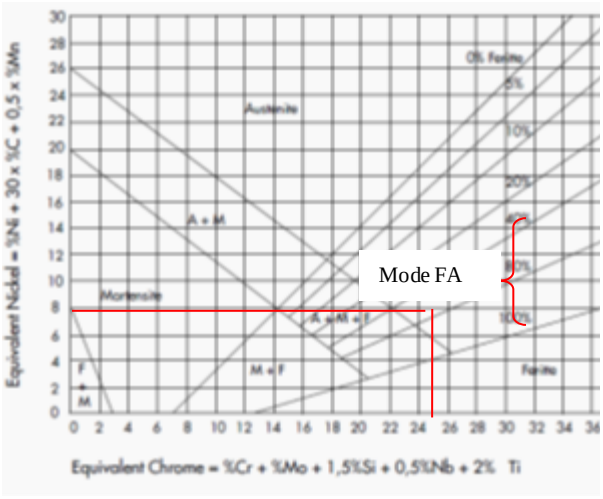


Figure 4: Schaeffler diagram for stainless steel weld metal [14].

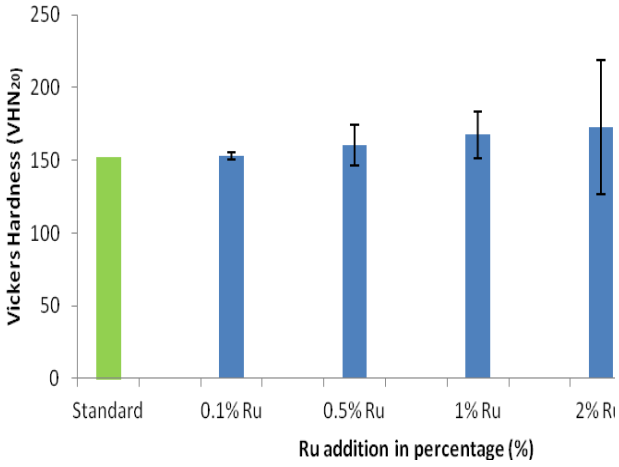


Figure 5: Vickers hardness test results for different Ru additions for the GTAW 316L button samples at: 0.1%, 0.5%, 1% and 2% Ru additions.

Therefore Ni_{eq} and Cr_{eq} equations can be estimated by imputing the EDX analysis results seen in Table 1 in the following equations [15].

$$Ni_{eq} = \%Ni + 35 \times \%C + 20 \times \%N + 0.25 \times \%Cu \quad (1)$$

$$Cr_{eq} = \%Cr + \%Mo + 0.7 \times \%Nb \quad (2)$$

In the current study, the solidification mode was characterised as FA alloys for GTAW 316L ASS. FA alloys consist of primary δ-ferrite with a eutectic γ at the end of solidification. Under equilibrium solidification conditions, the 316L ASS exhibit a mixed mode of freezing [8]. However with 2% Ru addition to the weld metal that was cooled on a Cu hearth, the Cr_{eq} /Ni_{eq} ratio was in-between the range of 1:48-1:95 and therefore it was classified as a FA alloy. This verified the microstructural phases observed in the optical microscope and SEM images analysis. With Mo contents ±2.5 wt % the microstructure could contain the Mo-rich σ-sigma intermetallic, often in some form of coupled growth with γ-austenite [8]. The EDX results for this Mo bearing 316L ASS showed that it had a homogenous chemical distribution throughout the different phases. Numerous studies have demonstrated the susceptibility of Mo-depleted regions of the microstructure to preferential corrosive attack when the chemical distribution of the alloy is not homogenous [16, 17,18]. This can further be assisted by the addition of Ru to the weld metal of 316L ASS by GTAW, to further decrease susceptibility to corrosion attack particularly when sample is homogenous.

14.2 Hardness results

The Vickers hardness tests were carried out according to EN ISO 9015-1:2001 [7]. Figure 5 shows the influence of Ru aaddition on the hardness of GTAW 316L button samples. The Vickers hardness tests were carried out with load of 10kgf with a dwell time of 30 seconds.The hardness results revealed that 316L has an increase in hardness as Ru addition was increased due to grain refining nature of Ru. The Vickers hardness measurements across the bead-substrate interface revealed a significant increase in hardness, varying from 152 HV for the AISI 316L parent material to 198 HV for the GTAW button samples, for 2% Ru alloyed sample shown in Figure 5. The increased hardness of alloys with 1% Ru and 2% Ru as compared to the 0.1% Ru and 0.5% Ru can be attributed to their high Ru and Ni content, as well as the microstructural changes due to heating in the vacuum arc furnace. The hardening effect of both Ru and Ni on alloys is well-known [19].

15 Conclusion

Overall, it can be concluded that the addition of Ru exhibits no detrimental effect on the solid state transformation as these phases appeared both in the 0.1wt% Ru and 2 wt% Ru containing alloy. The GTAW button welds at the different

percentage of Ru addition depicted certain similar metallographic features. During solid state process the growth in γ-austenite was accompanied by the rejection of Cr and the acceptance of Ni. This FA solidification mode resulted in the enrichment in Cr and depletion of Ni in the residual δ-ferrite. Moreover, Ru additions in 316L weldments can improve the weld metal mechanical properties as indicated by the increase in hardness to values of 197 HV with 2% Ru addition to the 10 gram GTAW button welds.

16 References

[1] G.P. Chernova, N.D. Tomashov, and L.A. Chigirinskaja, The Effect of Alloying on the Passivation of Iron Chromium Based Alloys , Corrosion:The Journal of Science and Engineering, 34, 12 (1978) 445-446.

[2] I. Wolff, P. Park-Ross, and A. Ball, Localised corrosion of high chromium superferritic alloys. British Corrosion Journal, 26 (1991) 202-208.

[3] J. H. Potgieter, H. C. Brooke, Corrosion Behavior of a High-Chromium Duplex Stainless Steel with Minor Additions of Ruthenium in Sulfuric Acid. Corrosion, 4, 51 (1995) 312-320.

[4] I.M. Wolff, L.E. Iorio, T. Rumpf, P.V.T. Scheers, and J.H. Potgieter, Oxidation and corrosion behaviour of Fe–Cr and Fe–Cr–Al alloys with minor alloying additions, Materials Science and Engineering, 241, 1-2 (1998) 264–276.

[5] G.L. Leone, and H.W. Kerr, The ferrite to austenite transformation in stainess steels, Welding research supplement ,1982.

[6] J. M Vitek , and S.A. David, Trends in Welding Research in the United States, American Society for Metals, Metals Park, Ohio , 1982, pp.243-258.

[7] ISO, Destructive tests on welds in metallic materials, Hardness testing -Part 1: Hardness test on arc welded joints [Internet], 2001 [Cited 30 August 2016], Available from https://www.iso.org. ISBN.

[8] M.J. Perricone, T.D. Anderson, C.V. Robino, J.N. DuPont, and J.R. Michael, Effect of Composition on the Formation of Sigma during Single-Pass Welding of Mo-Bearing Stainless Steels, Metallurgical and Materials Transactions A. 38, 9 (2007) 1976-1990.

[9] V.P. Kujanpaa, S.A. David , C.L. White, Formation of Hot Cracks in Austenitic Stainless Steel Welds-Solidification Cracking, Welding Research Supplement, Oulu, Finland , 1986, pp. 204-212.

[10] D. Baldissin, M. Baricco, and L. Battezzati, Microstructures in rapidly solidified AISI 304 interpreted according to phase selection theory, Material Science and Engineering A , 449-451 (2007) 999-1002.

[11] S.R. Collins, Stainless Steel for semiconductor Applications,39th Mechanical Working and steel processing Conference of the Iron and steel Society 1998, Indianapolis, 19-22 (1997) pp. 607-619.

[12] J.A. Brooks, M.I. Baskes, and F.A. Greulich, Solidification and solid state transformationin high energy density stainless steel welds, Metallurgical and Materials Transactions A, 22 (1991) 915–926.

[13] F. Junwei,Y. Yang, and J.J. Guo, Formation of a blocky ferrite in Fe–Cr–Ni alloy during directional solidification, Journal of Crystal Growth ,China , 311, 14 (2009) 3661-3666.

[14] British stainless steel association, The Schaeffler and Delong diagrams for predicting ferrite levels in austenitic stainless steel welds[Internet], 2016 [cited 12 August 2016], Available from http://www.bssa.org.uk .

[15] D.J. Kotechi, T.A. Siewert, WRC-1992 Constitution Diagram for Stainless Steel Weld Metals: A Modification of the WRC-1988 Diagram , Refined constitution diagram offers more accurate FN prediction for Cu-containing stainless steels and dissimilar metal joints ,Welding Journal, 71 (1992) 172s.

[16] A. Garner, Corrosion Journal, Houston,third ed , 35, 3 (1979) 108-14.

[17] A. Garner, Materials Performance,eight ed, Houston , 21 (1982) 9-14.

[18] M.B. Rockel, and M. Renner, Pitting, Crevice and stress corrosion resistance of high chromium und molybdenum alloy stainless steels. Materials and Corrosion, 35, 12 (1984) 537–542.

[19] C.A. Hampel, Rare Metals Handbook , New York, NY, USA , 1954.

Effect of Ru addition on the mechanical properties and microstructure of 316L austenitic stainless steel weld metal.

B.N. Zuma[a, b] and J.W. van der Merwe[a,b,c]

[a]School of Chemical and Metallurgical Engineering, University of the Witwatersrand, Johannesburg, South Africa

[b]DST-NRF Centre of Excellence in Strong Materials, University of the Witwatersrand

[c]African Materials Science and Engineering Network

Introduction

The addition of platinum group metals (PGM'S) to the weld metal of 316L austenitic stainless steel (ASS) by gas tungsten arc welding (GTAW) button welds resulted in superior mechanical properties. In the present investigation, the effect of Ru additions on the physical properties of 316L weld was evaluated by investigating the microstructural and mechanical properties of weld metal. The microstructure and mechanical properties of the alloyed button welds were analyzed using optical microscope, scanning electron microscope (SEM), EDX and Vickers hardness test at 0.1, 0.5, 1 and 2 wt% Ru addition.

Methodology

Buttons with total weight of 10 grams were made by gas tungsten arc melting 316L and Ru feed material under argon and then air cooling. The following compositions were added to the button welds: 0.1% Ru, 0.5% Ru, 1% Ru, and 2% Ru (all compositions given as percentage of the 10 g buttons). The GTAW button welds were fabricated using a button-arc furnace at Mintek (South Africa) under an argon atmosphere using titanium as an oxygen-getter, and were cooled in the furnace, on a water-cooled copper hearth. The samples were thereafter metallograpically prepared, so the microstructure can thereafter be examined using an optical microscope, high resolution Zeiss SEM analysis and EDX analysis. Lastly Vickers hardness measurements were carried out for hardness values varying from HV5 or HV10 on the prepared 316L button welded samples.

Results and discussion

The microstructural evaluation of the GTAW button welds depicted the typical fusion boundary microstructure for GTA welded 316L ASS. Figures 1(a) and (b) shows the typical morphologies of vermicular δ-ferrite in the austenite matrix, (a) with 0.1 wt% Ru addition and (b) with 2 wt% Ru added to the 316L button weld. Baldission et al suggested that formation of this ferrite (vermicular) morphology was a result of the suppression of the δ→γ (austenite) solid-state transformation due to higher cooling rate from the Cu water-cooled hearth[1]. The thin, vermicular δ-ferrite morphology observed in Figure 2(b) for 2 wt% Ru reinforces the grain refining capabilities of Ru. During the solid state, ferrite to austenite transformation occurs by a diffusion controlled process. Under normal weld solidification conditions, the solidification mode in ASS is primarily a function of composition, with a shift from primary ferrite to primary austenite accomplished by reducing the Creq/Nieq ratio below 1.5[2]. In the current study, the solidification mode was characterised as FA alloys for GTAW 316L ASS according to the morphologic criteria presented in the literature by several authors[3]. FA alloys consist of primary δ-ferrite with a eutectic γ at the end of solidification.

---

[1] D. Baldissin, M. Baricco, and L. Battezzati.(2007). Microstructures in rapidly solidified AISI 304 interpreted according to phase selection theory, *Material Science and Engineering A* , 449-451 ,999-1002.

[2] M.J. Perricone, T.D. Anderson, C.V. Robino, J.N. DuPont, and J.R. Michael. (2007). Effect of Composition on the Formation of Sigma during Single-Pass Welding of Mo-Bearing Stainless Steels,*The Minerals, Metals & Materials Society and ASM International,* 38 (9) 1976–1990.

[3] J.A. Brooks, M.I. Baskes, and F.A. Greulich.(1991). Solidification and solid state transformationin high energy density stainless steel welds, *Metallurgical and Materials Transactions A*, 22, 915–926.

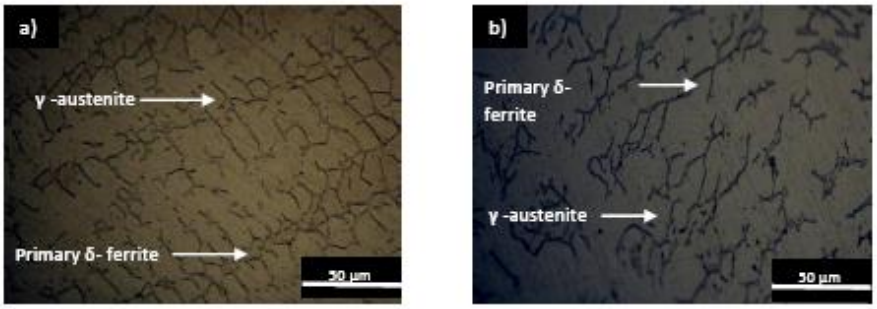


Figure 1(a): Etched optical microstructure of 0.1wt% Ru 316L button welds and (b) Etched optical microstructure with 2 wt% Ru 316L button welds.

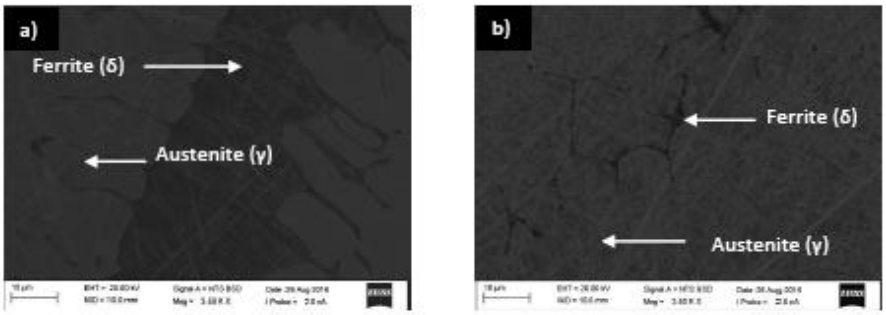


Figure 2(a): The 0.1 wt % Ru alloyed 316L button welded sample and (b) The 2 wt% Ru alloyed 316L button welded sample.

Figure 2(a) and (b) shows the microstructure obtained using SEM- Backscattered electron (BSE) with regions that were probed for chemical composition to determine the phase present and their composition. The austenite (darker) region had enrichment in Ni and depletion of Cr and the inverse for δ-ferrite. The Ni diffused in the ferrite towards the advancing austenite. No segregation of Ru was detected, Ti was detected after welding as slag forming compounds (such as Ti, Ca, and Al) accumulated together and precipitated as a spot on button welds. The Vickers hardness measurements across the bead-substrate interface revealed a significant increase in hardness due to grain refining nature of Ru. The hardness varied from 152 HV to 198HV for the AISI 316 L parent materials and the GTA welded 2% Ru alloyed sample respectively. The normal law assumption at a 95% confidence level was applied with each sample having five indentations.

Conclusions

Overall, it can be concluded that the addition of Ru exhibits no detrimental effect on the solid state transformation as similar phases appeared in the 0.1 wt% Ru and 2 wt% Ru containing alloy. The GTAW button welds at the different percentage of Ru addition depicted certain similar metallographic features. The FA solidification mode resulted in the enrichment in Cr and depletion of Ni in the residual δ-ferrite. Moreover, Ru additions in 316L weldments improved the weld metal mechanical properties as indicated by the increase in hardness to values of 197 HV with 2% Ru addition to the 10 gram GTAW button welds.